NAVAL POSTGRADUATE SCHOOL

MONTEREY, CALIFORNIA

THESIS

OCEANOGRAPHIC EFFECTS ON MARITIME THREATS: MINES AND OIL SPILLS IN THE STRAIT OF HORMUZ

by

Travis Clem

March 2007

Thesis Advisor:	Peter C. Chu
Second Reader:	Steven D. Haeger

Approved for public release; distribution is unlimited

THIS PAGE INTENTIONALLY LEFT BLANK

REPORT DOCUMENTATION PAGE		*Form Approved OMB No. 0704-0188*
<td colspan="3">Public reporting burden for this collection of information is estimated to average 1 hour per response, including the time for reviewing instruction, searching existing data sources, gathering and maintaining the data needed, and completing and reviewing the collection of information. Send comments regarding this burden estimate or any other aspect of this collection of information, including suggestions for reducing this burden, to Washington headquarters Services, Directorate for Information Operations and Reports, 1215 Jefferson Davis Highway, Suite 1204, Arlington, VA 22202-4302, and to the Office of Management and Budget, Paperwork Reduction Project (0704-0188) Washington DC 20503.</td>		
1. AGENCY USE ONLY *(Leave blank)*	**2. REPORT DATE** March 2007	**3. REPORT TYPE AND DATES COVERED** Master's Thesis
<td colspan="2">**4. . TITLE AND SUBTITLE** Oceanographic Effects on Maritime Threats: Mines and Oil Spills in the Strait of Hormuz</td>	**5. FUNDING NUMBERS**
<td colspan="2">**6. AUTHOR(S)** Travis Clem</td>	
<td colspan="2">**7. PERFORMING ORGANIZATION NAME(S) AND ADDRESS(ES)** Naval Postgraduate School Monterey, CA 93943-5000</td>	**8. PERFORMING ORGANIZATION REPORT NUMBER**
<td colspan="2">**9. SPONSORING /MONITORING AGENCY NAME(S) AND ADDRESS(ES)** N/A</td>	**10. SPONSORING/MONITORING AGENCY REPORT NUMBER**
<td colspan="3">**11. SUPPLEMENTARY NOTES** The views expressed in this thesis are those of the author and do not reflect the official policy or position of the Department of Defense or the U.S. Government.</td>		
<td colspan="2">**12a. DISTRIBUTION / AVAILABILITY STATEMENT** Approved for public release; distribution is unlimited</td>	**12b. DISTRIBUTION CODE** A
<td colspan="3">**13. ABSTRACT (maximum 200 words)**		

The Strait of Hormuz is a unique waterway vital to world commerce; as such, it is of military importance as well. The strait is narrow and has turbulent currents that change in intensity and direction due to the reverse estuarine flow of the Persian Gulf. On the border between extratropical and monsoonal atmospheric synoptic influences, the wind direction and intensity are dependent on time of year, which side of the strait due to terrain, and time of day due to land/sea breeze cycles. Utilization of model field inputs (from near real-time models) to tactical decision aids greatly enhances the information output by those aids.

Using the examples of drifting mines and oil spills, the utility of these model fields is shown when compared to climatology inputs. OILMAP, the oil dispersion model developed at Applied Science Associates, is used in this study to demonstrate how the behavior of an oil spill reacts with model field inputs for surface winds and currents from the Naval Oceanographic Office and the Fleet Numerical Meteorology and Oceanography Center, followed by comparative analysis between climatology inputs. Drift mine behavior is analyzed utilizing a simple Lagrangian drift model with model field inputs compared with climatology inputs.

The results from the comparisons show that the variable nature of the wind/current direction and speed through the strait is impossible to capture using climatology inputs. Winds less than 5 m/s are not a factor in the movement of an oil slick; even compared to the slowest of currents at ~10-15 cm/s. It is determined that the tidal nature of the currents through the strait, combined with variable strength of the winds, make prediction of oil slick or mine drift track unrealistic using climatology data. Therefore, using operational, near real-time environmental data is necessary for information superiority.

14. SUBJECT TERMS Meteorology, Oceanography, Strait of Hormuz, Drift Mine, Oil Spill, OILMAP, SWAFS, COAMPS, Empirical Orthogonal Function, EOF, Complex EOF, semidiurnal, diurnal, spring/neap tide, mass balance graph,			**15. NUMBER OF PAGES** 124
			16. PRICE CODE
17. SECURITY CLASSIFICATION OF REPORT Unclassified	**18. SECURITY CLASSIFICATION OF THIS PAGE** Unclassified	**19. SECURITY CLASSIFICATION OF ABSTRACT** Unclassified	**20. LIMITATION OF ABSTRACT** UL

NSN 7540-01-280-5500

Standard Form 298 (Rev. 2-89)
Prescribed by ANSI Std. 239-18

THIS PAGE INTENTIONALLY LEFT BLANK

OCEANOGRAPHIC EFFECTS ON MARITIME THREATS: MINES AND OIL SPILLS IN THE STRAIT OF HORMUZ

Travis Clem
Lieutenant, United States Navy
B.A., University of Texas at Austin, 2001

Submitted in partial fulfillment of the
requirements for the degree of

MASTER OF SCIENCE IN PHYSICAL OCEANOGRAPHY

from the

NAVAL POSTGRADUATE SCHOOL
March 2007

Author: Travis Clem

Approved by: Peter C. Chu
                Thesis Advisor

                Steven D. Haeger
                Second Reader

                Mary L. Batteen
                Chairman, Department of Oceanography

THIS PAGE INTENTIONALLY LEFT BLANK

ABSTRACT

The Strait of Hormuz is a unique waterway vital to world commerce; as such, it is of military importance as well. The strait is narrow and has turbulent currents that change in intensity and direction due to the reverse estuarine flow of the Persian Gulf. On the border between extratropical and monsoonal atmospheric synoptic influences, the wind direction and intensity are dependent on time of year, which side of the strait due to terrain, and time of day due to land/sea breeze cycles. Utilization of model field inputs (from near real-time models) to tactical decision aids greatly enhances the information output by those aids.

Using the examples of drifting mines and oil spills, the utility of these model fields is shown when compared to climatology inputs. OILMAP, the oil dispersion model developed at Applied Science Associates, is used in this study to demonstrate how the behavior of an oil spill reacts with model field inputs for surface winds and currents from the Naval Oceanographic Office and the Fleet Numerical Meteorology and Oceanography Center, followed by comparative analysis between climatology inputs. Drift mine behavior is analyzed utilizing a simple Lagrangian drift model with model field inputs compared with climatology inputs.

The results from the comparisons show that the variable nature of the wind/current direction and speed through the strait is impossible to capture using climatology inputs. Winds less than 5 m/s are not a factor in the movement of an oil slick; even compared to the slowest of currents at ~10-15 cm/s. It is determined that the tidal nature of the currents through the strait, combined with variable strength of the winds, make prediction of oil slick or mine drift track unrealistic using climatology data. Therefore, using operational, near real-time environmental data is necessary for information superiority.

THIS PAGE INTENTIONALLY LEFT BLANK

TABLE OF CONTENTS

THIS PAGE INTENTIONALLY LEFT BLANK

LIST OF FIGURES

xiii

THIS PAGE INTENTIONALLY LEFT BLANK

LIST OF TABLES

THIS PAGE INTENTIONALLY LEFT BLANK

ACKNOWLEDGMENTS

THIS PAGE INTENTIONALLY LEFT BLANK

I.   INTRODUCTION

The Persian Gulf (hereinafter referred to as the Gulf) is a region of high tactical and economical importance to the United States as well as the world. Unfortunately it is also a hotbed of hostility between nations of the Gulf as well as towards nations of the West and especially the United States (U.S.). Sectarian violence and insurgency threats leave many of the nation states of the region in a seemingly permanent state of unrest. The threat of terrorist (non-state actors) attacks is unrelenting in the region. Also, the threat from neighboring nations is very real.

Iran has been very vocal in its condemnation of the West and especially the United States. An ongoing dispute with the United Arab Emirates (UAE) over the islands of Abu Musa, Greater Tunb, and Lesser Tunb started when they were occupied by Iranian troops in 1971 (Kreil, 2004, and Kjeilen, 1996). Although Iran boasts the second largest length of the Gulf's coastline (1,700 km compared to Saudi Arabia's 2,640 km, from Kreil, 2004) extending from east of the Shatt al Arab river, around the Strait of Hormuz (SOH) to the border of Pakistan at the Gulf of Oman (GOO), these three islands give Iran an even better strategic position on the SOH (Figure 1). Iran's posture is hostile to outside military presence and seems to seek dominance in the waters of the Persian Gulf itself. Iran has developed long-range missiles specifically for naval warfare (Zaman, March 2006), and has used the thinly veiled threat of their use if the U.S. continues military exercises in the Gulf. Iran has been steadily making headway on building a nuclear program. If successful, tensions in the Middle East will be very high and Iran's power will be an undeniable influence on the politics of the region and therefore, the world. Additionally, closure of the SOH has been threatened if the U.S. and its allies continue to block Iran's efforts at gaining nuclear capability (Diba, 2006).
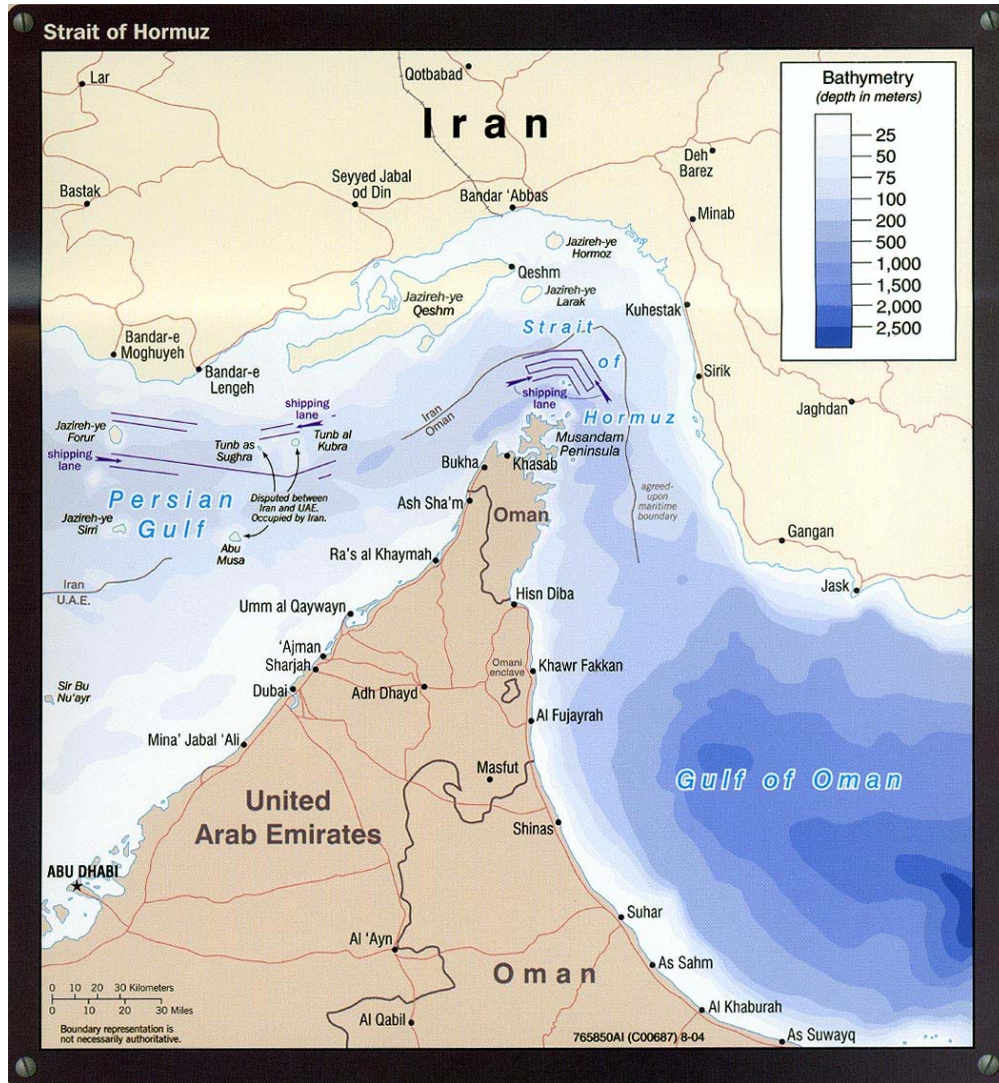
Figure 1.   Strait of Hormuz bathymetry and surrounding region. (From: www.lib.utexas.edu/maps/iran.html)

It is in this uneasy environment that approximately one-third of the world's supply of oil is provided. The methods of oil export are by pipeline to the port of Yanbu (across Saudi Arabia) and shipping through the SOH into the Arabian Sea and beyond. Additionally, three inactive pipelines (one in Iraq and two in Saudi Arabia) could potentially be used (Kreil, 2004). The full flow potential for all the pipelines together is about seven million barrels of oil a day. However, the SOH is the main avenue for the transport of oil (at 16.5-17 million barrels a day) as well as other goods both into and out of the Gulf. According to a report from the Energy Information Administration, roughly 90% of the oil leaving the Gulf, accounting for about two-fifths of the world's free traded

oil, left via tankers transiting the SOH (Kreil, 2004). Interestingly, the SOH is a natural choke point narrowing to just 56 km (34 miles) across with two mile wide transit lanes separated by a two mile wide buffer (Figure 1). Whether by IED (improvised explosive device), suicide bomber, or by mining, the SOH could be the target a terrorist attack or of a nation like Iran to hold the states of the Gulf hostage. Economic fallout would continue long after the stoppage was cleared. Even if all of the pipelines were working and able to pump immediately the loss or reduction in the volume of shipping could have dramatic negative effects on the world market (Kreil, 2006).

Understanding the oceanographic effects on potential oil spills, and drift mining could mean the difference for a faster recovery from an incident at this choke point. The faster the clean up or mine clearing, the faster shipping and maritime patrol can resume. Numerical models of drift tracks for mines and oil spill dispersion are currently available. The environmental inputs of current and wind speed that are vital to the performance of those models. Thus, the better the environmental data and models, the more accurate predictions are for dealing with oil spills and mine drifting.

Oil spill due to various reasons other than attack may likely be as effective at slowing down shipping. On 24 January 2000, Honduran-flagged cargo vessel Al Jazya 1 sank 4 miles east of Abu Dhabi's coast, laden with 980 tons of fuel oil. This vessel sank in bad weather. Also, on 6 April 2001, the Iraqi fuel tanker Zainab, suspected of smuggling around 1,300 tons of fuel oil from Iraq, ran into trouble on its way to a holding area in international waters. It left an oil spill with a 12 km radius which reached the reserved island of Sir Bou Neair, about 70 nautical miles off the coast of the Emirate of Sharjah (www.marinergroup.com/oil-spill-history.htm).

The SOH lies between the GOO and the Gulf and acts as a source of fresh water to, and also as an outlet for the hypersaline waters of the Gulf (Reynolds, 1993). Atmospheric forcing for water circulation is, in part, due to predominant winds from the southwest year round that vary in strength. The intense evaporation of the Gulf and cooling of waters heading north along the coast of Iran cause the formation of hypersaline water; which is, in turn, also a source of forcing for circulation.

The climate variability between the Gulf and the GOO is remarkably different. The Gulf is mainly affected by extratropical systems from the northwest and the GOO is on the northern edge of the tropical weather systems that affect the Arabian Sea and the Indian Ocean (Reynolds, 1993). The GOO experiences the monsoonal circulations where the winds are southerly during the summer and then northerly in the winter. The SOH is the approximate boundary of the two systems and is therefore, an amalgam. Although it has been stated that the predominant wind direction in the SOH is southwesterly, it is useful to analyze variability of synoptic winds and their effects on oil and surface floating obstacles such as mines.

Complexity of the physical conditions in atmosphere and ocean, especially the winds and currents, makes the oil spill/mine drift difficult to predict in the SOH. High resolution full physical models are needed to predict (or simulate) the surface winds and currents. After the high-resolution winds and currents are obtained, the transport model and chemical models are utilized to predict (or simulate) the mine drift and oil spill. To do so, three models are applied: 1) the Coupled Ocean/Atmosphere Mesoscale Prediction System (COAMPS), 2) the Shallow Water Analysis and Forecast System (SWAFS), and OILMAP™. Among them, the first two are the Navy's operational models with COAMPS running at the Fleet Numerical Meteorological and Oceanographic Center (FNMOC) and SWAFS running at the Naval Oceanographic Office (NAVOCEANO). OILMAP is in the test phase at NAVOCEANO.

Atmospheric modeling for this area is handled by COAMPS, which is a mesoscale atmospheric model utilizing nested grids and capable of resolving small scale events. The use of Multi-Variate Optimum Interpolation (MVOI) allows for the use of irregularly spaced in-situ observations (Chen et al., 2003). For this study, the model fields utilized were the 00UTC analysis fields along with the 6, 12, and 18 hour forecasts.

Current structure and circulation was provided by SWAFS, which is a numerical ocean forecast system for three dimensional analysis and prediction of currents and thermohaline structure in both deep and shallow water (Clifford et al., 1994). This model was designed specifically with coastal oceanography in mind. It is forced in near-real time with wind stresses and air-sea thermohaline fluxes derived from operational

atmospheric models such as COAMPS or the Navy Operational Global Atmospheric Prediction System (NOGAPS), along with in situ temperature and salinity measurements, and sea-surface temperatures inferred from multichannel infrared satellite imagery (MCSSTs) (Clifford et al., 1994).

OILMAP is an oil fate/dispersion model developed by the Applied Science Associates (ASA), capable of tracking an oil spill forwards and backwards, on the surface as well as subsurface, and also has the ability to calculate probabilities of where the oil will go as well as where it probably originated from. The model field output from COAMPS and SWAFS are the input to OILMAP for oil spill simulation and evaluation.

In this study, the surface atmospheric conditions for the entire Gulf region to include the SOH and the GOO, especially the winds, are simulated using COAMPS and the ocean currents in the same region are simulated using SWAFS; both were conducted at the NAVOCEANO supercomputing center. The model output was then analyzed and used to predict the oil spill and mine drift calculations for possible threat scenarios to the SOH. If the direction and destination of such events as oil spills and mines are able to be accurately forecast, then it enables the surrounding nations and vessels to be coordinated properly for faster cleanup/clearing operations. And therefore, the impacts, both economic and material, will be mitigated substantially.

The effectiveness of an oil fates/dispersion model supplied with environmental air-ocean data from COAMPS and SWAFS is compared to climatology data ingested to the model. The chemical model (OILMAP) is integrated with two sets of atmospheric and oceanic fields over a period of 5 days: (1) climatology and (2) synoptic forcing fields, using COAMPS and SWAFS models. Two sets of the OILMAP output using the climatology and synoptic fields are compared.

This thesis involves the Commander Naval Meteorology and Oceanography Command's (CNMOC) Three Tiers of tasks for "Battlespace on Demand" (Figure 2). The idea of "Battlespace on Demand" is to effectively supply combatant commanders with true battle space information superiority. By supplying good data to the first tier, the Environmental Layer, the Navy's models are fed quality information about the battle space in past and near-real time. This then sets up the second tier, the Performance

Layer, where the performance of such models is improved to supply accurate forecasts for ocean environment conditions. Given the ability to accurately forecast the ocean environment, combatant commanders can make better decisions in force deployment, risk assessment, and asset allocation; as seen in the third tier. The work of this thesis attempts to address the third tier. Impacts on naval operations, such as ship routing and battle space maneuver, make it crucial to be able to accurately predict the environment in order to plan for and meet any threat with confidence. By comparing the effectiveness of operational model input, vice climatology, into valid decision tools it is hoped to relate the importance of model data to the mission planning and response phase for mission planners.
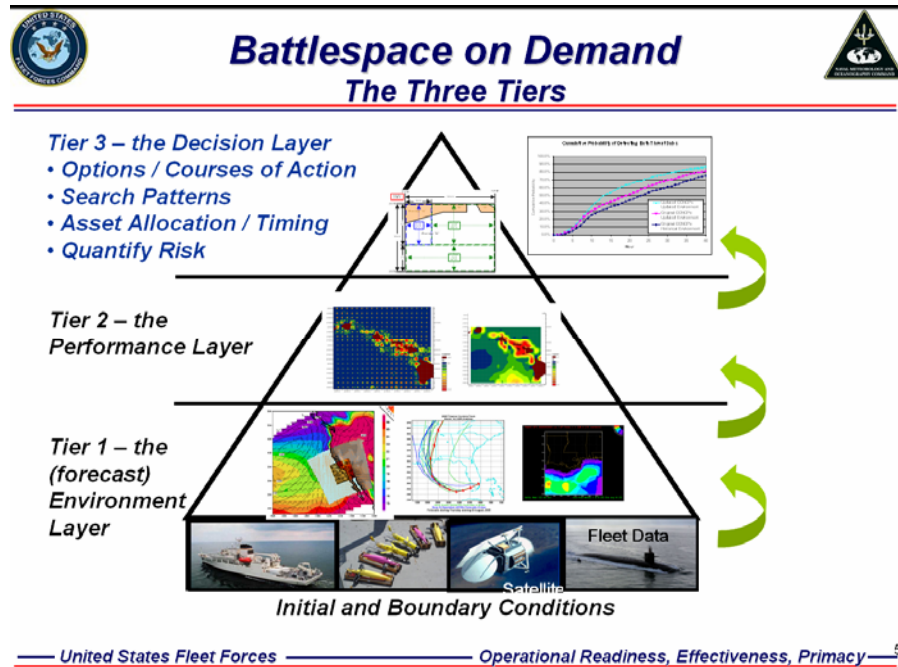
Figure 2.   Three Tiers of Battlespace on Demand   (From: Capt. Dave Titley, USN, 2007).

II. BACKGROUND

A. GEOGRAPHIC FEATURES

The SOH, separating the Persian Gulf from the GOO with a narrow channel of water that is 40 to an excess of 200 m in depth, is bordered by the Iranian province of Hormozgar to the north and the Omani exclave on the Musandam Peninsula to the south. (The Musandam Peninsula is surrounded by the UAE and the waters of the SOH and is therefore an exclave.) The strait is approximately 280 km long and about 50 km wide at its narrowest point.

The geography of the peninsula is made up of the Hajar Mountain Range, known as the "backbone" of Oman, which stretches from the south at Ra's al Hadd, and reaches Musandam where it descends into the waters of the SOH abruptly with the Ru'us al Jibal (Traut, 2002). At the SOH, the peninsula features a large number of fjords and few fishing villages, most of which are reachable only by boat (Figure 3) (Kjeilen, 1996).

Figure 3.   View of one of the fjords on the Musandam Peninsula (After: Kjeilen, 1996.)

Iran's Zagros Mountains begin in the northeastern Iran and end in the southern province of Hormozgan, north of the SOH (Ebrahim, 2006). These mountains descend to lime and sandy hills and highlands into the coastal plain parallel to the Gulf (HUMS, 1996).

B.   ENVIRONMENT

1.   Winds

The wind regimes vary from one body of water to the next in the Gulf region. The Gulf experiences an extra-tropical wind regime. With the deserts of the Arabian Peninsula to the west, there is little topographic barrier features to mitigate winds from this region. The mountains from Iran and Iraq act to channel winds to the southeast. Hence, winds in the Gulf are predominantly northwesterly ("shamal" winds, "shamal" means north in Arabic) in the northern portion of the gulf, becoming more westerly further south and become southwesterly on the western portion of the SOH (Chao et al, 1992). Reynolds (1993) points to the influence of Iran's Zagros Mountains for channeling of near-surface southerly winds (Figure 4). This topographic feature acts to restrict the strongest of the southerly winds to the southeastern Gulf (therefore, the western portion of the SOH). The GOO is much different than the extra-tropical weather systems of the Persian Gulf.

Figure 4.   Topographical map of the Middle East (After Chart number 803056AI(R02107)3-04, CIA , 2007)

Influenced by the northern edge of the monsoonal circulation, which heavily shapes the weather of the Arabian Sea and the Indian Ocean, the GOO winds are variable from northwesterly to southeasterly in the winter and predominantly southeasterly during the summer months (Reynolds, 1993).

The SOH resides in the approximate boundary region between these two regimes. It is possible that the mountain ranges to the north and south contribute to the prevailing southerly winds Bandar Abbas experiences (Figure 4 and Table 1). Coupled with the monsoonal influence of the GOO and the mountains of the Hajar Range, it is understandable why Khassab would have a seasonal variation between southerly winds from spring to summer, switching to northwesterly winds in late summer through winter (see Table 1). On the far western side of the SOH, Ras al Khaimah shows more of the extra-tropical influence.

Station	Month	Feb	Mar	Apr	May	Jun	Jul
Bandar Abbas, Iran	Wind Dir	S	S	S	S	S	S
	Wind Speed (m/s)	8	9	11	11	10	11
	Peak Gust (m/s)	58	39	31	62	30	65
Khassab International Airport, Oman	Wind Dir	S	S	S	S	S	NNW
	Wind Speed (m/s)	5	6	6	6	7	7
	Peak Gust (m/s)	50	45	63	52	45	53
Ras al Khaimah International Airport , UAE	Wind Dir	SSE	W	WSW	N	N	N
	Wind Speed (m/s)	7	11	13	8	8	7
	Peak Gust (m/s)	61	43	45	56	48	65

Table 1.   Climatology figures, from years 1995 to 2004, for weather stations (in order) to the north south and west of the SOH. (After: IPS MeteoStar, 2007)

Reynolds (1993) noted that a strong land/sea breeze occurs along the entire coastline. When analyzing for wind features this has to be taken into account since the land/sea breeze occurs at different times across the region. Therefore, dependent on the

size of the area being studied, it can be difficult to remove these effects from data analyses of winds. For instance, Bandar Abbas, Iran experiences the land/sea breeze prior to Ras al Khaimah, UAE, and much longer before Doha, Qatar. So when the winds data is analyzed the effect of the land/sea breeze is incorporated over a longer time period since it is a larger spatial area of effect (Eager et al., 2004).

Eager et al.(2005) show that the main mesoscale circulation in the region of the Gulf that affects meteorology is the sea and land breezes that develop due to the strong heating of the land and the largely weak synoptic scale winds. Offshore synoptic winds above 11 m/s and onshore synoptic winds stronger than three m per second inhibit sea breeze formation.

As part of an analysis of mean synoptic conditions from 1978 to 1998, it was found that Bandar Abbas experienced wind direction bimodality (see Figure 5(a, b, and d)). The winds were North and South and suggested the occurrence of land-sea breeze circulation (LSBC), which occurred at other stations in the Gulf but were not as evident due to synoptic conditions (Zhu and Atkinson, 2004).
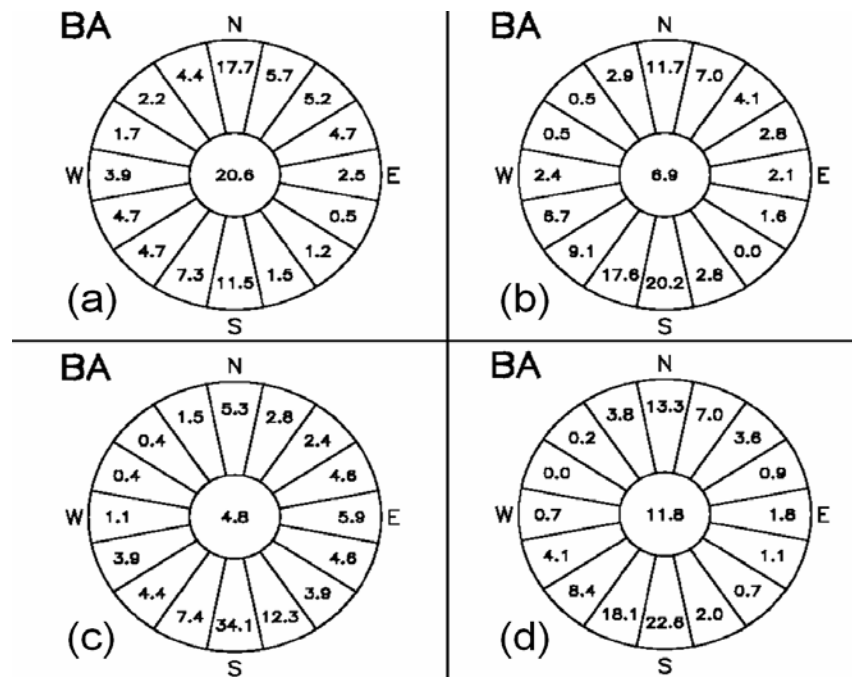
Figure 5.   Frequency of the hourly wind direction and calms (in center) observed at Bandar Abbas Airport (**BA**) in 2002: (a) January; (b) April; (c) July; (d) October. (After: Zhu and Atkinson, 2004)

10

2. Tides/Currents

Reynolds (1993) noted that the tides in the Gulf co-oscillate with the SOH (see Figure 6). The tides vary from being primarily semidiurnal to diurnal and have a large range; with values greater than one meter everywhere in the region. It is these strong tides that mask the weak residual currents that vary across the SOH (Reynolds, 1993).
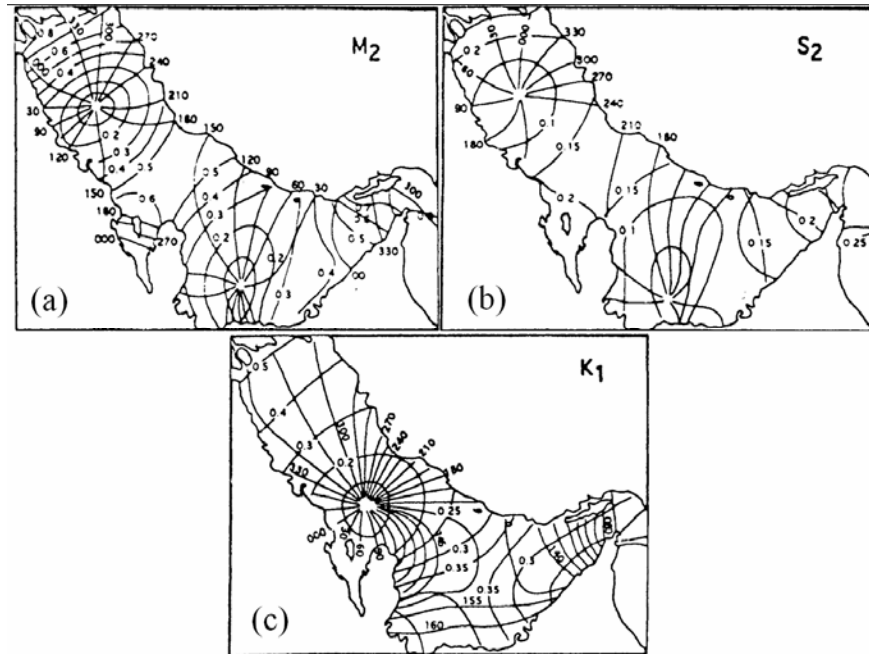
Figure 6.   Tidal Constituents of the Gulf: 6(a) is the M2, 6(b) is the S2, and 6(c) is the K1, heights in m (After: Reynolds, 1993).

Waters from the Gulf of Oman flow northward along the Iranian coastline against the prevailing winds (Chao et al., 1992). Outflow from the Persian Gulf follows the coast of the United Arab Emirates and that of the Musandam Peninsula where it once again joins the Gulf of Oman. This directional flow results from the cyclonic circulation in the southern portion of the Persian Gulf. Chao et al. (1992) noted that as the waters from the Gulf of Oman move north, "they become cooled and more concentrated then eventually sink and flow out of the gulf as a deep countercurrent."

The inflow from the SOH to the Gulf is evidenced to be strongest in summer, at about 20 cm/s, and weakest in spring and autumn, at about 10 cm/s (Chao et al., 1992). Kampf and Sadrinasab (2006) showed that the strong outflow of dense bottom water in late spring and summer is in conjunction with peak Indian Ocean Surface Waters (IOSW)

11

inflow.   By analyzing upward looking acoustic doppler current profiler (ADCP) measurements in the SOH, from December 1996 to March 1998 Kampf and Sadrinasab (2006) were able to conclude that the bottom outflow was correlated with surface inflow.

3.   Temperature and Salinity

Sea surface temperature in the SOH is driven by the temperature of the IOSW inflow from the GOO. This temperature ranges from 22 to 38 degrees Celsius. During autumn and winter months the IOSW is ~22 deg C, climbing to a range reaching ~28 deg C in spring, and maintaining a 37 to 38 deg C surface temperature during the summer months (Kampf and Sadrinasab, 2006).

Due to the increased evaporation in the southern portion of the Persian Gulf the waters are more saline along the Arabian Peninsula than on the Iranian side producing a haline circulation. The salinity contrast is most evident where the Persian Gulf meets the Strait of Hormuz where the waters from the Gulf of Oman enter (Chao et al, 1992).

Flow of IOSW enters the Gulf through the SOH and follow the Iranian coast northward against the predominant winds, cooling and sinking along the way, creating a sub-surface counter current (Kämpf and Sadrinasab, 2006). Due to the density driven cyclonic flow in the southern portion of the Gulf, surface water stagnates around Qatar. Evaporation and sinking produces hypersaline water; which then forms a dense, bottom flow to the northwest and out the SOH.

Salinity distribution in the Gulf is seasonal. As seen in Figure 7, the inflow of IOSW from the SOH (purple colored portion of the cross-sections) increases in the late spring and into the summer and leads to the formation of a summer salinity front (Kämpf and Sadrinasab, 2006). The presence of the front can be identified where the 39 salinity contour follows the 40 m depth contour (Kämpf and Sadrinasab, 2006). Salinity distribution in the SOH is generally consistent year-round at 36.5 to 37 (Chao et al., 1992).
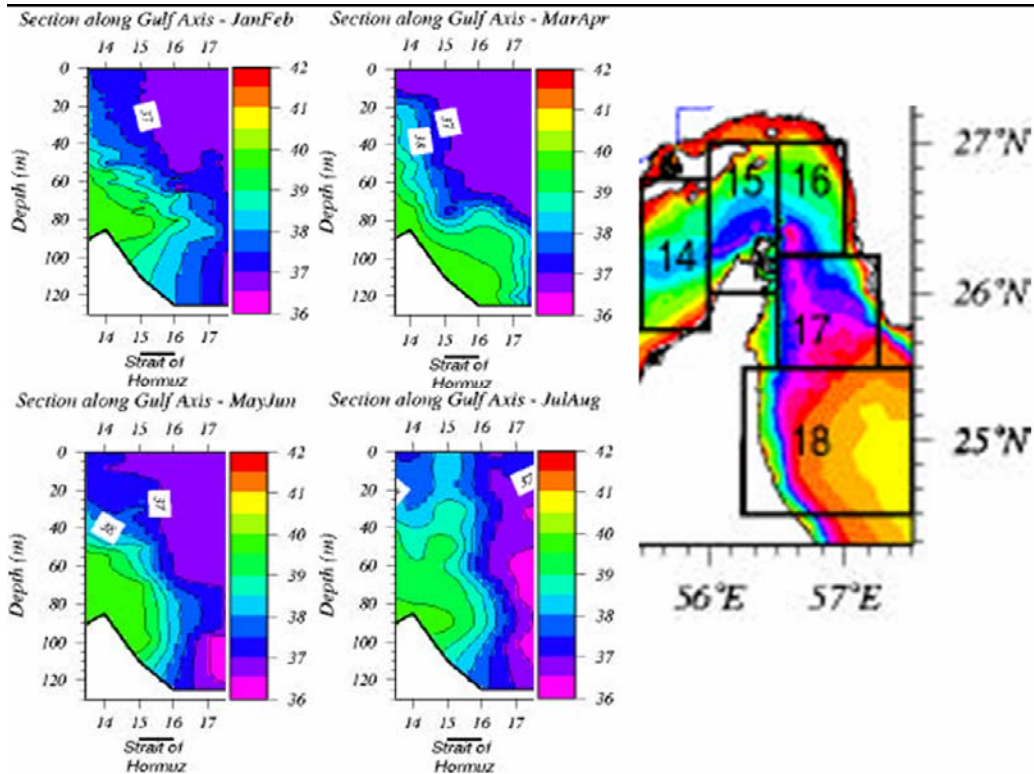
Figure 7.　　　Salinity cross sections along the axis of the Gulf through the SOH in two month sections. Averaged sample data over several years (from the 1940s to the 1990s) obtained from the U.S. Naval Oceanographic Office's Master Oceanographic Observations Data Set (MOODS)). The numbers on the x-axis of the cross-sections correspond to the boxes in the axis of the SOH. Notice the fresh IOSW intrusion beginning in spring and retreating in summer (After: Swift and Bower, 2002).

4.　　　Bathymetry

The Strait of Hormuz is characterized by a steep drop from the mountains of the Musandam peninsula, from the south to north, to a depth in excess of 100 m, which looks much like a groove just off the Omani coastline. Gradual shoaling from south to north towards the Iranian coast, where the waters become as shallow as 20 m (Reynolds, 1993) towards Bandar Abbas, characterizes the tectonic subduction of the region. This subduction is much like that of the Gulf basin but in a mirror image. The Gulf shoals to the south rather than to the north.

The SOH is a stark contrast to the GOO as it is much shallower. Difference of Bathymetry is easily seen in Figures 8 and 9. Heading out of the SOH, the waters gradually deepen to in excess of 100 m and rapidly deepen to depths in excess of 2000 m upon entering the GOO.
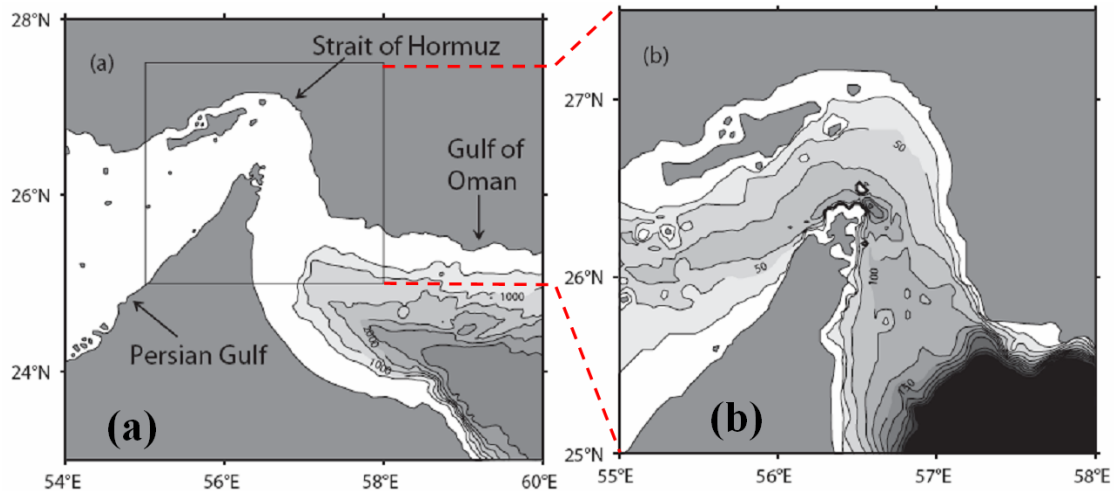
Figure 8. (a) Chart of the eastern Persian Gulf, Strait of Hormuz, and the Gulf of Oman. Bathymetry is shaded in 500-m intervals. (b) Expanded view of the Strait of Hormuz and the northwestern Gulf of Oman (area shown by box in Figure 3a). Bathymetry is contoured in 25 m intervals to 300 m (After: Bower et al., 1999).
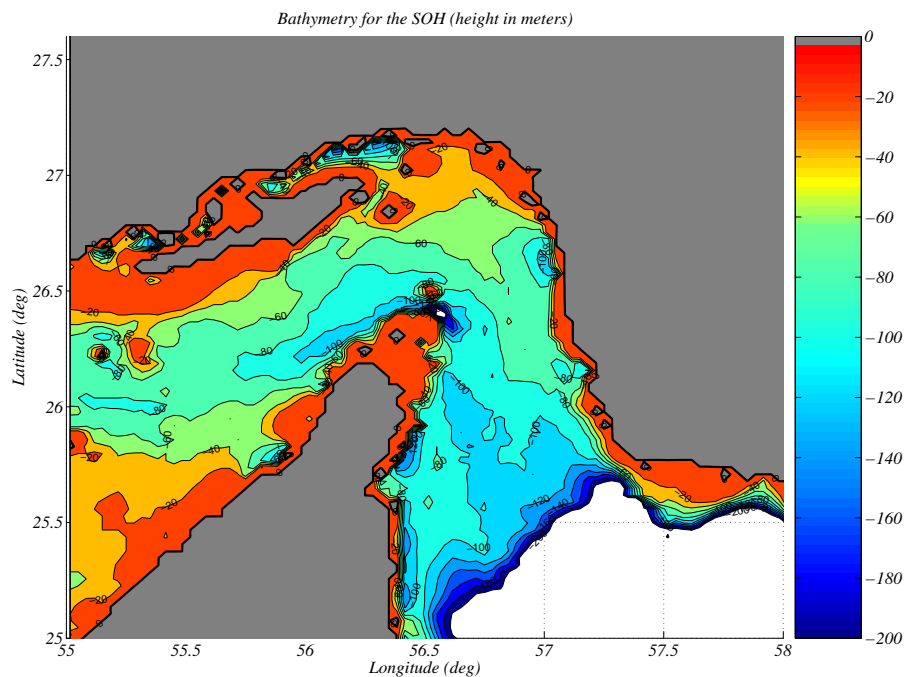
Figure 9. Bathymetry from the Gulf, through the SOH and to the beginning of the GOO. The depth is in increments of 20 m down to 200 m. The white areas signify where the depth exceeds 200 m.

C. MILITARY SIGNIFICANCE

For most Americans the name "Persian Gulf" brings to mind the current crisis America is facing in Iraq and maybe even the first war with Iraq in the 1990s. However,

due to its importance to trade, the SOH has been vied over since the establishment of world trade routes to the Persian Gulf states even from the time of the early sixteenth century (Metz, 1993).

In the last two decades, the Persian Gulf has been a battlefield for such territorial disputes as: the Iran-Iraq War (1980-88), the Iraqi invasion of Kuwait in August of 1990 (also known as the first Gulf War), and a longer ongoing dispute over three islands at the western entrance to the Straight of Hormuz (Kreil, 2004).

Originally belonging to members of the United Arab Emirates, Iran claimed and militarily occupied the three islands of Abu Musa, Greater Tunb (UAE Tumb al Kubra or Iranian Bozorg Tunb), and Lesser Tunb (UAE name: Tunb as Sughra, Iranian name: Kuchak Tunb) just 48 hours prior to the declaration of the establishment of the UAE in November 1971. The Tunbs are lawfully part of the Ra's al-Khaimah emirate and Abu Musa is part of the Sharjah emirate. This is an ongoing dispute due to the lack of military force on the part of the UAE as well as reluctance from the United Nations Security Council to interfere, although the claims of the emirates were affirmed by the UN (www.uaeislands.com; CIA, 2007; and Metz, 1993).

The Gulf is primarily a national interest due to the dependence on the oil and natural gas produced there. The flow of commerce through the SOH is the lifeblood of most of the nations of the world. It has been the interest of the world to ensure the flow of oil is not impeded by war and conflict. It is in that interest that the U.S. and European states agreed to escort convoys of Kuwaiti oil tankers (under U.S. flags) and cleared the area of mines during the Iran-Iraq war (Anderson et al., 1987). Due to the relationship the U.S. shared with Kuwait, the U.S. again utilized the waters of the Gulf for military patrols during and after the Iraqi invasion of Kuwait was turned back. The U.S. has maintained a presence in the region ever since. Due to recent events in Iraq, there is an increased presence of Western allied forces in the Gulf. Allied forces provide security with maritime patrol efforts as well as detachments aboard the oil platforms of Iraq. Boarding and searching of vessels in and around the Gulf is common.

The Persian Gulf is not the only site of armed conflict. On 18 April 1988, the U.S. Navy struck the Iranian forces in and around the Strait of Hormuz during Operation

Praying Mantis (Winkler, 2003). Hostilities were in retaliation for mine-laying by Iran, such as the 14 April mining of the USS Samuel B. Roberts (FFG-58). The Navy sank two Iranian warships and six high-speed patrol craft in the operation. Another incident that same year was the downing of Iran Air 655 by the USS Vincennes (CG-49) (McCarthy, 1991).

The presence of Western nations' navies is a constant irritant to the government of Iran; which has rattled its saber via military exercises and surface to surface missile testing (Diba, 2006). Iran claims half of the Persian Gulf and Strait of Hormuz as territorial waters (CIA, 2007). The presence and transit of U.S. war vessels is closely watched and barely tolerated.

Military presence is economically important as well as important to preventing hostilities. Security provided by the sheer presence of a strong navy provides investors confidence in the future of oil. Looney (2002) reported on a study undertaken at the Naval Postgraduate School which reflected that an increased U.S. naval forward presence had an economic benefit based on the trends in oil futures and amount of naval presence. The study linked oil price effects associated with naval forward presence and crisis response to changes observed in major economic indicators. When this economic model was applied to three cases of forward engagement and crisis response it revealed that when the oil futures markets became aware of naval forward engagement/crisis response, oil prices dropped. Since oil prices were stabilized or lowered during the crises, it proved that forward naval presence provides marked economic benefits to the U.S. economy. In dollar amounts, they estimated that naval presence in Desert Storm provided $55.22 billion worth of economic benefits in terms of the Gross Domestic Product (GDP) of the U.S., in the 1994 Iraq-Kuwait border incident yielded $7.13 billion, and during the 1987 Gulf shipping crisis (during the Iran-Iraq War) produced $5.01 billion. In terms of world income, they assert that the opening of Desert Storm alone is likely to have provided up to an $86.8 billion increase (in terms of GDP) (Looney, 2002).

III. MODELS

This thesis utilizes physical-chemical models to predict mine drifting and oil spill dispersion. First, the ocean and the atmospheric models are used to assimilate the observed in-situ and satellite data and to generate synoptic fields for the physical environment, which are the inputs to the oil fate/dispersion model. Second, the oil fates/dispersion model is utilized to run oil spill scenarios in various regimes of current and wind determined from the ocean and atmospheric models. Third, the oil fate/dispersion model is used to run oil spill scenarios in the same locations with only climatology data as input. Lastly, the Lagrangian drift model is used to predict the mine drifting pattern also utilizing the model fields and climatology data. The value-added to naval operations (mine drifting and oil spill) is determined through using the synoptic winds and currents as the input into the oil spill/mine drift models versus using the climatological winds and currents.

A.   SWAFS

As stated by Clifford et al. (1994), SWAFS is an operational nowcast/forecast system used at NAVOCEANO. It is a numerical ocean forecast system that has been applied to several semi-enclosed basins (such as the Gulf). It was constructed for the purpose of predicting the current and salinity structure in both deep and very shallow water. The modeling works on a real-time basis and is designed to function as an analog to a short-term weather prediction system. The modeling system is built around an established and well-tested numerical model of ocean circulation, designed expressly for coastal oceanography. The model is forced in near-real time with wind-stresses and air-sea thermohaline fluxes derived from operational meteorological forecast models. Remotely sensed and in situ temperature and salinity measurements, also available in near-real time, are continually assimilated into the forecast fields (Clifford et al., 1994).

Built around a three dimensional primitive equation numerical circulation model as its dynamical core, the SWAFS model is an upgraded version of the Princeton Ocean

Model (POM) that has been converted to Message Passing Interface (MPI) code, and includes Lagrangian trajectory simulation companion codes (Clifford et al., 1994).

1. Core Physics

The core of the model is a primitive equation, three-dimensional ocean forecast model commonly called the Princeton Ocean Model, whose major attributes include: 1) time-dependent, three-dimensional forecasts of temperature, salinity, density, free-surface elevation, and the three velocity components, 2) an Arakawa "C" horizontal grid and vertical coordinates scaled by the bottom depth, 3) complete thermodynamics so that surface thermohaline fluxes can be specified, and 4) an imbedded turbulence closure submodel for the purpose of yielding surface and bottom Ekman layers, assuming sufficient vertical resolution (Blumberg and Mellor, 1989).

a. Basic Equations of the POM

The following is an overview of the basic equations of the POM taken from the users guide (Mellor, 2004). Sigma coordinates, a necessary attribute to the model for dealing with bottom topography as encountered in estuaries or over continental shelf breaks, together with the turbulence submodel, produce realistic bottom boundary layers which are important to coastal waters and tidally driven estuaries. The basic equations are cast in a bottom-following sigma coordinate system as seen in Figure 10.
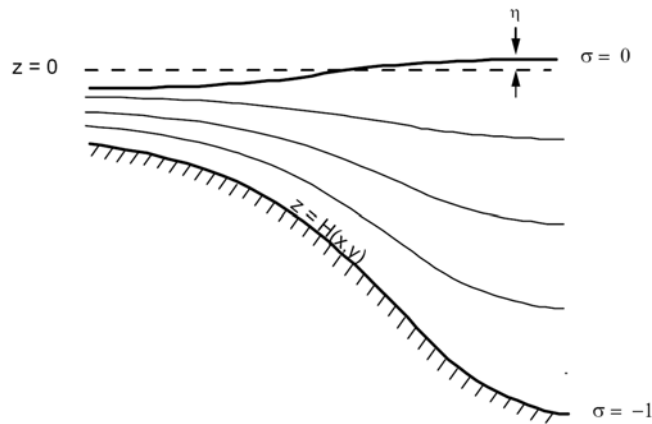
Figure 10.   The sigma coordinate system. (From: Mellor, 2004)

The derivation will not be exercised here as it is well documented. The sigma coordinates are based on the transformation,

$$x^* = x, \; y^* = y, \; \sigma = \frac{z - \eta}{H + \eta}, \; t^* = t, \tag{3.1}$$

18

where x, y, and z are the conventional Cartesian coordinates; $D \equiv H + \eta$ where $H(x, y)$ is the bottom topography and $\eta(x, y, t)$ is the surface elevation. Thus, σ ranges from $\sigma = 0$ at $z = \eta$ to $\sigma = -1$ at $z = H$. Let (U, V) be the horizontal velocity components; ρ be the density; (K_M, K_H) be the eddy viscosity and thermal diffusivity. After conversion to sigma coordinates and deletion of the asterisks, the continuity equation is given by

$$\frac{\delta DU}{\delta x} + \frac{\delta DV}{\delta y} + \frac{\delta \omega}{\delta \sigma} + \frac{\delta \eta}{\delta t} = 0. \tag{3.2}$$

The horizontal momentum equations are given by

$$\frac{\partial UD}{\partial t} + \frac{\partial U^2 D}{\partial x} + \frac{\partial UVD}{\partial y} + \frac{\partial U\omega}{\partial \sigma} - fVD + gD\frac{\partial \eta}{\partial x} + \frac{gD^2}{\rho_0} \int_\sigma^0 \left[\frac{\partial \rho'}{\partial x} - \frac{\sigma'}{D}\frac{\partial D}{\partial x}\frac{\partial \rho'}{\partial \sigma'} \right] d\sigma'$$
$$= \frac{\partial}{\partial \sigma}\left[\frac{K_M}{D}\frac{\partial U}{\partial \sigma} \right] + F_x \tag{3.3}$$

$$\frac{\partial VD}{\partial t} + \frac{\partial UVD}{\partial x} + \frac{\partial V^2 D}{\partial y} + \frac{\partial V\omega}{\partial \sigma} + fUD + gD\frac{\partial \eta}{\partial y} + \frac{gD^2}{\rho_0} \int_\sigma^0 \left[\frac{\partial \rho'}{\partial y} - \frac{\sigma'}{D}\frac{\partial D}{\partial y}\frac{\partial \rho'}{\partial \sigma'} \right] d\sigma'$$
$$= \frac{\partial}{\partial \sigma}\left[\frac{K_M}{D}\frac{\partial V}{\partial \sigma} \right] + F_y \tag{3.4}$$

The heat and salt equations are represented by

$$\frac{\partial TD}{\partial t} + \frac{\partial TUD}{\partial x} + \frac{\partial TVD}{\partial y} + \frac{\partial T\omega}{\partial \sigma} = \frac{\partial}{\partial \sigma}\left[\frac{K_H}{D}\frac{\partial T}{\partial \sigma} \right] + F_T - \frac{\partial R}{\partial z} \tag{3.5}$$

$$\frac{\partial SD}{\partial t} + \frac{\partial SUD}{\partial x} + \frac{\partial SVD}{\partial y} + \frac{\partial S\omega}{\partial \sigma} = \frac{\partial}{\partial \sigma}\left[\frac{K_H}{D}\frac{\partial S}{\partial \sigma} \right] + F_S. \tag{3.6}$$

The eddy viscosity K_M and thermal diffusivity K_H are expressed by

$$K_M = lqS_M, \quad K_H = lqS_H$$

where l is the mixing length, q is the turbulent speed, and S_M and S_H are stability functions which are analytical derived, algebraic relation functionally dependent upon $\partial U / \partial z$, $\partial V / \partial z$, $\partial \rho / \partial z$, q, and l. The level-2 turbulent closure scheme is used:

$$\frac{\partial q^2 D}{\partial t} + \frac{\partial Uq^2 D}{\partial x} + \frac{\partial Vq^2 D}{\partial y} + \frac{\partial \omega q^2}{\partial \sigma}$$
$$= \frac{\partial}{\partial \sigma}\left[\frac{K_q}{D}\frac{\partial q^2}{\partial \sigma} \right] + \frac{2K_M}{D}\left[\left(\frac{\partial U}{\partial \sigma}\right)^2 + \left(\frac{\partial V}{\partial \sigma}\right)^2 \right] + \frac{2g}{\rho_0}K_H\frac{\partial \tilde{\rho}}{\partial \sigma} - \frac{2Dq^3}{B_1 \ell} + F_q \tag{3.7}$$

$$\frac{\partial q^2 \ell}{\partial t} + \frac{\partial U q^2 \ell}{\partial x} + \frac{\partial V q^2 \ell D}{\partial y} + \frac{\partial \omega q^2 \ell}{\partial \sigma} = \frac{\partial}{\partial \sigma} \left[\frac{K_q}{D} \frac{\partial q^2 \ell}{\partial \sigma} \right]$$

$$+ E_1 \ell \left(\frac{K_M}{D} \left[\left(\frac{\partial U}{\partial \sigma} \right)^2 + \left(\frac{\partial V}{\partial \sigma} \right)^2 \right] + E_3 \frac{g}{\rho_0} K_H \frac{\partial \tilde{\rho}}{\partial \sigma} \right) - \frac{D q^3}{B_1} \tilde{W} + F_\ell$$

(3.8)

The transformation to the Cartesian vertical velocity is given by

$$W = \omega + U \left(\sigma \frac{\partial D}{\partial x} + \frac{\partial \eta}{\partial x} \right) + V \left(\sigma \frac{\partial D}{\partial y} + \frac{\partial \eta}{\partial y} \right) + \sigma \frac{\partial D}{\partial t} + \frac{\partial \eta}{\partial t} ,$$

(3.9)

which satisfies the no-flow boundary conditions at the surface and the bottom.

The wall proximity function is prescribed according to

$$\tilde{W} = 1 + E_2 \left(\ell / kL \right)$$

where

$$L^{-1} = \left(\eta - z \right)^{-1} + \left(H - z \right)^{-1} , \partial \tilde{\rho} / \partial \sigma \equiv \partial \rho / \partial \sigma - c_S^{-2} \partial p / \partial \sigma ,$$

and c_S is the speed of sound. In equations 1.3 and 1.4, mean density (ρ_{mean}) must be subtracted from ρ in order to obtain the density perturbation (ρ') before performing the subroutine that calculates the baroclinic, vertical integrals involving density in (1.3) and (1.4). This procedure removes most of the truncation error in the transformed baroclinic terms which arise due to the subtraction of the large terms involving $\partial \rho / \partial x$ and $D^{-1} \left(\partial D / \partial x \right) \sigma \partial \rho / \partial \sigma$ in (1.3) and similarly in (1.4).

In order to maintain a valid bottom boundary in the face of sometimes large horizontal diffusivity in a sigma coordinate system can result in the creation of false vertical fluxes even when isotherms and isohalines are flat lined in the Cartesian coordinates. Mellor (2004) uses a Smagorinsky horizontal diffusivity to alleviate this condition.

2. Forcing

The circulation model is forced using wind speeds, air temperatures, and vapor pressures used to derive the wind stress and air-sea thermohaline fluxes, which are then used to drive the ocean forecast model. These inputs come from COAMPS running at the

Fleet Numerical Meteorology and Oceanography Center. The meteorological forecasts and the assimilated data are available in near real time, and the circulation modeling system is designed to make continual up-to-date forecasts (Clifford et al., 1994).

3.   **Data Assimilation**

The other major element of SWAFS is a data assimilation module (see Figure 11) for the circulation model along with associated databases of in situ temperature and salinity measurements, sea surface temperatures (SST), tides, current, as well as meteorological fluxes.

As this is an Operational ocean model, it is constantly changing in order to improve model accuracy and skill. Hence, the availability of up-to-date documentation is nonexistent. Through a representative from NAVOCEANO, the following description of the current data assimilation module configuration was obtained.

Data Assimilation for SWAFS Circulation Model
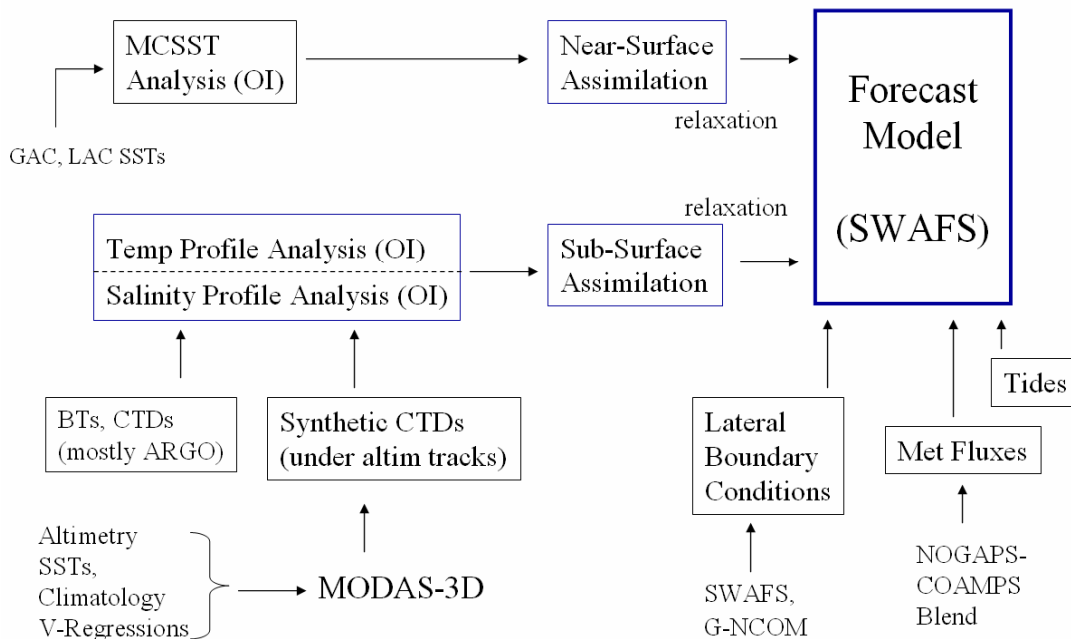
Figure 11.   Data Assimilation structure for SWAFS. (From: Haeger, 2006, personal communication)

SWAFS runs a 48 hour forecast and a 24 hour hindcast (Figure 12). The hindcast is utilized for incorporating "real-time" data into the model. Due to the paucity and

spatial variability of observations in the oceans, it is necessary to incorporate data into the hindcast from a variety of sources. From Figure 11, it can be seen that SWAFS incorporates data in the following five methods: 1) Tides, 2) atmospheric forcing and fluxes, 3) lateral boundary conditions, 4) sub-surface assimilation, and 5) near-surface assimilation.

Tides inputs are an option if needed only. The coastal tide stations are "turned on" only if tide amplitude is significantly out of phase. Atmospheric forcing is directly input to the model via atmospheric model fields from NOGAPS or COAMPS. It can be seen in Figure 11, that there is a NOGAPS-COAMPS "Blend" that is used for input. That simply means that a NOGAPS outer nest is utilized to encompass two COAMPS fields that meet up at the boundary to ensure reduction of boundary error propagation.

Sub-surface data assimilation is accomplished by combining in situ observations and synthetic observations obtained from the Modular Ocean Data Assimilation System (MODAS-3D). MODAS utilizes near-real time altimetry, sea surface temperature (SST), and a climatological database to synthesize equally spaced conductivity/temperature/depth (CTD) observations. The synthetic CTDs are more accurate under the altimetry tracks. These, combined with the in-situ data via optimum interpolation (OI), are assimilated into the model utilizing what is termed as "relaxation" or "nudging" the model.

The near-surface data assimilation is accomplished by utilizing MCSSTs from either the Global or Local Area Coverage (GAC, LAC) satellites for input to the model via the "relaxation" technique as well. Correlation scales (both of time and length) are calculated and determine how far and long the data can be spread around. Time correlations are related to how much the observations are weighted. The relaxation technique can be seen in Figure 12, where observations are combined with the "first guess" field from the previous day's run to make the 24 hr hindcast of the current run. Time correlations or weighting is high at this time because the hindcast is essentially the "truth" of the past. Observations are also re-entered into the run at the time zero and 24 hr forecast with time correlation reducing the further from the hindcast it gets. This method was empirically derived by Charles Horton at NAVOCEANO for every basin.

Vertical regressions are calculated in MODAS with the inputs of sea surface height, sea surface temperature, Julian Day, and latitude and longitude. It is these vertical regressions that determine the correlation time scales. Furthermore, it is ocean basin dependent. Meaning, that depending on the ocean basin one is dealing with, a better regression is achieved by "turning off" altimetry, SST, or both on continental shelves or regional seas. The aforementioned method was developed by the Navy Research Lab when it conducted the confidence level assessment for MODAS (CLAM) in 1999 to establish just how to run MODAS in each region (Fox et al., 2002).
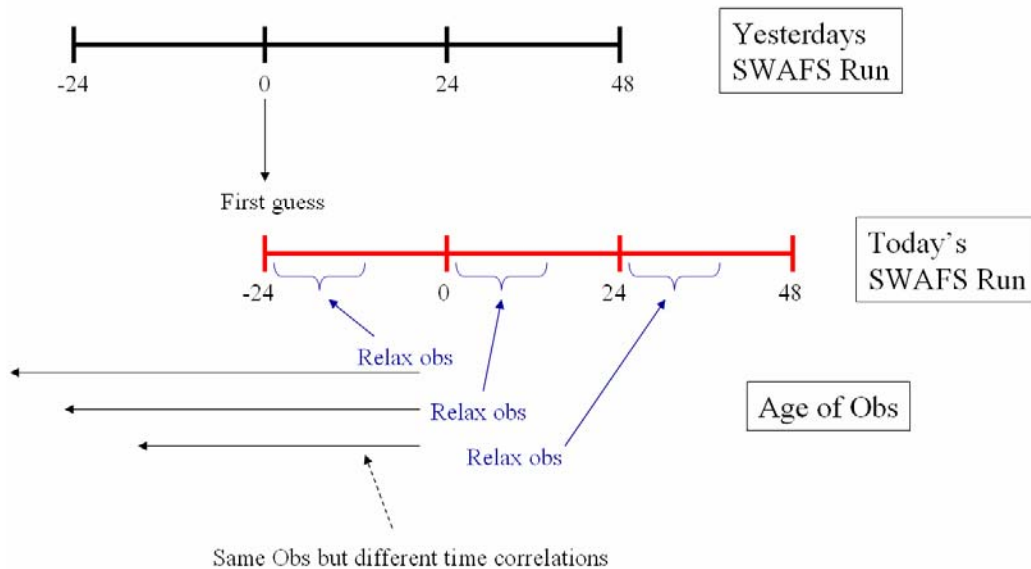
Figure 12.   SWAFS model run cycle. (From: Haeger, 2006, personal communication)

B.   COAMPS

The Coupled Ocean/Atmosphere Mesoscale Prediction System (COAMPS) is an operational non-hydrostatic regional model developed by the Naval Research Laboratory (NRL) in 1996 and made operational by 1998 (Chen et al., 2003). The following overview of COAMPS is taken directly from Chen et al. (2003).

The atmospheric component of COAMPS can be used for real-data or idealized applications. As applied to this thesis, the COAMPS analysis can use global fields from

the current Navy Operational Global Atmospheric Prediction System (NOGAPS) analysis or the most recent COAMPS forecast as the first-guess field (NOGAPS is used as the initial first guess in Figure 13). Observations from a wide variety of sources such as aircraft, weather station, ship, and satellites are blended with these first-guess fields to generate the current COAMPS analysis. The analysis field is the first major component in the atmospheric model since it is required in order to prepare the initial field and boundaries necessary for the other major component, the forecast.
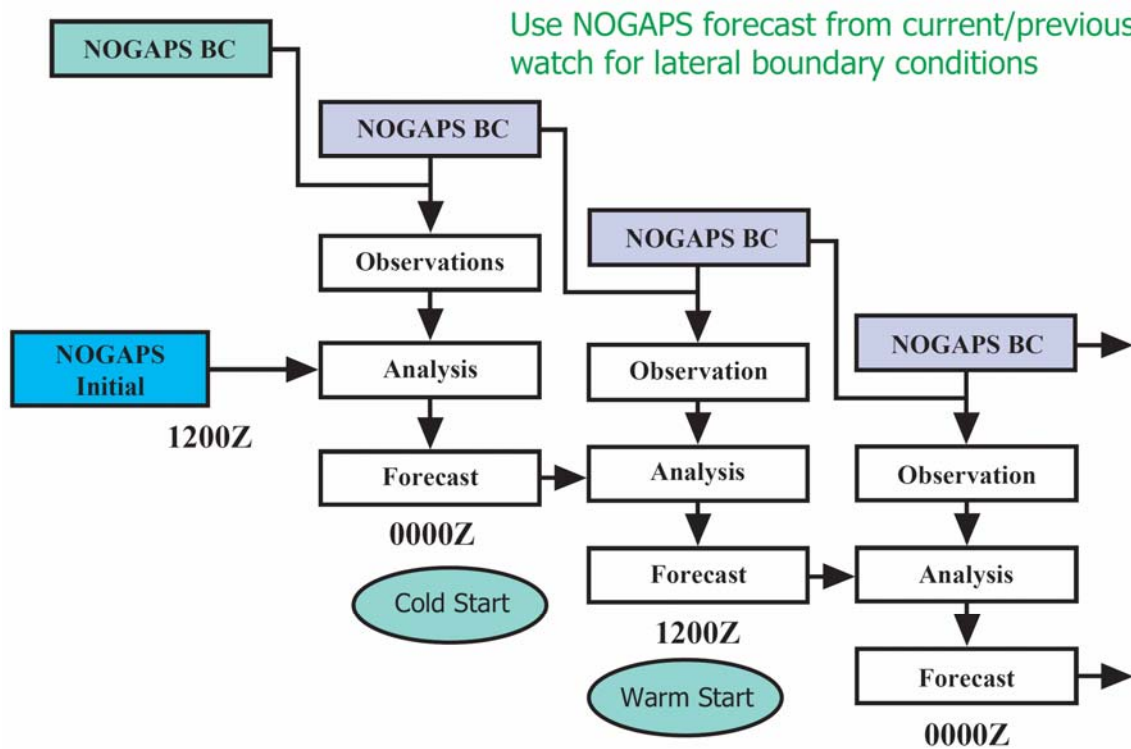
Figure 13.   Example of COAMPS data assimilation cycle. This example has an update cycle of 12 hours. (From: Chen et al., 2003)

1.   Grid Spacing

The atmospheric model uses nested grids to achieve high resolution for a given area; it contains parameterizations for subgrid scale mixing, cumulus parameterization, radiation, and explicit moist physics. It is these model features that allow the model to resolve such small scale features as mountain waves, terrain-induced circulations, and land-sea breezes.

Grid spacing is staggered in both the horizontal and vertical. The horizontal grid is staggered using an Arakawa-C as seen in Table 2, where π is representing scalar variables defined in the center of the table (grid box). The u and v components are one-half grid intervals between the mass points in the x and y direction. Kantha and Clayson (2000) say that the C grid scheme is "eminently suited" to the calculation of pressure gradients and divergence but submit that the Coriolis terms require averaging for the finite-differencing since they are not collocated on the grid (as is the case in Arakawa A grid spacing). All derivatives are computed to second-order accuracy, with the exceptions of the horizontal diffusion and an option for fourth-order accurate horizontal advection. By using fourth order accurate horizontal diffusion, the damping is much more specific to the removal of high-frequency modes.

$\pi_{i-1,j+1}$	$u_{i-1,j+1}$	$\pi_{i,j+1}$	$u_{i,j+1}$	$\pi_{i+1,j+1}$
$v_{i-1,j}$		$v_{i,j}$		$v_{i+1,j}$
$\pi_{i-1,j}$	$u_{i-1,j}$	$\pi_{i,j}$	$u_{i,j}$	$\pi_{i+1,j}$
$v_{i-1,j-1}$		$v_{i,j-1}$		$v_{i+1,j-1}$
$\pi_{i-1,j-1}$	$u_{i-1,j-1}$	$\pi_{i,j-1}$	$u_{i,j-1}$	$\pi_{i+1,j-1}$

Table 2.   Arakawa-Lamb scheme C staggering (After: Chen et al., 2003).

The vertical coordinate system is a terrain-following sigma-z system. In the sigma-z system the number of sigma levels do not change but the distance between them does according to the height of the terrain (z_{sfc}). The transformation of the vertical coordinate following Gal-Chen and Somerville (1975) is applied to map the lowest coordinate surface to an irregular lower boundary

$$\sigma = z_{top}\left(\frac{z - z_{sfc}}{z_{top} - z_{sfc}}\right),$$
(3.10)

where z_{top} is the depth of the model domain and z_{sfc} is the height of the topography. The *w*-component (vertical velocity), is coincident with the mass variables and is defined at the model sigma levels. COAMPS gets terrain information from the one kilometer grid spaced, Digital Terrain Elevation Data (DTEDs) series of models which are products of the U. S. National Geospatial Intelligence Agency (NGA). The COAMPS model run by the Navy utilizes 30 sigma levels. Chen et al. (2003) note that the utilization of more sigma levels may be appropriate if one desires to run high resolution over steep topography in order to increase vertical resolution.

2. Core Physics

a. Basic Equations

The atmospheric portion of the COAMPS models is comprised of the nonhydrostatic, fully compressible equations of motion following Klemp and Wilhelmson (1978). The adiabatic equations are developed using the equation of state:

$$p = \rho R_D T_v, \tag{3.11}$$

where p is the pressure, ρ is the density, R_d is the dry gas constant, the virtual temperature, T_v is

$$T_v = T\left(1.0 + 0.608 q_v\right), \tag{3.12}$$

where T is the temperature and q_v is the specific humidity, and the Exner function,

$$\pi = \left(\frac{p}{p_{00}}\right)^{R_d/C_p}, \tag{3.13}$$

where C_p is the specific heat at constant pressure, and p_{00} the reference pressure.

Solving the fully compressible, nonhydrostatic equations explicitly is extremely computational expensive because of the presence of sound waves that severely limit the time step required to maintain computational stability. One approach for addressing this problem is to treat the sound wave modes separately on a small time step following Klemp and Wilhelmson (1978) and Skamarock and Klemp (1992).

26

The equations are solved using the centered-in-time or leapfrog scheme (Haltiner and Williams 1980). Typically, the time splitting due to the leapfrog scheme is not problematic (e.g., Klemp and Wilhelmson, 1978). However, a Robert (1966) time smoother is applied to assure that any tendencies that may tend to decouple the odd and even time steps are stable. For any variable ϕ, the Robert time filter is applied as

$$\left.\begin{aligned} \phi^{*t+\Delta t} &= \phi^{t-\Delta t} + 2\Delta t \phi^{*t} \\ \phi^{t} &= \phi^{*t} + \alpha\left(\phi^{*t+\Delta t} - 2\phi^{*t} + \phi^{t-\Delta t}\right) \end{aligned}\right\}. \tag{3.14}$$

The first equation corresponds to the leapfrog step for

$$\partial\phi \big/ \partial t = F, \tag{3.15}$$

with the asterisk corresponding to provisional terms that have not yet been smoothed through application of the second step. The net effect is to produce strong damping of the computational mode, while the physical mode is generally not affected (Asselin 1972). Here, α is taken as 0.2.

b. Boundary Layer/Turbulence Equations

For boundary layer, COAMPS uses a level-2.5 turbulent closure scheme (Mellor and Yamada, 1982) that solves both a prognostic equation for turbulent kinetic energy (TKE) and diagnostic equations for second-moment quantities primarily such as fluxes of heat, moisture, and momentum. The level-2.5 scheme computes all of the fields necessary for solving the TKE equation, including boundary layer depth, turbulent mixing length, flux, Richardson number, and eddy coefficients. In addition, the scheme incorporates the influence of boundary layer cloudiness. TKE is calculated using,

$$\begin{aligned} &\frac{D}{Dt}(e) - \frac{\partial}{\partial z}\left(K_e \frac{\partial}{\partial z}(e)\right) = \\ &K_M\left(\frac{\partial U}{\partial z}\right)^2 + K_M\left(\frac{\partial V}{\partial z}\right)^2 - \beta g K_H \frac{\partial \theta}{\partial z} - \frac{(2e)^{3/2}}{\Lambda_1} + U\frac{\partial}{\partial y}(e)^* + V\frac{\partial}{\partial y}(e)^* \end{aligned} \tag{3.16}$$

where U and V denote the mean horizontal velocity field, β is the coefficient of thermal expansion, θ is potential temperature, g is the acceleration due to gravity, Λ_1 is the dissipation length scale, u', v', and w' denote the components of the three dimensional

turbulent velocity field, and $K_{H,M,e}$ are eddy coefficients. The left side of the equation holds the diffusion terms; where, the left is diffusion and the right is turbulent diffusion. On the right hand side, the first two terms are shear (or mechanical production of TKE), then the buoyant production of TKE, the dissipation term equal to TKE raised to the 3/2 power divided by the dissipation length scale, and the last two are the advective terms used only when the grid increment is less than 10 km (as in the fields provided for this study at 2 km).

The prognostic variable is

$$e = \overline{\left(u'^s + v'^s + w'^s\right)}/2 . \tag{3.17}$$

In the TKE expression,

$$K_{H,M,e} = S_{H,M,e} l\sqrt{2e} . \tag{3.18}$$

where $S_{H,M}$ are polynomial functions of the flux Richardson number, S_e is a constant, and l is the master length scale. The TKE equation is solved explicitly, omitting the diffusion term. Then the diffusion term is solved implicitly.

c.   *Surface Layer Parameterization*

The surface layer parameterization follows the Louis (1979) scheme, which uses polynomial functions of the bulk Richardson number to directly compute surface sensible heat flux, surface latent heat flux, and surface drag. The bulk Richardson number is defined as

$$Ri_B = \frac{gz\Delta\theta}{u^2\Theta} , \tag{3.19}$$

where g is the acceleration due to gravity, z is the reference elevation (equal to 10 m in COAMPS), $\Delta\theta$ is the air-sea temperature difference, u is the wind speed at the reference elevation, and Θ is the mean potential temperature over the depth of the surface layer.

Surface roughness (Fairall et al., 1996) is obtained by

$$z_0 = c_0 \frac{u_*^2}{g} + c_v \frac{v}{u_*} , \tag{3.20}$$

where c_0 is the Charnock constant, u^* is the friction velocity, g is the acceleration due to gravity, c_v is a constant, and v is the molecular viscosity. The first term is the Charnock relation that accounts for high wind (aerodynamically rough conditions), while the second term accounts for low wind (aerodynamically smooth conditions).

Although the equations are solved on a staggered, scheme C grid, the COAMPS analysis is performed on the Arakawa-Lamb scheme A grid (i.e., no grid staggering). The bicubic spline interpolation is used to interpolate the analyzed fields to the C grid within the forecast model code.

3.   Data Assimilation

The COAMPS analysis is based on the multivariate optimum interpolation (MVOI) analysis scheme described in Goerss and Phoebus (1992) and Barker (1992). The MVOI technique utilizes both real and synthetic observational data to compute increments for the first-guess fields. COAMPS runs in a continuous update cycle; therefore, the first guess fields for the operational model come from the previous COAMPS forecast. If accomplished over a significant number of observations, utilization of this technique significantly reduces the Mean Squared Error of the analysis. The analysis variables for the MVOI are geopotential height, and the u and v wind components. Finally, the first-guess fields are adjusted based on observational data via a MVOI analysis. Observational data include the following data types: (1) Radiosonde, (2) Pibal, (3) Surface land, (4) Surface marine, (5) Aircraft, (6) Satellites (including SSM/I, Scatterometer, Sea Surface Temperature, and QUIKScat), and (7) Synthetic observations from NOGAPS.   The cutoff for data used is $\pm 3:00$ hours from the analysis time. Conventional data are subjected to quality control (Baker, 1992 and 1994) including gross check error checking and complex quality control of radiosonde observations (Gandin, 1988). Quality control of aircraft data includes sophisticated flight track checking and characteristic error detection (Pauley, 2003). Within the MVOI itself, both satellite and conventional data are further checked for quality and for consistency with neighboring observations and the model short-term forecast, which is used as a "first guess" for the analysis.

After going through quality control, the time/space adjusted model forecast variables are compared to the observations to determine differences to be input into the analysis program. The differences are then weighted by a factor based on the reliability of the observations (instrument error characteristics, for example) relative to that of the first guess. A mathematical procedure is then employed to minimize the analysis error, based on the assumed observation and model forecast error characteristics.

C.   OILMAP

OILMAP is an oil spill model system able to predict the movement and fate of oil spilled in marine or fresh water (ASA, 2006). As shown in Figure 14, the model system is made up of several integrated components. The spill model itself predicts the movement of oil on the surface as well as the distribution of oil in the environment (whether it is evaporated, in the water column, or on the shoreline). These calculations are made utilizing environmental data such as winds and currents, physical data such as proximity of shorelines, and chemical data that defines the properties of the oil spilled (ASA, 2006). This data can be input to the model and edited using the appropriate OILMAP component. Additionally, OILMAP includes an embedded Geographical Information System (GIS), which is used to store, display and analyze any type of geographically referenced data, including critical habitats, oil spill response equipment, shipping lanes, and real-time spill observations (ASA, 2006). The model does not necessarily use this data but it can prove helpful in analyzing and interpreting model results.

The model contains up to four of the model options displayed in Figure 14: trajectory and fates model, subsurface model, stochastic model, and the receptor model. Each model has unique application to oil spill management, clean up, and response.
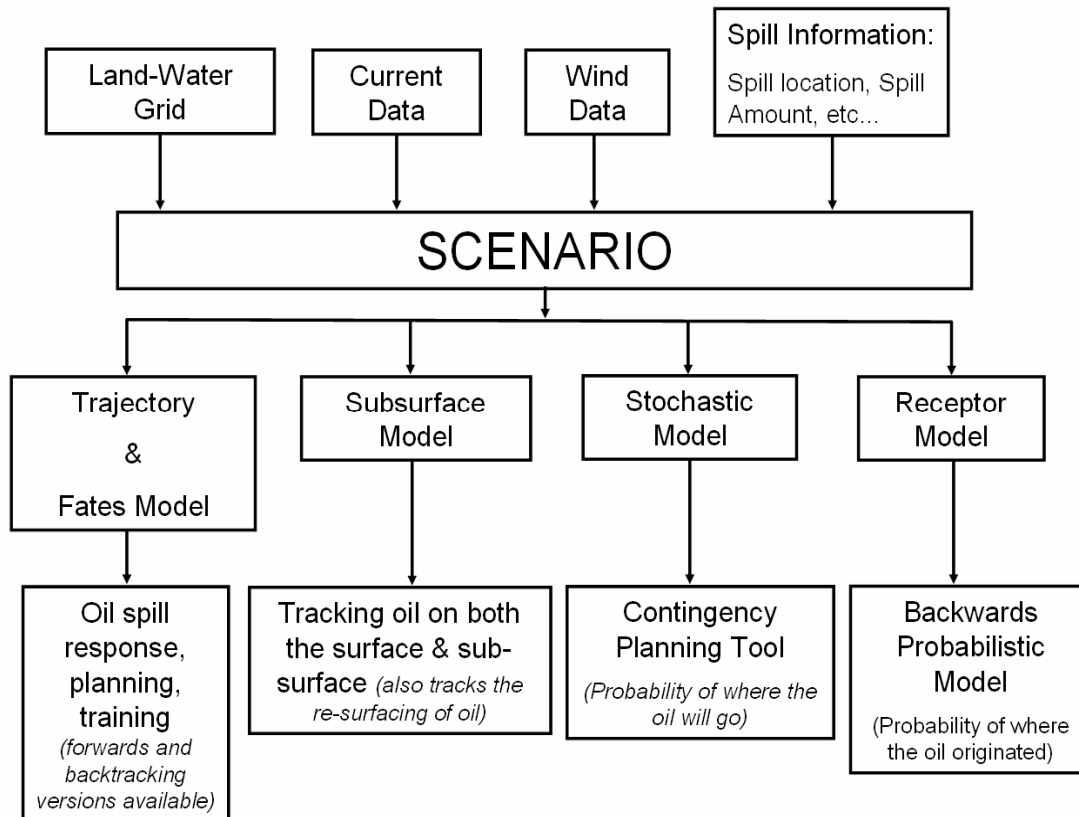
Figure 14.   OILMAP model system and integrated components. (From: ASA, 2006)

1.   Trajectory and Fates Model

The trajectory and fates model tracks the surface movement of oil and determines the distribution in various environmental compartments: water surface, atmosphere, water column, and shoreline (ASA, 2006). This is the model to be used for oil spill response. It has two modes; standard and backwards mode. "Standard" mode tracks oil forward in time and the "Backwards" mode tracks the oil backwards in time.

2.   Subsurface Model

The subsurface model tracks the movement of oil on the surface and under the water surface (ASA, 2006). Like the trajectory and fates model, it also determines the distribution of oil in the environmental compartments. Oil entrained into the water column by breaking waves is also tracked and displayed. The re-surfacing of oil is also a tracked feature.

3.   Stochastic Model

The stochastic model is a contingency planning tool used to determine the range of distances and directions oil spills from a particular site are likely to travel, given local

climatology for wind speed and direction (ASA, 2006). This model performs a large number of simulations for a given spill site, varying the wind and current conditions for each scenario. This model provides a time history of surface oiling for a large number of spill trajectories which are used to generate probabilities of which water surfaces and shoreline areas will be oiled by a release from a given site. This model helps to determine the most effective placement of response equipment.

4.   Receptor Model

This component is similar to the stochastic model, with the exception that it is run in reverse. This model allows the user to determine the origin of a spill by running a large number of simulations for a given receptor site (where oil has been washed up) (ASA, 2006). Wind and current conditions are varied for each scenario, creating a probability distribution of spill trajectories. Uses for this component include determination of sites vulnerable to oil spills and determining the source of oil deposited on the shoreline.

IV. ANALYSIS OF PHYSICAL MODEL OUTPUT

A. WIND AND CURRENT DATA

The Navy's operational models (COAMPS, SWAFS) assimilate the observational data from satellites and in-situ measurements. The model output such as winds and currents are treated as the quasi-observational and relate to current tools available to deployed units as well. By utilizing an operational source, it is intended to assess the value added by actual model fields input to a fates/dispersion model when compared to climatology.

1. COAMPS Model Fields

Archived COAMPS model fields were collected by NAVOCEANO, from FNMOC operational COAMPS runs, in one day increments and stitched together to complete six months of 10 m winds data. Each day begins at 00UTC and ends at 1800UTC. The six month window began at 00UTC February 1, 2006 and ended at 1800UTC July 31, 2006. Each day set of model fields was a single model run starting with the analysis at 00UTC and utilized the forecasts from Tau's 06, 12, and 18 to complete the day. Therefore, for each day four time steps, thus the total number of time steps was 724. The model fields were from a large area covering the Persian Gulf to the Gulf of Oman in a box of dimensions: 23N, 48E to 31N, 58E. With the spatial resolution of 27 km this amounted to a matrix of grid points 41x51 over the region.

2. SWAFS Model Fields

SWAFS model current fields, from archived runs starting at 00UTC on the morning of 01 February 2006 and continuing to 00UTC 01 August 2006, were provided from NAVOCEANO in hourly time stamps. The model fields were delivered in six one-month data packets for 0.5 m (essentially surface) current velocity fields. SWAFS makes one model run per day with a 24 hr hindcast and a forecast out to 48 hrs. Each day of data was made up by one SWAFS run from the analysis out to 23 hours in hourly increments. The operational SWAFS run is hourly and has an internal time step of 50 seconds. The model fields were from a large area covering the Persian Gulf to the Gulf of Oman in a box of dimensions: 23.489N, 47.49E to 30.485N, 57.49E. With the spatial resolution of 2 km this amounted to a matrix of grid points 202x226 over the region.

B.   STATISTICAL ANALYSIS/DATA PROCESSING

The wind fields delivered had values for 10 m winds in the "u" and "v" directions. These fields had to be combined to make velocity vectors. The temporal means were taken for velocity in both planes. Mean, refers to the sample mean taken at each grid point denoted by:

$$\overline{x}_j = \frac{\sum_{i=1}^{n_j} x_{ij}}{n_j},$$ (4.1)

where, $\overline{x}$ is the mean of the variable at grid point j, and i is the time step, and n is the number of time steps, which as stated before was 724. In this manner, the temporal mean was obtained for each of the grid points to obtain the mean winds for the entire time period of six months.

There two main methods of using the mean that were used in this research. One was to use the mean to calculate the perturbation, or "prime" values. The perturbations were obtained by normalizing the data. That is, the mean was subtracted from each of the values of u and v for each grid point since:

$$u = \overline{u} + u', \quad v = \overline{v} + v'.$$ (4.2)

In addition to the mean, discussed earlier, two other statistical methods are utilized. These methods include standard deviation and covariance. Standard deviation of a probability distribution is defined as a measure of the spread of those values. It is also the square root of variance. Mathematically, standard deviation is defined as:

$$s = \sqrt{\frac{\sum_{i=1}^{n}\left(X_i - \overline{X}\right)^2}{(n-1)}}$$ (4.3)

Standard deviation is the most common measure of statistical dispersion and measures how widely spread the values in a data set are. If the data points are close to the mean, then the standard deviation is a lower value, close to zero. As the data points move further away from the mean, the standard deviation moves further from zero. The other statistical method, covariance, is the measure of how much two variables change

together. This is different from variance, mentioned early, which measures how much a single variable fluctuates.

Covariance is computed by:

$$\text{cov} = \frac{\sum_{i=1}^{n} \left(X_i - \overline{X} \right) \left(Y_i - \overline{Y} \right)}{(n-1)} \tag{4.4}$$

for two variables X and Y. If two variables tend to vary together then the covariance between the two variables will be positive. On the other hand, if when one of them is above its expected value, the other variable tends to be below its expected value, then the covariance between the two variables will be negative. If the variables vary independent from each other, the covariance will be zero. Conversely, if the covariance is zero, the variables need not be independent.

Another important mathematical method involves matrix algebra. Specifically the covariance matrix and eigenvectors/eigenvalues of a given matrix will be discussed. If the data set has more than 2 dimensions, there is more than one covariance measurement that can be calculated. A useful way to account for the additional variances associated with each dimension is to create a covariance matrix. This matrix is composed of the covariance between elements of a vector. A covariance matrix of three dimensions would look like:

$$C = \begin{pmatrix} \text{cov}(x,x) & \text{cov}(x,y) & \text{cov}(x,z) \\ \text{cov}(y,x) & \text{cov}(y,y) & \text{cov}(y,z) \\ \text{cov}(z,x) & \text{cov}(z,y) & \text{cov}(z,z) \end{pmatrix} \tag{4.5}$$

Some points to note: Down the main diagonal, the covariance value is between the same dimensions. These values are the variances for the given dimension. The other point is that since $\text{cov}(a,b) = \text{cov}(b,a)$, the matrix is symmetrical about the main diagonal.

Since the model field data is two dimensional at particular times it is in reality a three dimensional matrix of velocities over time. Matrix algebra was thoroughly utilized to process the model fields for both analysis and formatting for input to OILMAP.

Eigenvectors are a special case of multiplying two matrices together. There are two key properties of all eigenvectors. First, all eigenvectors multiplied by a scalar are equal, since all the scalar does is make the vector longer but not change its direction. Secondly, all eigenvectors of a matrix are perpendicular, or at right angles to each other, no matter how many dimensions one has. Mathematically another term for perpendicular is orthogonal. This is important because it means the data can be expressed in terms of these perpendicular eigenvectors, instead of expressing them in terms of the x and y axes.

Another important thing to know is that when eigenvectors are found it is common to find those whose length is exactly one. This is because the length of a vector does not affect whether it is an eigenvector or not, whereas direction does. So, in order to keep eigenvectors standard, whenever an eigenvector is found it is scaled to have a length of 1, so that all eigenvectors have the same length. Eigenvalues are closely related to eigenvectors. Eigenvectors and eigenvalues always come in pairs. Eigenvalues are the multiple used to get the eigenvector back to the original length it was before being converted to a length of one.

Perturbations of the velocities gave anomaly data that could be further analyzed for patterns. One of the methods utilized was the empirical orthogonal function (EOF) or alternatively known as principal components analysis (PC). This method is very useful for analyzing data with complex spatial/temporal structures (Kaihatu et al., 1998).

As explained by Kaihatu et al. (1998), by using complex EOF analysis, one can obtain eigenfunctions that best describe the information contained within the data. Therefore, one is essentially distilling information from mountains of data. EOF eigenmodes are then ordered in terms of the percentage of the total variance described by each mode, additionally, eigenmodes are statistically uncorrelated with one another (Sirovich, 1987). Advantages of using EOF analysis for this case are: 1) only the first few modes may be necessary to accurately describe the information since they contain the most significant portion of the total variance; and 2) the significant computer memory savings involved with utilizing a relatively small set of information to describe large processes (Kaihatu et al., 1998).

C. CONVENTIONAL EOF ANALYSIS

Let a temporally and spatially varying scalar variable ψ be represented by $\psi(x_i, y_j, \chi_k, \tau_l)$ with (x_i, y_j) the horizontal grids, χ_k the time sequence in months, τ_l = 1, 2, ..., the time sequence in a month. Let $\bar{\psi}(x_i, y_j, \chi_k)$ be the monthly mean of the scalar. The synoptic anomalies

$$\psi'(x_i, y_j, \chi_k, \tau_l) = \psi(x_i, y_j, \chi_k, \tau_l) - \bar{\psi}(x_i, y_j, \chi_k),\qquad(4.6)$$

are re-arranged into a $N \times P$ matrix, $\psi'(\mathbf{r}_n, t_p)$, $n = 1, 2, ..., N$; and $p = 1, 2, ..., P$. Here N is the total number of the horizontal grid points and P is the total number of time points used for computing the covariance matrix. The EOF analysis widely used in oceanographic and meteorological research (e.g., Weare et al., 1976; and see review by Richman, 1986; Chu et al., 1997 a, b) is the same as the principal component (PC) analysis (Hotelling, 1933) in the statistics community. PCs are the amplitudes, which are functions of time, of their corresponding EOFs. These EOFs can be found by calculating the unitary eigenvectors of the covariance matrix associated with the sample data field. EOF analysis separates the data sets into eigenmodes. Generally speaking, each mode has an associated variance, dimensional spatial pattern, and non-dimensional time series. The $N \times N$ spatial covariance matrix is calculated by

$$\mathbf{R} = \begin{bmatrix} R_{11} & R_{12} & \cdots & R_{1N} \\ R_{21} & R_{22} & \cdots & R_{2N} \\ \vdots & \vdots & \cdots & \vdots \\ R_{N1} & R_{N2} & \cdots & R_{NN} \end{bmatrix}, \quad R_{nm} = \frac{1}{P-1} \sum_{p=1}^{P} \psi'(r_n, t_p)\psi'(r_m, t_p),\qquad(4.7)$$

where n and m (1, 2, ..., N) denote the grid locations. The diagonal elements of the covariance matrix $\{R_{nn}\}$ are the variance at location $\mathbf{r}_n$. The off-diagonal elements are the covariance with spatial lag equal to the difference between the row and column indices. This symmetric matrix has N real eigenvalues λ_α, and eigenvectors $\phi_\alpha(\mathbf{r}_n)$, such that

$$\sum_{j=1}^{N} R_{ij}\phi_\alpha(\mathbf{r}_j) = \lambda_\alpha \phi_\alpha(\mathbf{r}_i), \quad i = 1, 2, ..., N.\qquad(4.8)$$

The eigenvectors $\phi_1(\mathbf{r}_i)$, $\phi_2(\mathbf{r}_i)$, ..., $\phi_N(\mathbf{r}_i)$ are called EOFs. Each of them is an N-point field showing anomaly pattern. The eigenvalues, λ_α ($\alpha = 1, 2, ..., N$), are all positive and the summation of them, $\sum_\alpha \lambda_\alpha$, equals the total variance. Therefore, λ_α is considered as the portion of total variance "explained" by the EOF $\phi_\alpha(\mathbf{r}_n)$. It is convenient to label the eigenfunctions $\phi_\alpha(\mathbf{r}_n)$ so that the eigenvalues are in descending

$$\lambda_1 > \lambda_2 > ... > \lambda_N. \tag{4.9}$$

The data matrix, $\psi'(\mathbf{r}_n, t_p)$, is thus approximately written by

$$\psi'(\mathbf{r}_n, t_p) = \sum_\alpha PC_\alpha(t_p)\phi_\alpha(\mathbf{r}_n), \tag{4.10}$$

where $PC_\alpha(t_p)$ is the principal component with the same unit as the scalar ψ and a size of P, representing the temporal variation of the associated spatial pattern described by EOF $\phi_\alpha(\mathbf{r}_n)$.

D. COMPLEX EOF ANALYSIS

Consider a two-component variable such as the horizontal velocity vector (u, v). A complex field can be constructed by

$$w = u + iv, \quad i = \sqrt{-1}. \tag{4.11}$$

Similar to the previous section, let a temporally and spatially varying complex field w be represented by $w(x_i, y_j, \chi_k, \tau_l)$ with (x_i, y_j) the horizontal grids, χ_k the time sequence in months, $\tau_l = 1, 2, ...,$ the time sequence in a month. Let $\bar{w}(x_i, y_j, \chi_k)$ be the monthly mean of the scalar. The synoptic anomalies

$$w'(x_i, y_j, \chi_k, \tau_l) = w(x_i, y_j, \chi_k, \tau_l) - \bar{w}(x_i, y_j, \chi_k), \tag{4.12}$$

are re-arranged into a $N \times P$ matrix, $w'(\mathbf{r}_n, t_p)$, n = 1, 2, ..., N; and p = 1, 2, ..., P. Here N is the total number of the horizontal grid points and P is the total number of time points used for computing the covariance matrix. $N \times N$ spatial covariance matrix is calculated by

$$\mathbf{R} = \begin{bmatrix} R_{11} & R_{12} & ... & R_{1N} \\ R_{21} & R_{22} & ... & R_{2N} \\ \vdots & \vdots & ... & \vdots \\ R_{N1} & R_{N2} & ... & R_{NN} \end{bmatrix}, \quad R_{nm} = \frac{1}{P-1}\sum_{p=1}^{P} w'^{*}(\mathbf{r}_n,t_p)w\psi'(\mathbf{r}_m,t_p), \qquad (4.13)$$

where the superscript "*" denotes the transpose. The diagonal elements of the covariance matrix $\{R_{nn}\}$ are the variance at location $\mathbf{r}_n$. The covariance matrix $\mathbf{R}$ is a Hermitian, so the eigenvalues $\{\lambda_\alpha\}$ are positive real numbers whereas the EOFs $\{\phi_\alpha(\mathbf{r}_n)\}$ are complex,

$$\sum_{j=1}^{N} R_{ij}\phi_\alpha(\mathbf{r}_j) = \lambda_\alpha\phi_\alpha(\mathbf{r}_i), \quad i = 1, 2, ..., N. \qquad (4.14)$$

Each of the complex EOFs $\phi_1(\mathbf{r}_i)$, $\phi_2(\mathbf{r}_i)$, ..., $\phi_N(\mathbf{r}_i)$ them is an N-point field showing anomaly velocity vector pattern. The eigenvalues, λ ($\alpha = 1, 2, ..., N$), are all positive and the summation of them, $\sum_\alpha \lambda_\alpha$, equals the total variance. Therefore, λ_α is considered as the portion of total variance "explained" by the EOF $\phi_\alpha(\mathbf{r}_n)$. It is convenient to label the eigenfunctions $\phi_\alpha(\mathbf{r}_n)$ so that the eigenvalues are in descending

$$\lambda_1 > \lambda_2 > ... > \lambda_N. \qquad (4.15)$$

The data matrix, $w'(\mathbf{r}_n, t_p)$, is thus approximately written by

$$w'(\mathbf{r}_n, t_p) = \sum_\alpha r_\alpha(t_p)\exp[i\theta_\alpha(t_p)]\phi_\alpha(\mathbf{r}_n), \qquad (4.16)$$

where $\left[r_\alpha(t_p), \theta_\alpha(t_p) \right]$ are the temporally varying amplitude (positive) and phase (between -180° and 180°) associated spatial pattern described by EOF $\phi_\alpha(\mathbf{r}_n)$.

E.   COAMPS WIND FIELDS

During analysis it was determined that bad data was present for the period of 21 to 23 June. Quality control for the data was instituted to preserve the utility of the model fields. The mean for the entire period was calculated and then substituted in for the bad data times. This did not affect the EOF and only slightly affected the mean winds. This is shown in the EOF magnitude and angle plots as a straight line.

1.   Mean Winds

A monthly and total period mean was calculated from the COAMPS wind fields. A definite change in wind direction is noticeable over even just a couple of months (see Figure 15). In February, the mean wind is west-southwesterly and continues to be so until May, when the beginnings of the Southwest Monsoon start to be seen in the eastern portion over the GOO. The change is with the noticeable reduction in mean wind speed over the southeastern portion of Iran's Hormozgan Province. The full change into the Southwest Monsoon season is evident in the monthly mean for June and July (Figure 15 "e" & "f").

Conversely, the overall mean flow, from February to July, does not give much information in the change in winds over the period (see Figure 16). The vector plot shows the tendency of synoptic flow over the region. It highlights the predominance of the Shamal over the southern portion of the Gulf and the mostly southerly flow experienced by Bandar Abbas which is nestled in the bend of the strait. Orographic effects are noticeable by the lengthening of the winds along the Hajar Mountain Range over Oman and the UAE alluding to down-slope winds, as well as steering of winds by the Zagros Mountains of Iran.
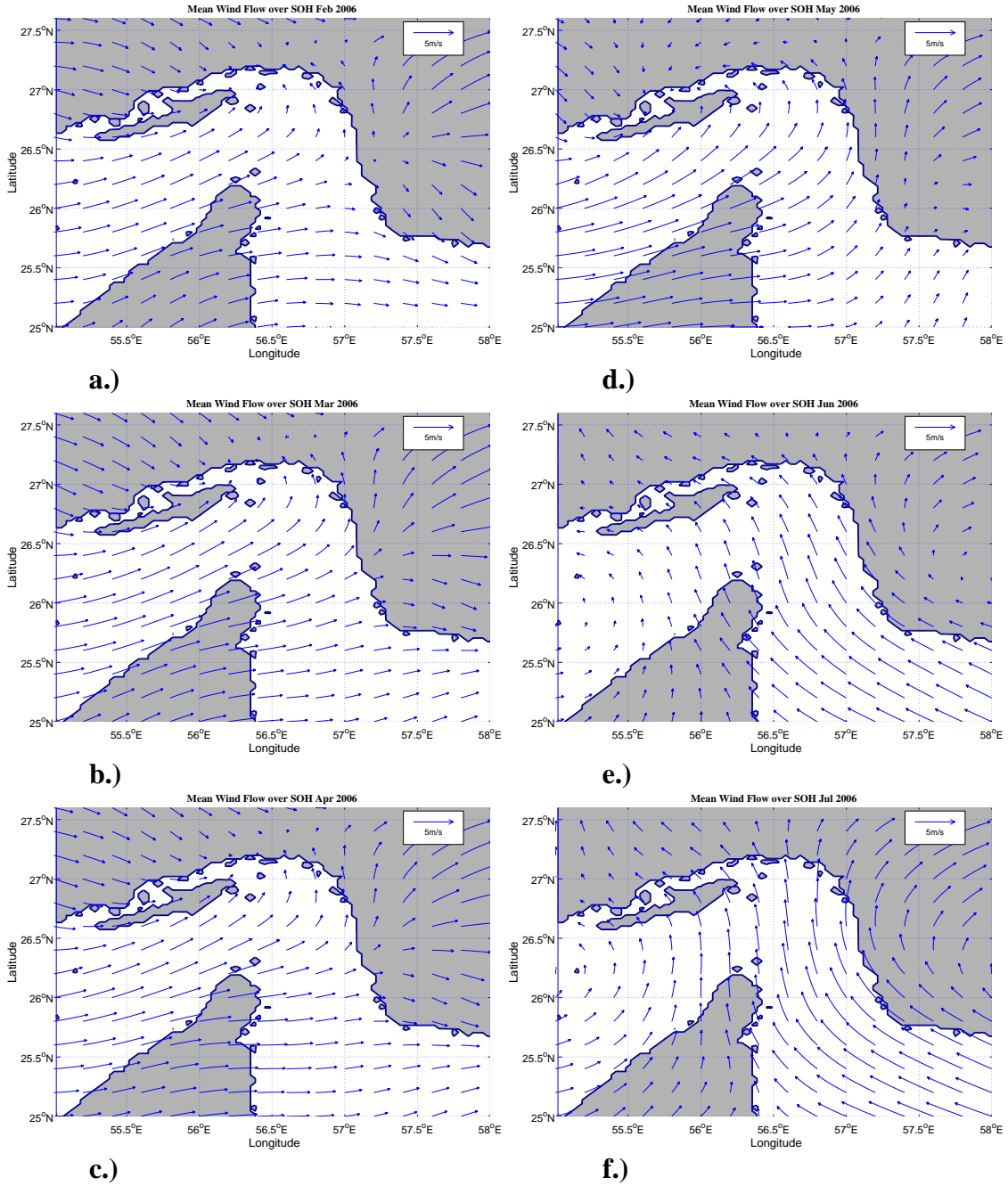
Figure 15.   Monthly Mean vector plots of COAMPS wind fields for: a) February, b) March, c) April, d) May, e) June, and f) July.
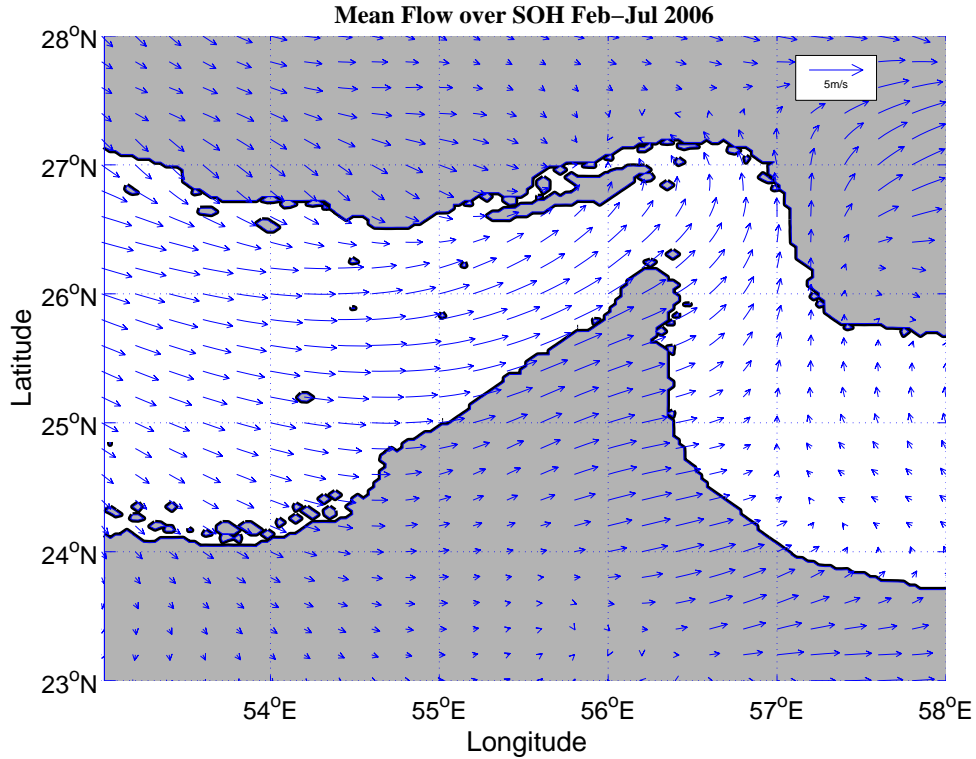
Figure 16.   COAMPS Mean Wind for the entire six month period from February to July 2006.

2.   Complex EOFs

As explained previously, one of the advantages of EOF analysis is that a small set of information may be used to describe large processes. For example, in Table 3, the first three modes correspond to almost 83% of the total variance. Hence, the first three modes were determined to be sufficient to describe the processes involved in forcing for the winds in the region.

Table 3 shows that the EOF modes are for the SOH and not for the entire Persian Gulf region described earlier. As explained in the Background Chapter, the processes involved in the SOH are a combination of both extra-tropical and monsoonal synoptic forcing as well as LSBC events. This portion of the Gulf region is significantly different from the rest of the Gulf and therefore, would be disproportionately represented if the entire wind field for the Gulf were analyzed. The extra-tropical synoptic features would have more grid points represented and would therefore, skew the EOF, causing a smoothing of the features that were desired for analysis.

42

EOF	Percentage of Variance	Percentage of Cumulative Variance
1	52.69%	52.69%
2	22.05%	74.74%
3	7.94%	82.68%
4	5.03%	87.71%
5	3.16%	90.87%
6	2.24%	93.11%
7	1.73%	94.84%
8	1.11%	95.95%
9	0.68%	96.63%
10	0.63%	97.26%

Table 3.   COAMPS EOF eigenmodes and corresponding percentage of variance for the winds over the Strait of Hormuz from Feb to Jul 2006.

Hence, the area box was reduced, to the dimensions: 25N, 55E to 27.6N, 58E, in order to better represent the forcing affecting the winds over the SOH (comparing Figures 16 and 17). The EOF modes were plotted and analyzed and it was found that large anomalies were longer lasting in the late winter and early spring months, becoming more on a diurnal to semidiurnal time scale in late spring and into the summer months (Figure 18). This is a good indication that the LSBC increases in affect and frequency in the summer to winter months as noted by Zhu and Atkinson (2004) as well as Eager et al. (2005). Additionally, a Power Spectrum of each EOF Mode was plotted, revealing a diurnal constituent in all top three modes (Figure 24). Since the sampling for COAMPS was every six hours this means the Nyquist frequency cutoff is at about the 12 hour mark. This means all influences about equal to or less than 12 hours will not be able to be captured in the power spectrum. The diurnal constituent was strong in the first mode, heaviest in the second mode and not insignificant in the third mode. This would lead one to conclude that Zhu and Atkinson (2004) were correct in their assessment that the low-level wind field over the Gulf was "dominated by a single, coherent circulation termed as the LSBC."
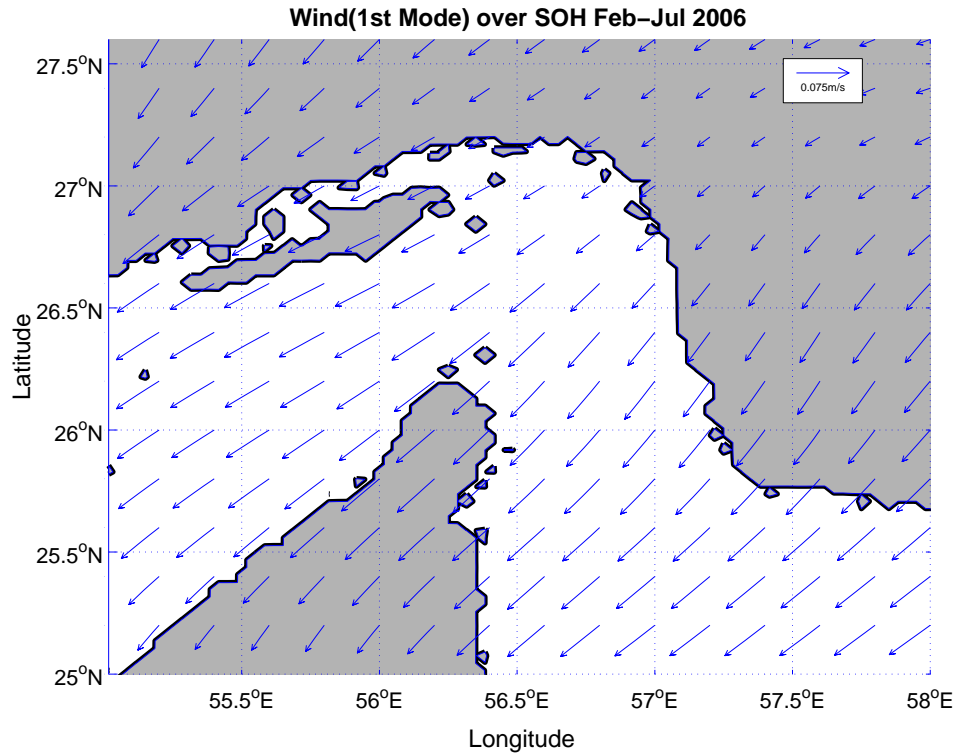
Figure 17.   EOF-1 Vector plot. The reference arrow is 0.075m/s.

Figure 18.   First Mode Time Series of EOF Coefficient magnitude and angle in six hour increments over the entire period of six months.

44

Synoptic forcing is the larger force that is being acted on by the smaller perturbations of the LSBC events in this case. The synoptic wind patterns shown in Figure 19 should be kept in mind when observing the results of the EOF mode vector plots starting with Figure 17. The vectors represented in Figure 17 are in opposition to the synoptic flow shown in Figure 19. Perturbation vectors are just an indication of the axis of movement since direction is dependent on phase angle. Moreover, the magnitude indicated in the time series of the amplitude are unit-less and must be multiplied by the scale represented in the EOF modes. Since in the case of the winds the scale is 0.075 m/s a magnitude of 150 , as shown in EOF-1 around 23 March, is a perturbation equal to 11.25 m/s. This, combined with the vector plots yields the following information: EOF-1 is largely affected by LSBC but mostly influenced by synoptic forcing, EOF-2 is primarily LSBC influenced, and EOF-3 is slightly influenced by LSBC but appears to be more of an indication of terrain effects on flow. Mode 1 follows the mean wind vector pattern and is likely due to changes in the synoptic flow. EOF-2, where the LSBC influence is largest, shows an eddy in the center of the strait just to the north of the Musandam Peninsula. This eddy of perturbations is due to the influence of LSBC events from the land masses surrounding the area. EOF-3 shows vector axes along mountain ranges and indicate downslope tendencies as well.

a)   b)
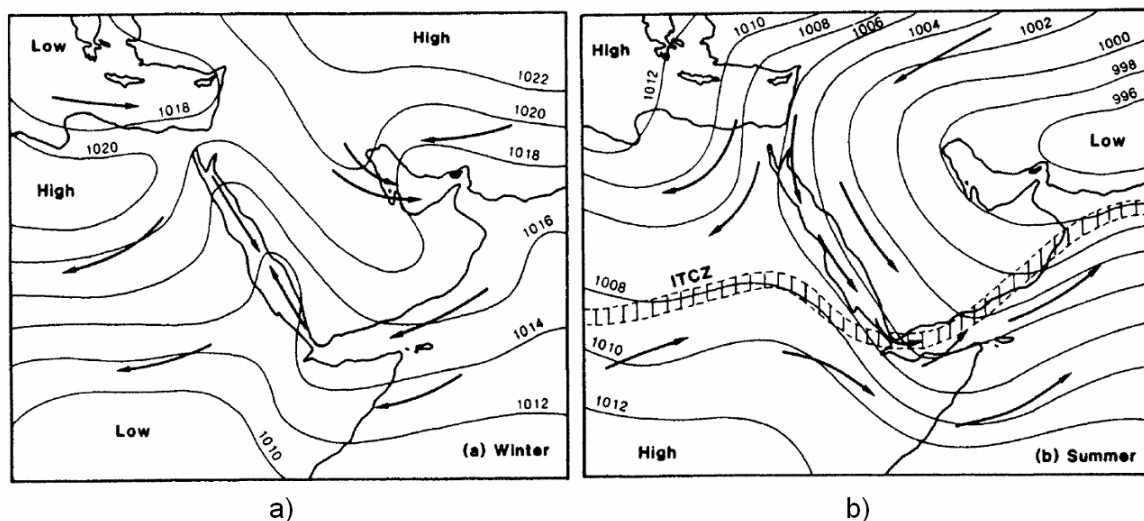
Figure 19.   (a) Winter and (b) summer wind patterns over the Arabian Peninsula (From: Sheppard and Dixon, 1998).
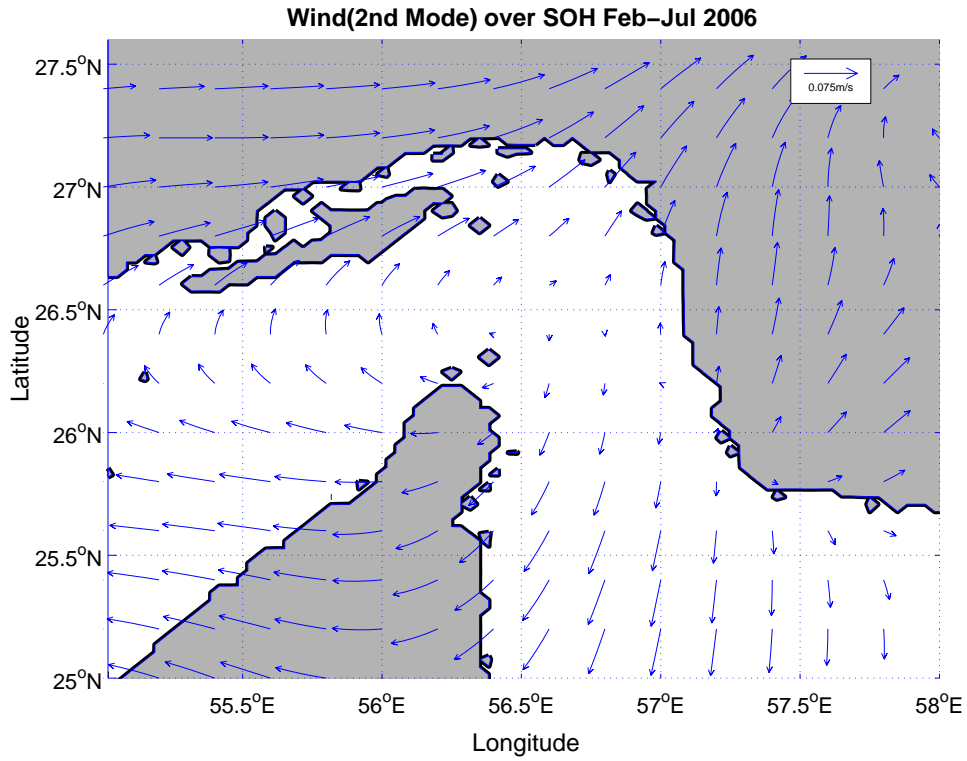
Figure 20.   EOF Second Mode Vector plot. The reference arrow is 0.075 m/s.
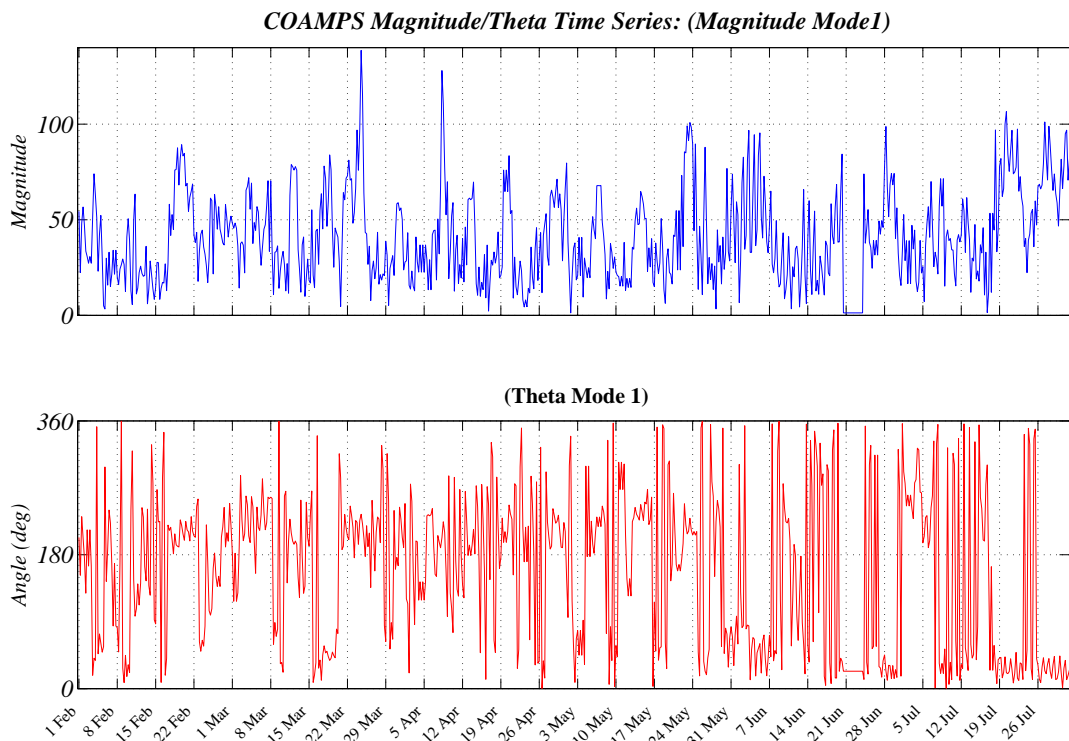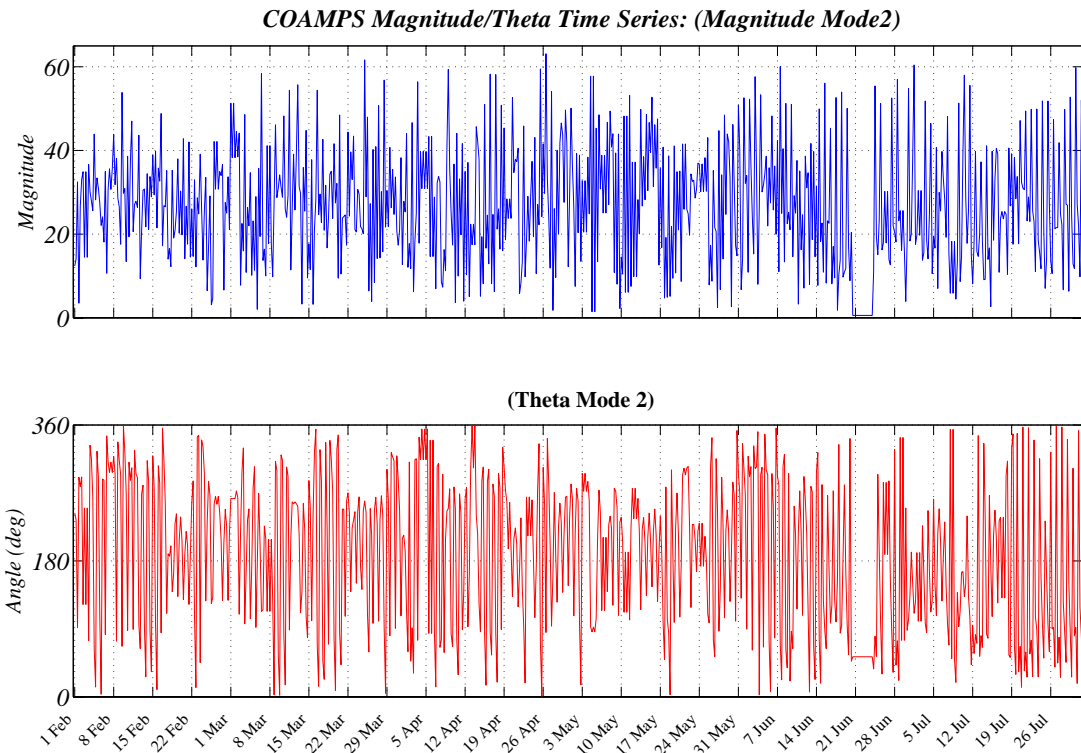

Figure 21.   EOF Second Mode Time Series of EOF Coefficient magnitude and angle in six hour increments over the entire period of six months.
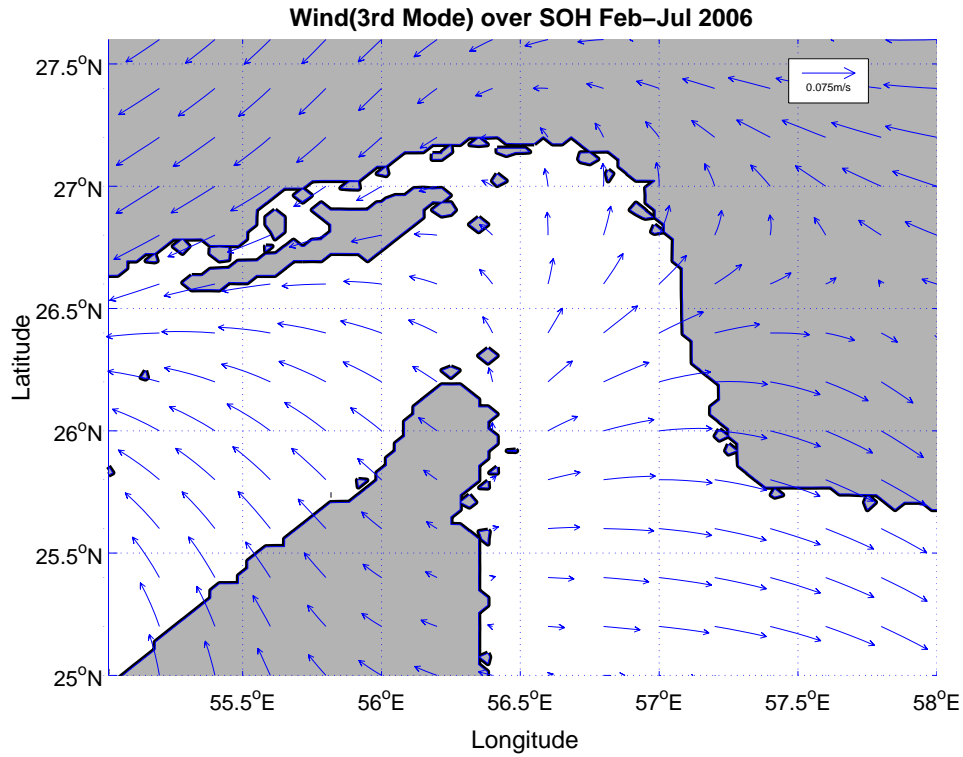
Figure 22.   EOF Third Mode vector plot. Reference arrow is 0.075 m/s.
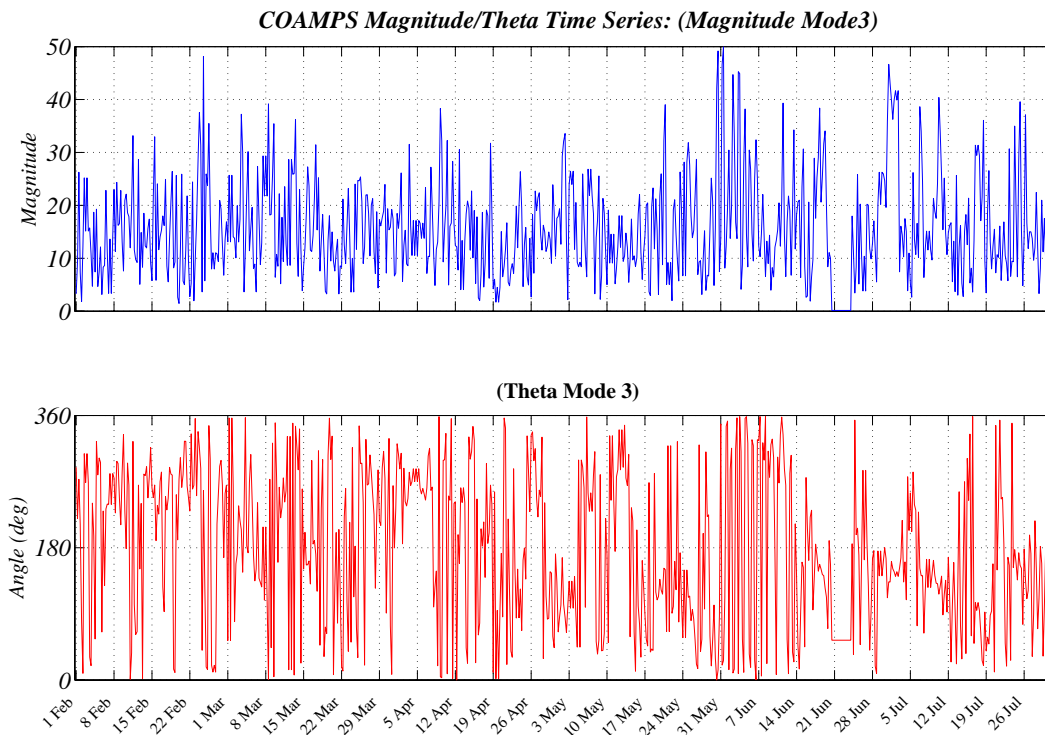
Figure 23.   EOF Second Mode Time Series of EOF Coefficient magnitude and angle in six hour increments over the entire period of six months.

SOH COAMPS EOF Power Spectrum (Mode 1)

Period(day)

(Mode 2)

Period(day)

(Mode 3)

Period(day)
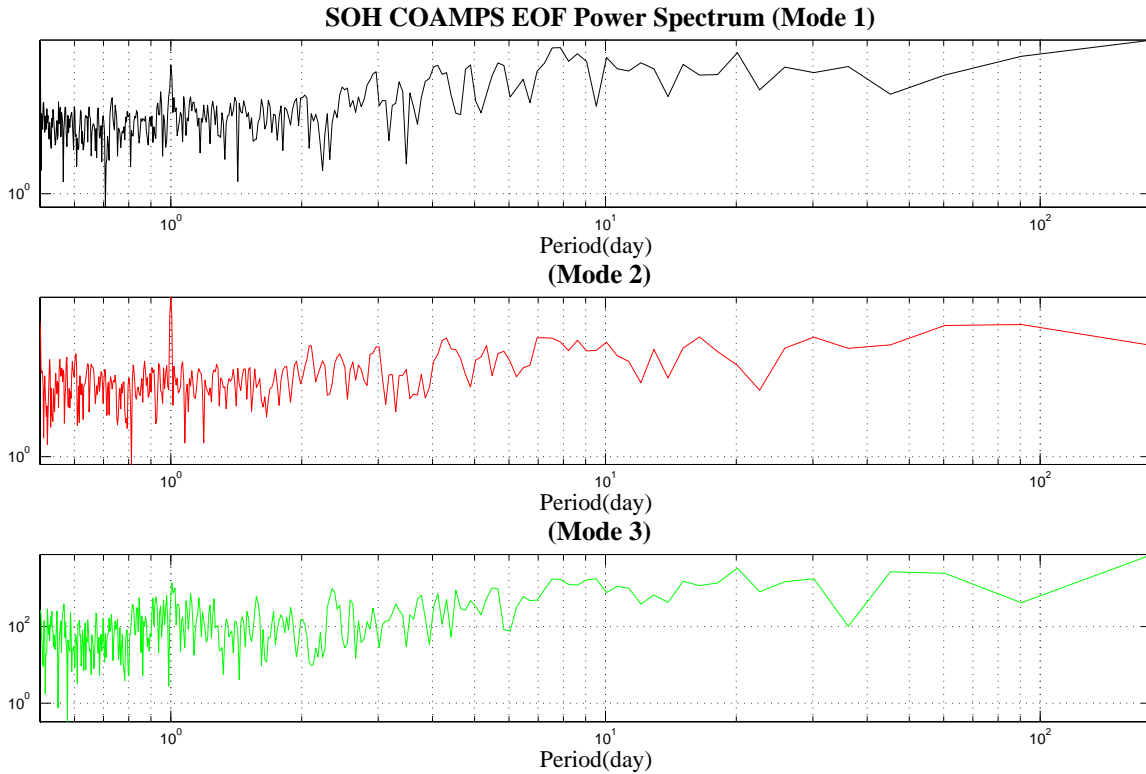
Figure 24.　　　Power Spectrum plot of EOF Coefficient Modes 1-3. The first spike in all three modes is at the one day mark indicating a diurnally cycling constituent.

3.　　Modeled Wind Features

In addition to EOF analysis, wind fields were plotted in vector format for viewing and analysis. Initially the wind fields were made into images and then viewed to give an initial assessment of the wind flow over the area. The SOH is four hours ahead of UTC and since the wind fields were in six hour increments it was not easy to identify small delays in onset for mesoscale features. The wind often varied, with synoptic patterns dominating the daily patterns. Definite land/sea breeze cycles (LSBC) were evident where the synoptic forcing was weak, similar to the findings of Zhu and Atkinson (2004).

In order to investigate the occurrence of LSBC it was decided to break the video into pieces. Furthermore, the winds were broken out according to hour so that all winds at the same hours were grouped together for analysis. This yielded a good assessment of not only LSBC events but also time periods of pure synoptic forcing. During periods of low winds in the Gulf, alongshore winds were evident at the coastline of the UAE at the 06 UTC (1000 Local) times. LSBC events were most noticeable at the 12 and 00 UTC (1600 and 2200 Local). These were identifiable events where the flow was to or from the

land on both sides of the SOH. Some events were also identified where the forcing was less on the leeward side of the Hajar Mountains which is a possible cause for the Omani coast to experience LSBCs. In this case there was less evidence of LSBC events elsewhere making it a localized feature based on terrain.

It was rare for wind speed to exceed 10 m/s over the area of interest; however, there were strong shamal wind events in February and March that definitely exceeded that speed. Evidence of large scale circulation was evident from the similarity of flow regardless of terrain. Also, large wind velocity was a key for the synoptic influence. Onshore flow dying not far from the coast evidenced interaction between synoptic and LSBC mesoscale features.

F.   CURRENTS

The SWAFS model fields were missing the 23 June data due to complications. Also, during analysis it was determined that bad data was present for 23 May. The same process of quality control used for the data in SWAFS was used in the COAMPS case.

1.   Mean Current

The monthly mean vector plots (Figure 26) appear to show a turbulent flow through the SOH. The six month mean vector plot shows current flowing in both directions as well (Figure 25). Keeping in mind that the flow through the strait is primarily tidally driven, one would think that the mean should be no flow. Indeed the mean flow is actually very small in magnitude. Notice the reference arrow is 20 cm/s and most of the flows are less than the reference.

The mean flow actually shows preferred paths of flow. As water flows into the SOH the path is not the same in nature as that of water flowing out. The Coriolis apparent force acting upon surface water pushes it to the right in the northern hemisphere and predictably the flow through the strait is fashioned so that the majority of surface flow is along the coasts to the right of the direction of flow.

Complications to this simple flow arise with the bend in the strait. The abrupt loss of coastline bending away on the outflow gives rise to the aforementioned peninsular cyclonic eddy. The eddy is present in varying degrees of strength and

slight modification in location throughout the six months of data.   Thus, the topography is the main engine for this feature.

Another complication to simple flow is the eddy which forms at the mouth of the strait and the edge of the GOO. This eddy is a strong agent in the effective surface transport out of and into the SOH. It appears to limit surface outflow and actually add velocity to IOSW inflow. Recall that the southwest monsoon started to be seen in the monthly mean wind plot in May. Indications from March's mean current plot shows the eddy from the GOO just starting to push in and adding turbulent energy to the flow on the east side of the strait. Moving through the plots to July, one can see the effect the eddy continues to have as it grows closer to the mouth of the strait. The closer the eddy gets to the strait the further the peninsular eddy moves to the west and also more of the eastern leg eddies are generated.

Wind did not appear to be a major forcing agent for the currents through the strait, although it was used in oil spill scenario development for study of how the dispersion of oil reacts to differing combinations of wind and current.
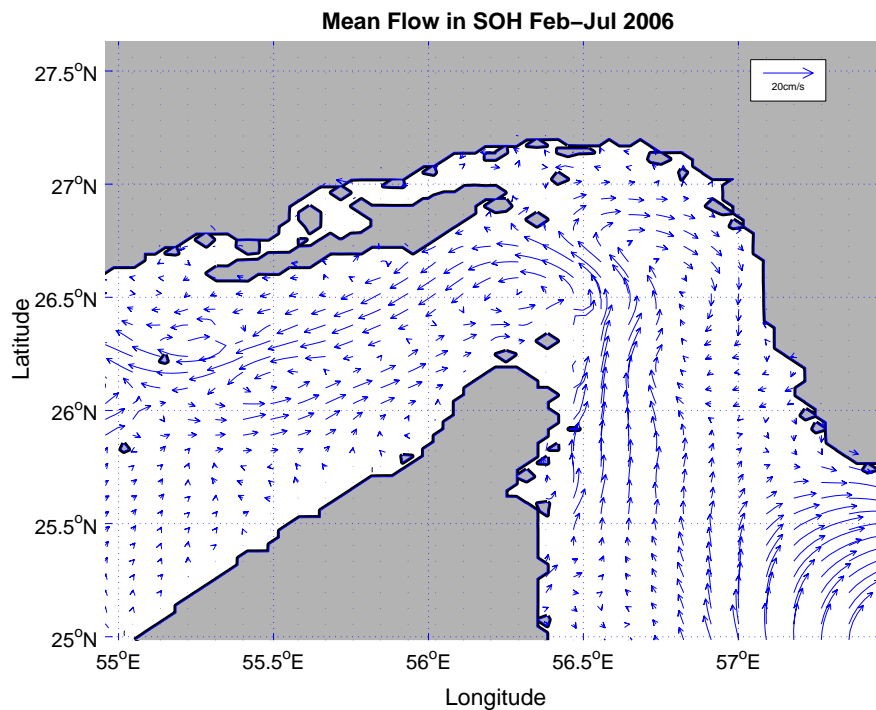

Figure 25.   SWAFS Mean Current for the entire six month period from February to July 2006. Reference arrow is 20 cm/s.
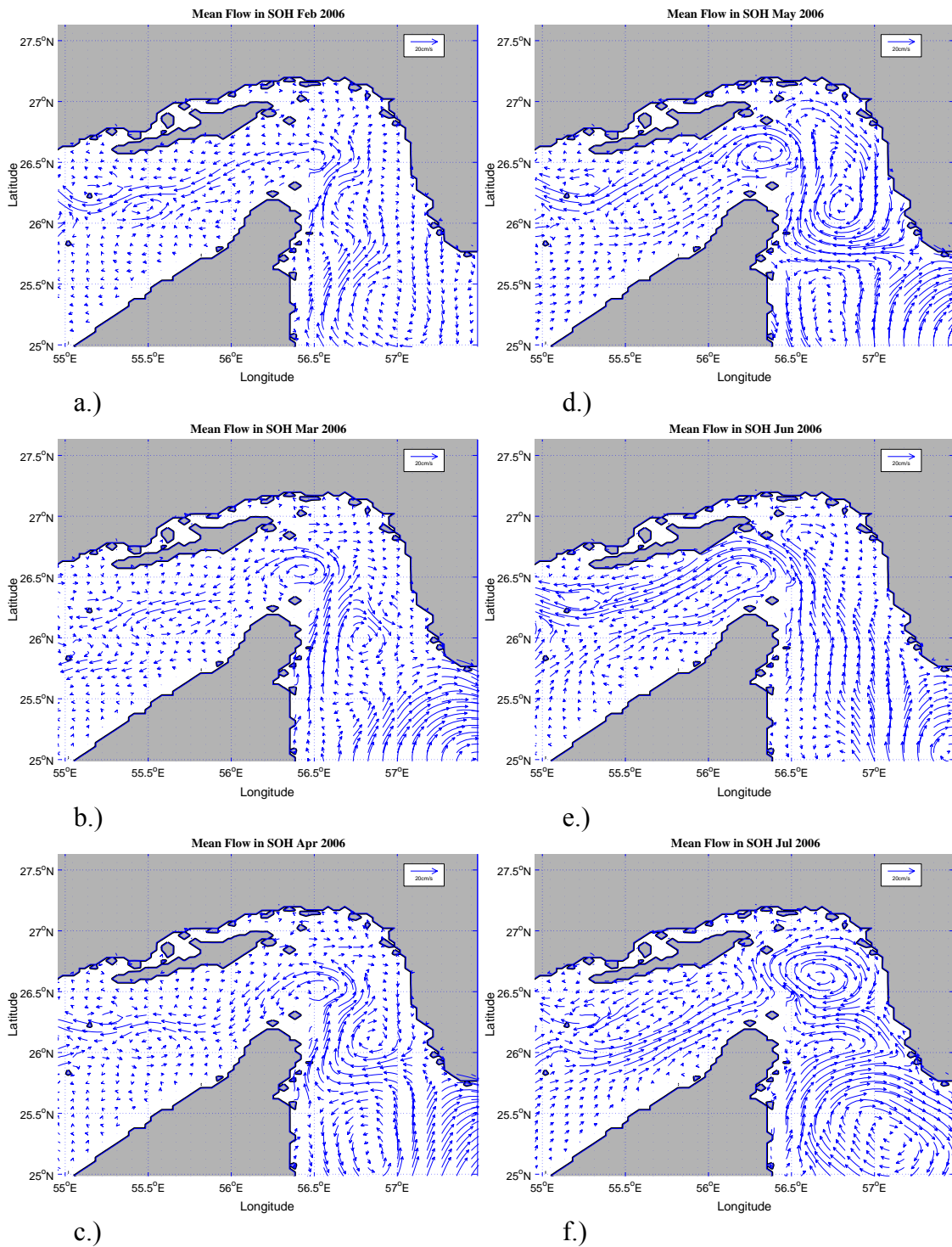
Figure 26.   Monthly Mean vector plots of SWAFS current fields for: a) February, b) March, c) April, d) May, e) June, and f) July. Reference arrow is 20 cm/s.

2.   Complex EOF Analysis

The SWAFS model fields of 0.5 m currents were analyzed using the previously explained EOF analysis. After analysis, it was determined that it was necessary to consider at least the first four modes for the SWAFS current fields (see Table 4).

EOF	Percentage of Variance	Cumulative Percentage of Variance
1	36.11%	36.11%
2	18.08%	54.19%
3	10.56%	64.75%
4	6.70%	71.45%
5	4.69%	76.14%
6	2.84%	78.98%
7	2.10%	81.07%
8	1.58%	82.65%
9	1.41%	84.06%
10	1.25%	85.31%

Table 4.   SWAFS EOF eigenmodes and corresponding percentage of variance for the currents in the Strait of Hormuz from Feb to Jul 2006.

EOF-1 is referred to the tidally-driven currents since it is very similar to the tidal constituent plot for S2 (comparing Figure 24 to Figure 6b). The power spectrum of its amplitude shows diurnal, semidiurnal, and spring/neap tidal cycles (Figure 35) with the main constituents for EOF-1 are the diurnal and spring/neap. Indeed, after analyzing the power spectrum of current magnitudes for four different sites in the SOH, the presence of a diurnal, semidiurnal, and spring-neap cycle tides were all present (Figure 36). Since the samples were taken at three hour intervals the Nyquist frequency cutoff is about the 6 hour mark. The presence of a constituent at the eight hour mark can not therefore be given credence as a valid constituent since it is so close to the cutoff.

EOF-2 had the same tidal constituents as EOF-1; however, the main constituent was spring/neap. The diurnal and semidiurnal constituents, although present, were much smaller than the spring/neap. The semidiurnal was an order of magnitude less. Looking at the vector plots, EOF-2 and EOF-1 were primarily affected the inside of the channel of

the strait with EOF-1 on the western leg and EOF-2 on the eastern (Figures 27, 29, and 35). Also, the differences between EOF-1 and EOF-2 include a one week lag between the spring/neap cycles (Figures 28 and 30).

Looking at the angle plot for EOF-1 (Figure 28) and EOF-2 (Figure 30), it is apparent that the angle swing is due to tides. EOF-1 oscillates from 0 to 180. The large transitions are just an effect of the plot since if the swing goes from 180 degrees to a little past zero to around 355, say, it looks like a wild swing in a short amount of time when in actuality it is a smooth swing of the angle. EOF-2 offers a more straightforward representation with a primarily smooth swing from approximately 135 to 335 degrees.

EOF-3 and EOF-4 had only semidiurnal effects and were associated with the eddy motions at the edge of the GOO and some eddy effects in the eastern leg of the strait (see Figures 31, 33, and 35). The magnitude of the semidiurnal constituent is much lower (an order or two of magnitude less) than that of the first two modes. Looking at the angle plots for EOF-3 (Figure 32) and EOF-4 (Figure 34) it is apparent that the steady tidal swings associated with the first two modes are not present. Although a tidal swing is present, the majority of movement is due to eddies. Looking at the magnitude for figures 32 and 34 and the monthly mean plots for March through May and July (Figure 26) the onset of the eddy from the GOO correlates to the swing in angle as well as magnitude for both modes. This leads to the conclusion that the last two modes are primarily representing the influence from the eddy in the GOO with these two modes accounting for the main and residual effects of the eddy influence.

Current(1st Mode) in SOH Feb–Jul 2006
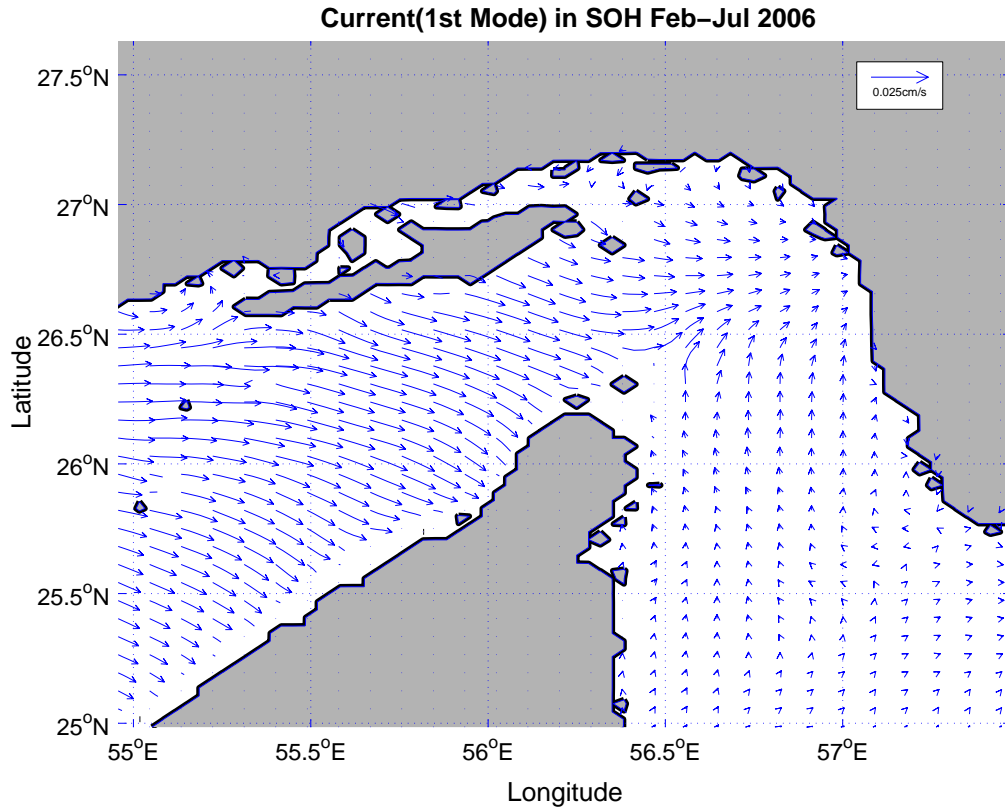
Figure 27.　　SWAFS EOF First Mode vector plot. Reference arrow is 0.025 cm/s.

SWAFS Magnitude/Theta Time Series: (Magnitude Mode1)

(Theta Mode 1)
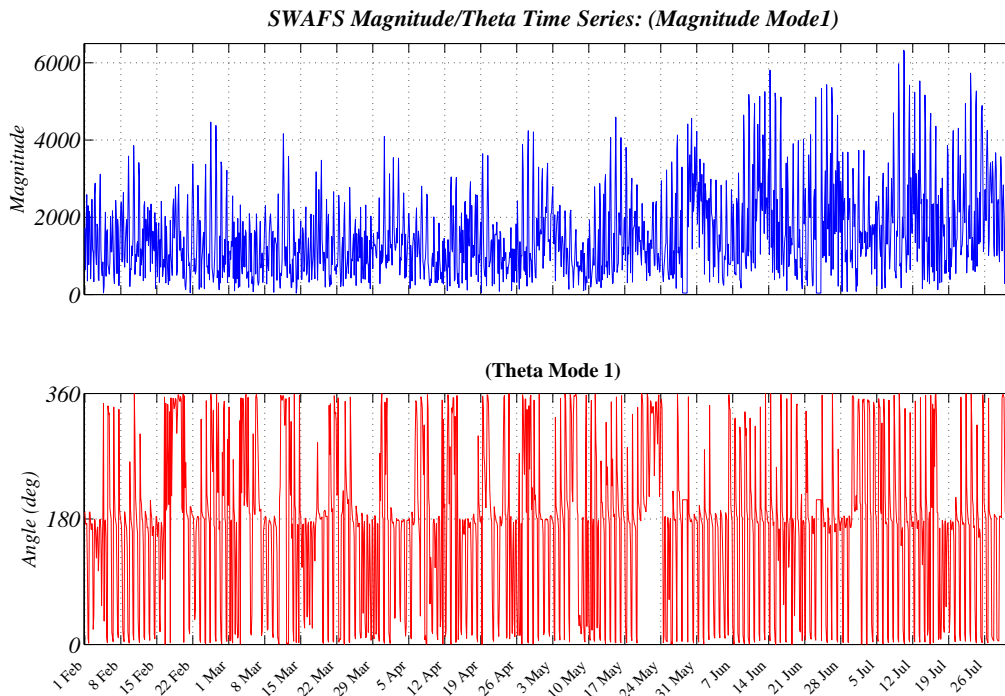
Figure 28.　　SWAFS First Mode EOF Coefficient Time Series for magnitude and direction.
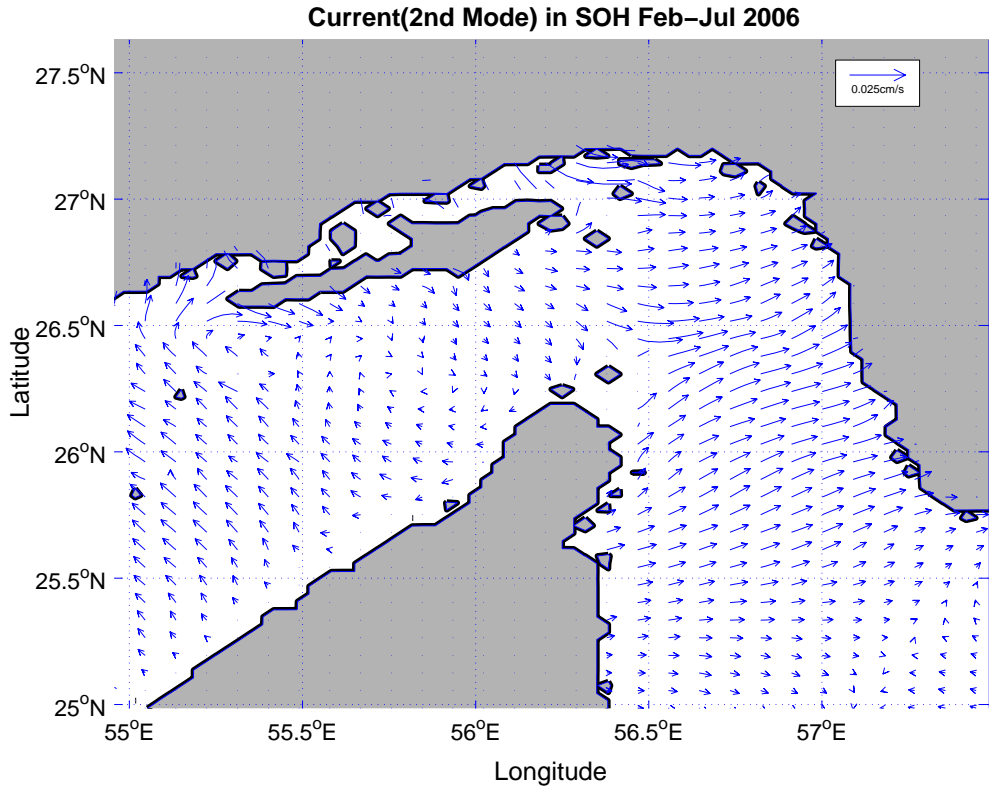
Figure 29.　　　　　SWAFS EOF Second Mode vector plot. Reference arrow is 0.025 cm/s.
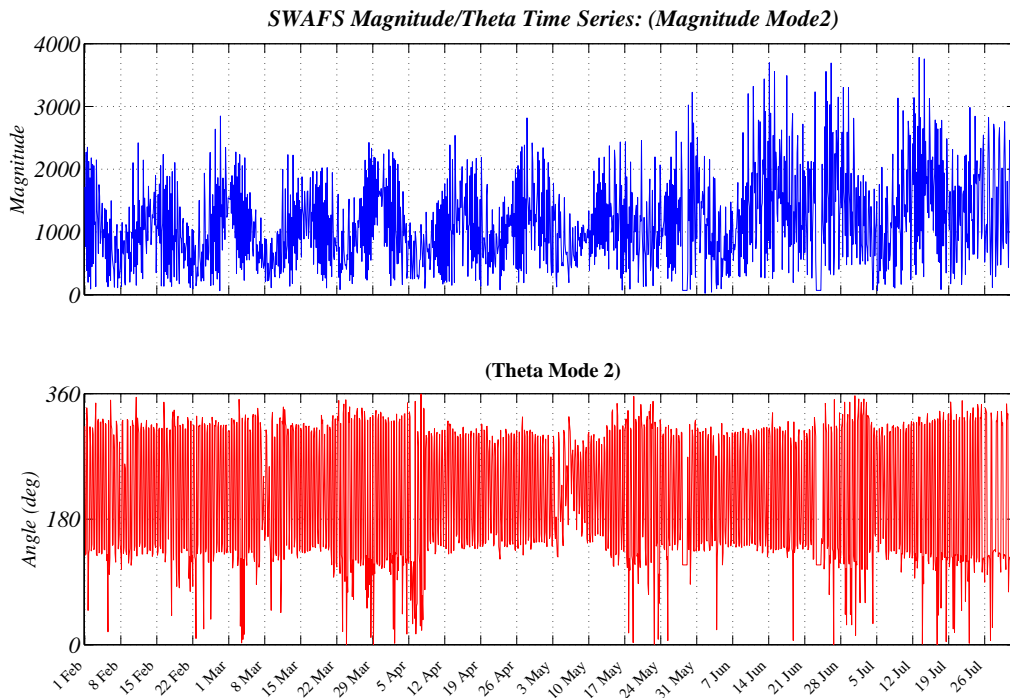
Figure 30.　　　　　SWAFS Second Mode EOF Coefficient Time Series for magnitude and direction.
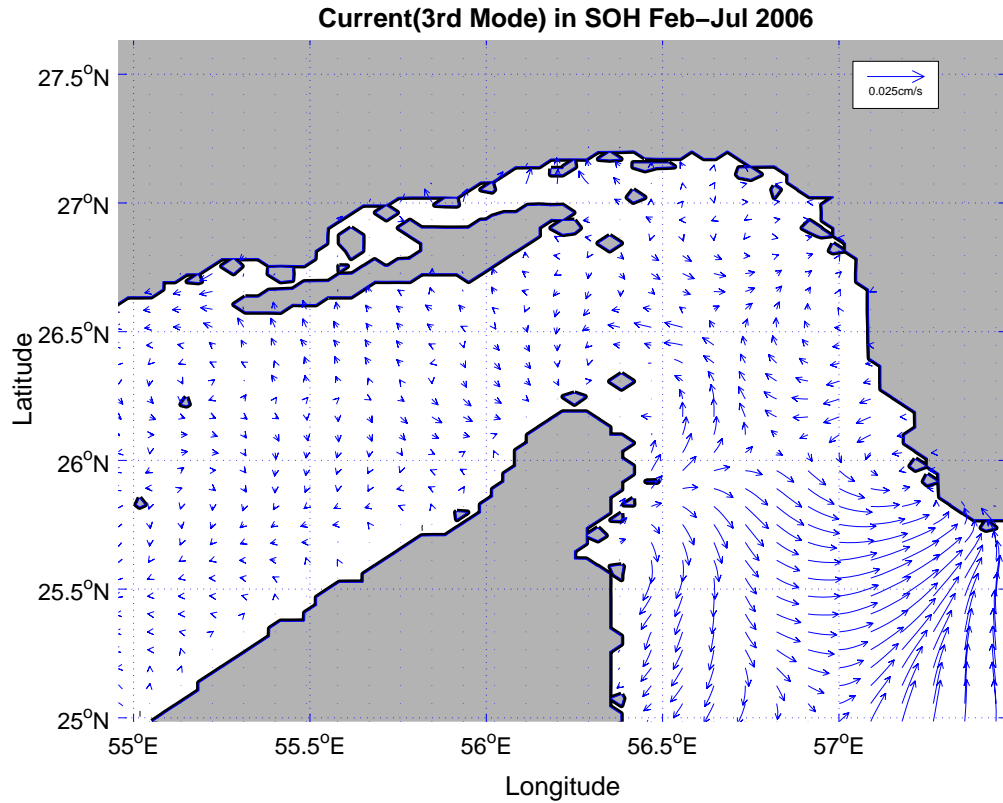
Figure 31.   SWAFS EOF Third Mode vector plot. Reference arrow is 0.025 cm/s.
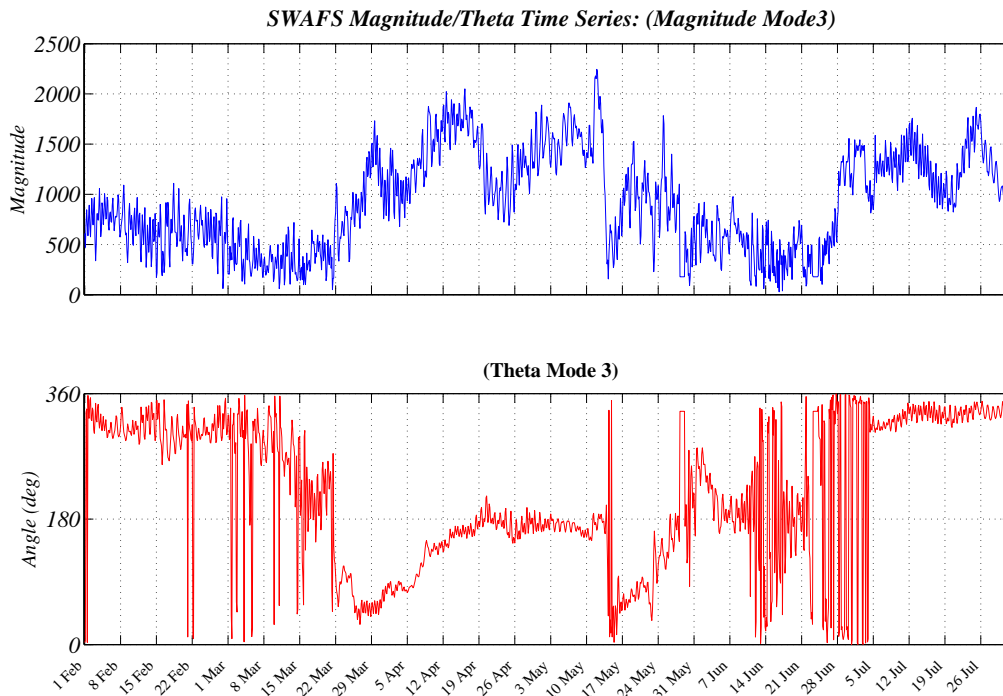
Figure 32.   SWAFS Third Mode EOF Coefficient Time Series for magnitude and
direction.

Current(4th Mode) in SOH Feb–Jul 2006
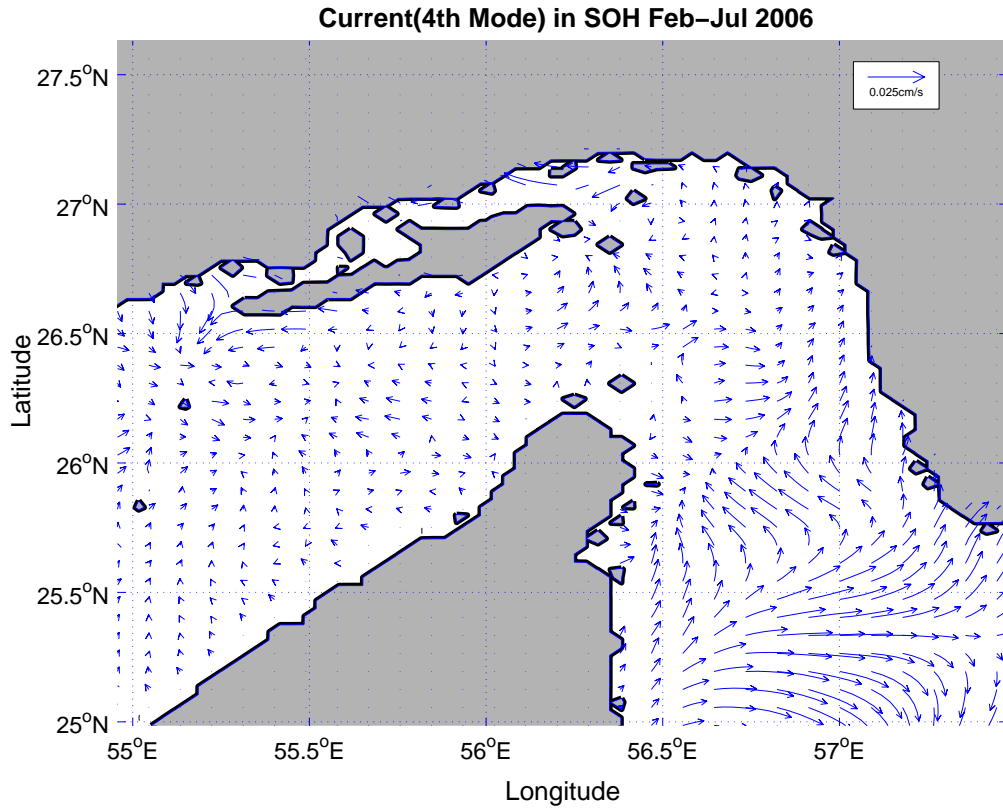
Figure 33.   SWAFS EOF Fourth Mode vector plot. Reference arrow is 0.025 cm/s.

SWAFS Magnitude/Theta Time Series: (Magnitude Mode4)

(Theta Mode 4)
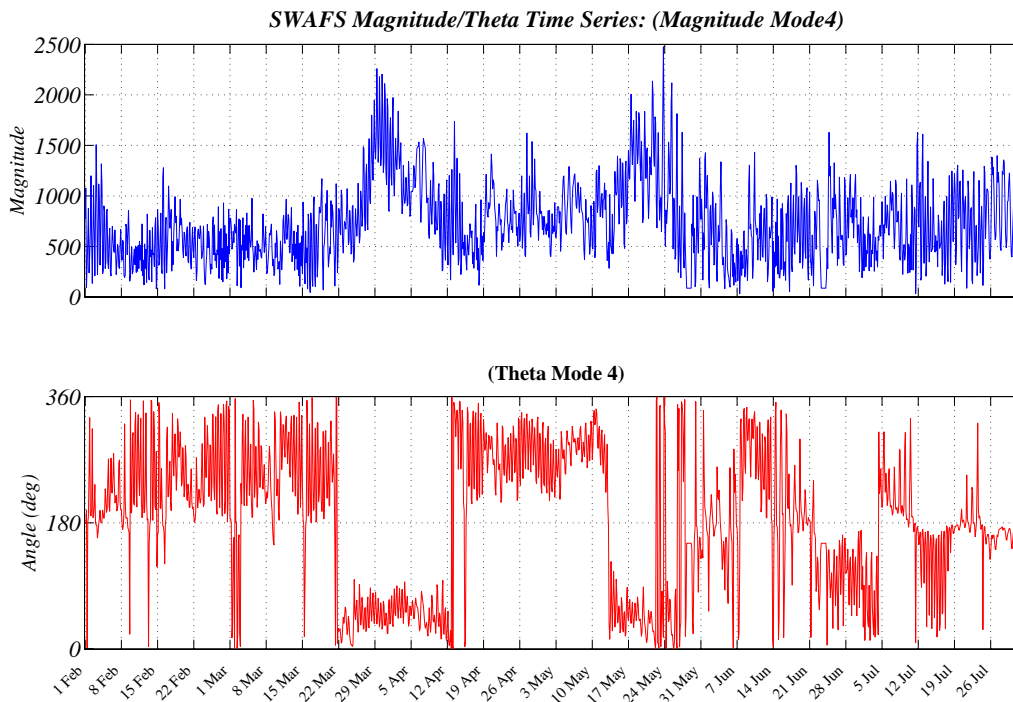
Figure 34.   SWAFS Fourth Mode EOF Coefficient Time Series for magnitude and direction.

SOH Power Spectrum of Current (1st Mode)

(Mode 2)

(Mode 3)

(Mode 4)
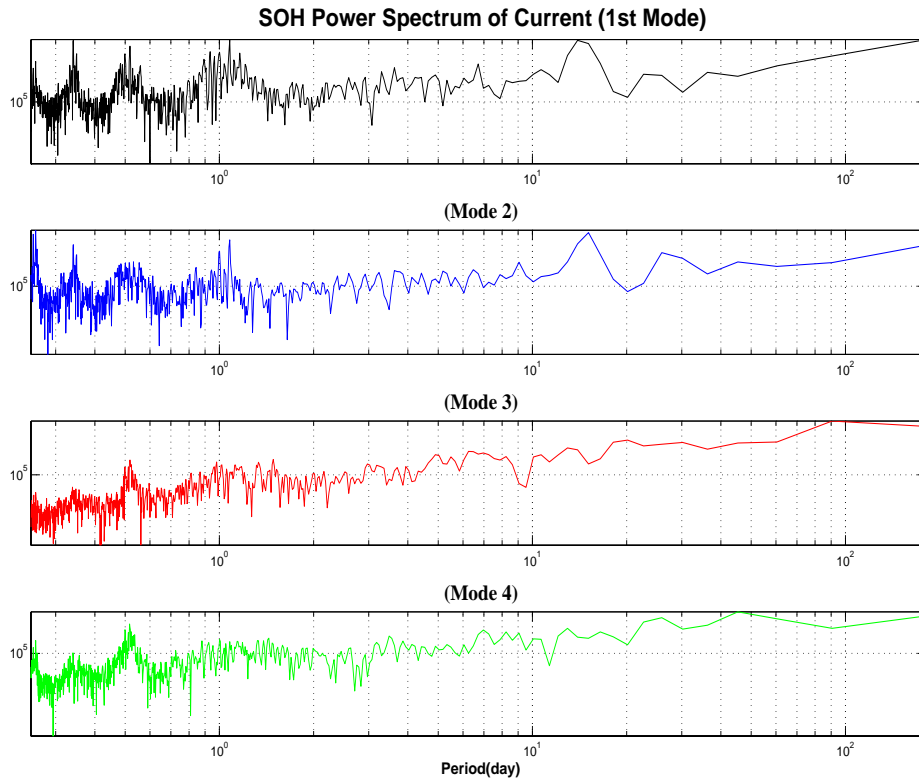
Figure 35.   Power Spectrum of SWAFS EOF Modes 1-4.

SOH Power Spectrum of Current Sites 1–4
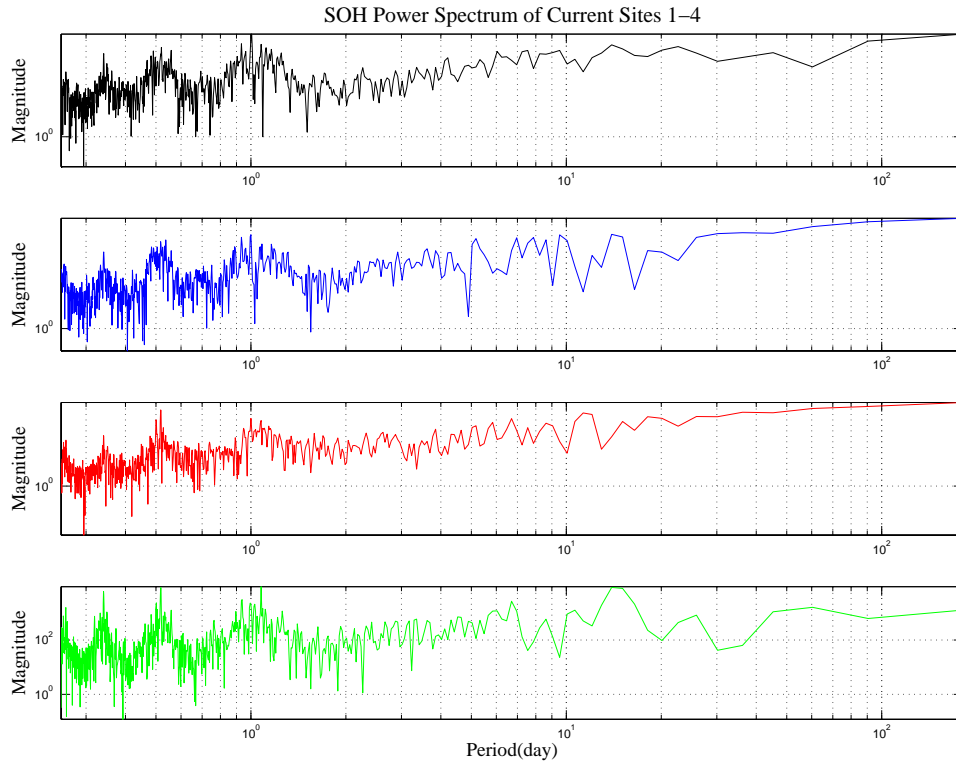
Figure 36.   Power Spectrum of current fields at four sites in the SOH

58

3.   Modeled Current Features

The fields were analyzed and found to be tidally driven with three main flow regimes and a few sub-regimes (Figures 24, 25, and 26). The first regime is best described as an Outflow Regime with the surface current flowing out of the Gulf and into the GOO. The second main regime is the Inflow Regime with surface current flowing westward into the Gulf. The last regime, the Convergent Regime, is the rarest in the collection of SWAFS currents over the six month period; in which surface current flows from the Gulf and from the GOO, converging around the Musandam Peninsula and Bandar Abbas. There are variations of flow strength associated with these main regimes from strong to almost no flow.

It was noted that the distance the surface outflow made it past the tip of the peninsula was in proportion to the influence of the eddy formed on the northwestern edge of the GOO. The stronger the eddy, the more contained the surface outflow.

Smaller eddies formed in the eastern bend of the strait especially during the transition periods from inflow to outflow and from outflow to inflow. This is also the time period where the convergent flow regimes were observed.

A particular feature was an eddy that formed at the tip of the peninsula and rotated in a cyclonic fashion. This "peninsular eddy" was a near constant feature that disappeared during periods of heavy currents and was often displaced to the north towards Bandar Abbas, Iran as well as to the west towards the island of Queshm. However, eddies forming in the eastern leg of the strait rotated in an anticyclonic direction and were a transient feature that grew in frequency and population towards the early summer as the force of the flow from the eddy in the GOO became more evident.

Vector of current(cm/s) in SOH 2006, 26 Feb, 12 UTC, 16 LST
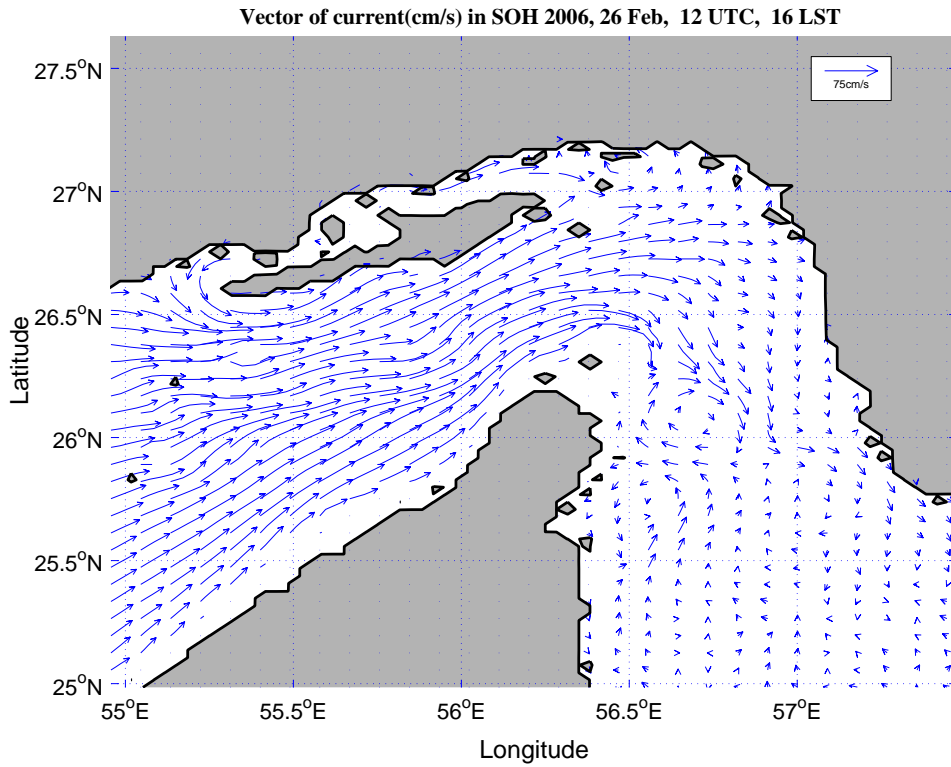
Figure 37.   Example of Outflow type current regime.

Vector of current(cm/s) in SOH 2006, 4 Apr, 0 UTC, 4 LST
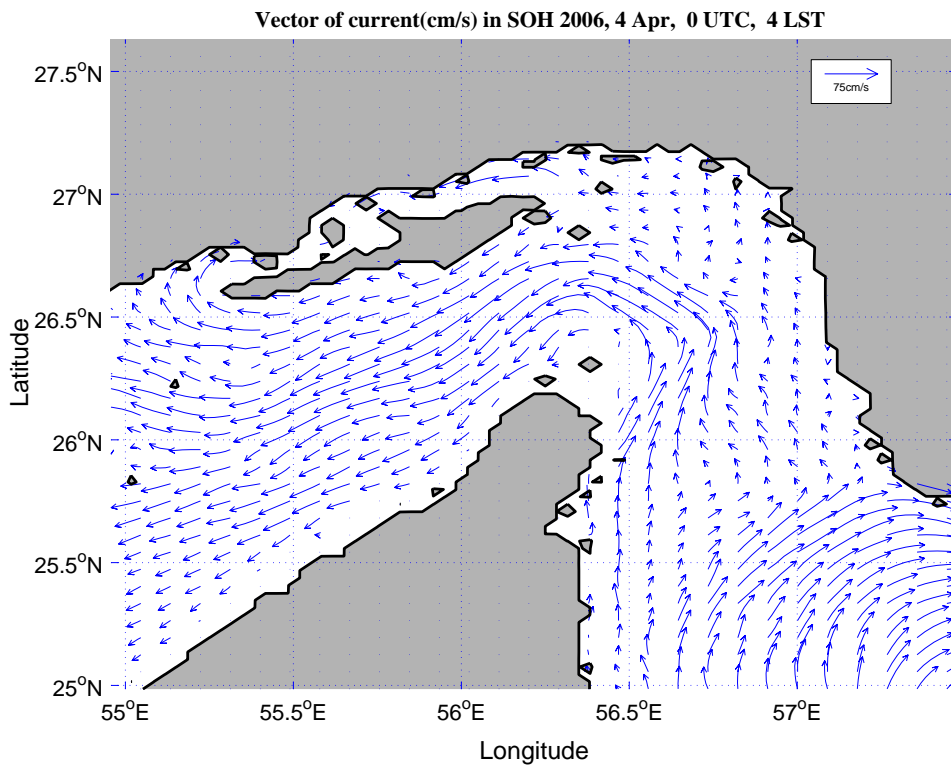
Figure 38.   Example of Inflow type current regime.

Vector of current(cm/s) in SOH 2006, 2 Mar, 6 UTC, 10 LST
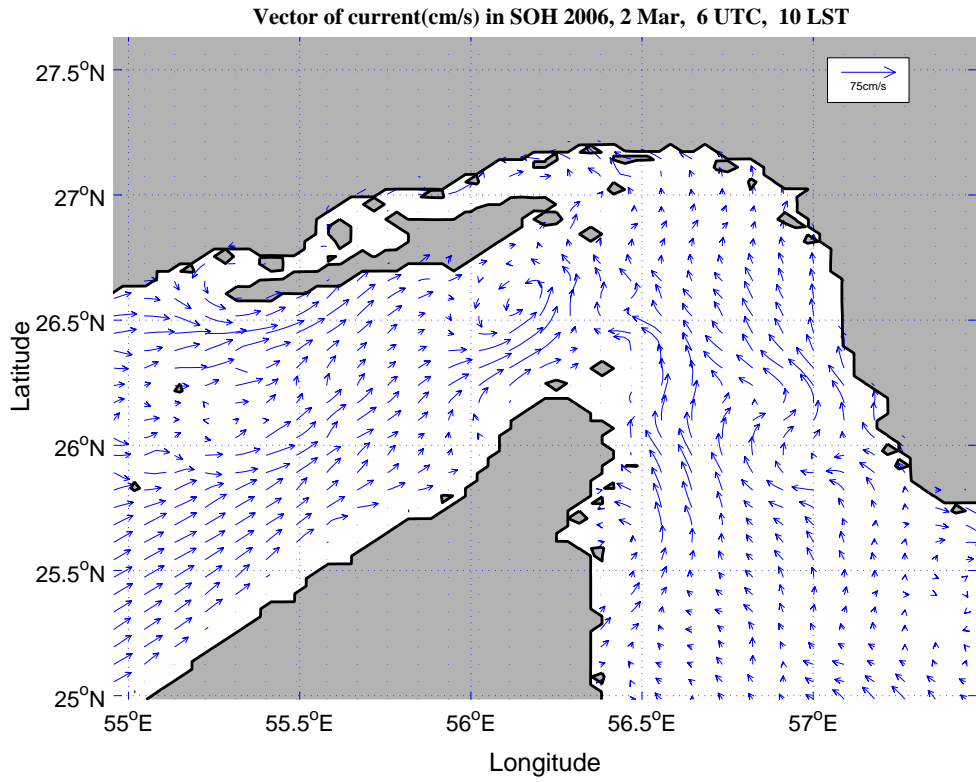
Figure 39.   Example of Convergent type current regime.

THIS PAGE INTENTIONALLY LEFT BLANK

V. SCENARIO SELECTION PROCEDURE

A. SCENARIO OBJECTIVES/SITE SELECTION

A major purpose of this thesis is to analyze the effectiveness of utilizing operational model fields as input to oil fate/dispersion and mine drift models compared to running the same models with climatology input. In order to evaluate the effectiveness of using model fields vice climatology, several different combinations of wind and current were established for analysis. Additionally, different locations representative of possible spill sites were set based on shipping lanes and possible strike areas.

1. Oil Spill/Mine Drift Scenario Premise

The premise for the spill is simple. Either a terrorist from any number of organizations currently in play, or a state actor (such as Iran) targets oil shipping through the Strait of Hormuz. Initially the scenario is that an improvised explosive device is attached to a tanker and set off once the outbound tanker reaches a predetermined point in transit. The purpose is to hamper the movement of shipping, civilian and military, through the SOH. Since the SOH is a natural choke point for shipping this is not an unreasonable scenario.

The second phase is that the spill could be a result of mining in the SOH. In this scenario a fast boat, under cover of darkness has offloaded several floating mines across an arc near the shipping lanes to disrupt shipping. This phase is analyzed using the Lagrangian drift model to see how well drift mines could be dispersed, over a maximum of 48 hours, in a high energy flow area such as the SOH. The time period of 48 hours is due to the present capacity for the prediction of currents with SWAFS. This allows for the direct comparison of model fields to mean flow.

Either of these scenarios would be a cause for the U.S. Navy to be concerned. Indeed, the loss of shipping in the SOH for even a short amount of time translates to a world economic crisis.

2. Location Selection

There was a spill site location located on both the eastern and western legs of the SOH in or near the transit lanes. Additionally, there were two locations near the tip of

the Musandam Peninsula as the shipping lanes are tightest through that area. This covered most of the region's flow regimes and gave a wide look to possible outcomes. Site locations also were based on closest grid points. COAMPS grid points were utilized for location and the SWAFS grid points closest to those were chosen for individual site input. Figure 40 shows the locations of the four sites chosen. Sites 1 and 2 are at the tip of the peninsula, Site 3 is on the eastern leg towards the GOO, and Site 4 is on the western leg.
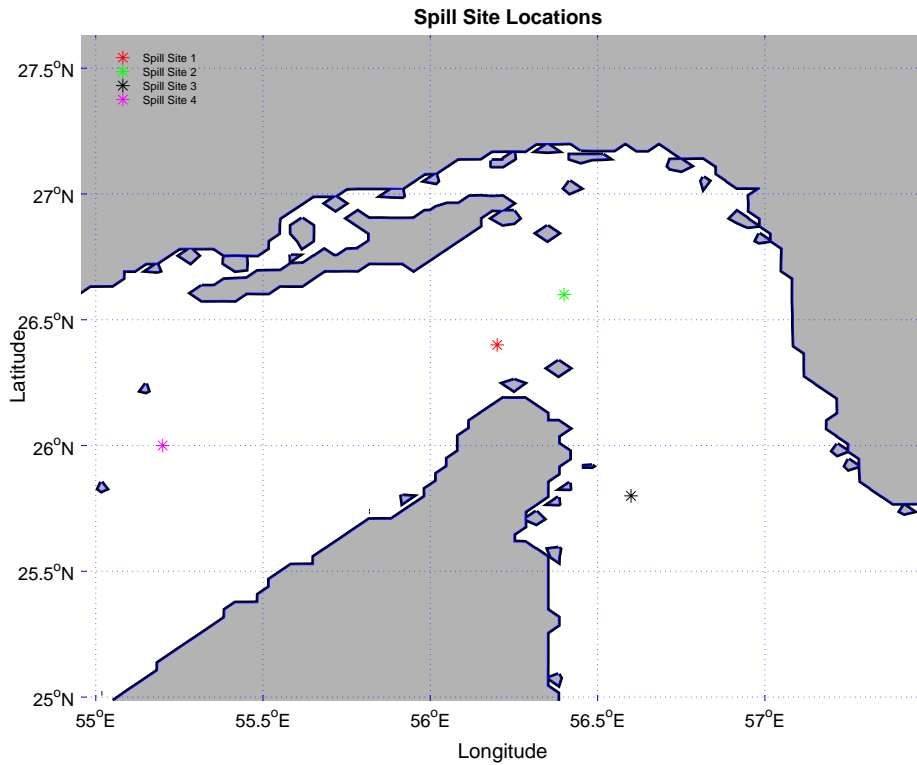
Figure 40.   Spill Site Locations

Spill Site	SWAFS		COAMPS	
	Lat (deg N)	Lon(deg E)	Lat(deg N)	Lon(deg E)
1	26.395	56.157	26.4	56.2
2	26.604	56.401	26.6	56.4
3	25.804	56.601	25.8	56.6
4	25.995	55.201	26.0	55.2

Table 5.   Nearest grid points of SWAFS and COAMPS for spill sites.

B. WIND AND CURRENT SELECTION

Four different wind and current regime combinations were established to examine the effect each had in the dispersion of oil. Each combination sought to establish extremes encountered in the environment to highlight differences from climatology. A time series of wind and current at all four of the selected spill sites was constructed and then compared to come up with the combinations necessary for evaluation. Each combination of high and low for wind and current was sought at each spill site to cover a five day period optimally. The following is the result of those efforts. Figures 41 to 44 were used to select the following scenario combinations. Notice that the flat areas highlighted by red indicators were data replaced by the overall mean as discussed earlier.

1. Low Wind/Low Current

Low wind and current occurrences occurred quite a few times at all spill sites. For ease of evaluation the occurrences in February were utilized. Low wind was defined as wind below 6 m/s and Low current was defined as current less than 60 cm/s. Acceptable limits were available at Site 1 from 10 to 15 February, at Site 2 from 7 to 12 February, and for Sites 3 and 4 from 5 to 10 February.

2. Low Wind/High Current

High current was defined as greater than or equal to 60 cm/s. Coinciding low wind and high current events were found in July for Sites 1, 3, and 4 covering the period 8 to 17 July. Site 2 had an acceptable event from 1 to 6 June.

3. High Wind/Low Current

High wind (defined as wind greater than or equal to 10 m/s) and low current events were almost identical for the first three sites and covered the period of 21 to 27 March. Site 4 had a coinciding event during the period of 17 to 22 February.

4. High Wind/High Current

The high wind high current coincidental events were not so easy to find. Although they occurred, they did not always occur for sufficient length of times. Site 1 had an event for 20 to 25 May. Site 2 did not have a coinciding event at all. Site 3 had an acceptable event 19 to 24 July. Site 4 had a short event covering 27 to 30 April.
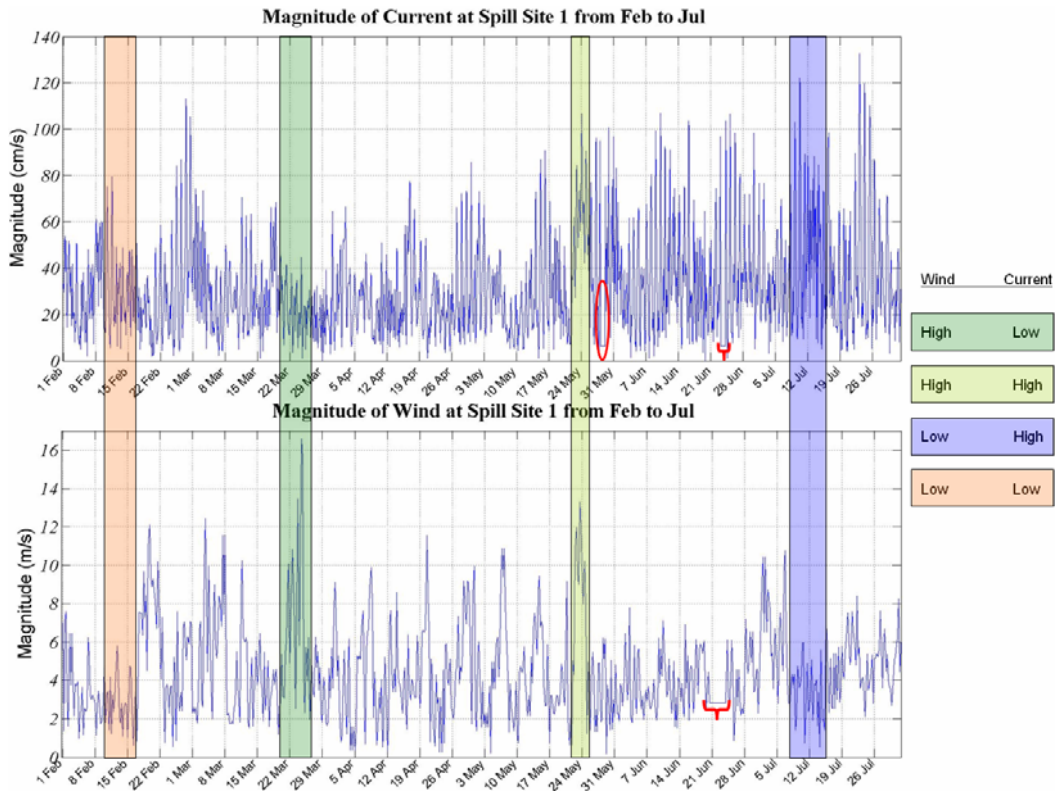
Figure 41.   Comparison of Magnitude Time Series plots for Site 1.
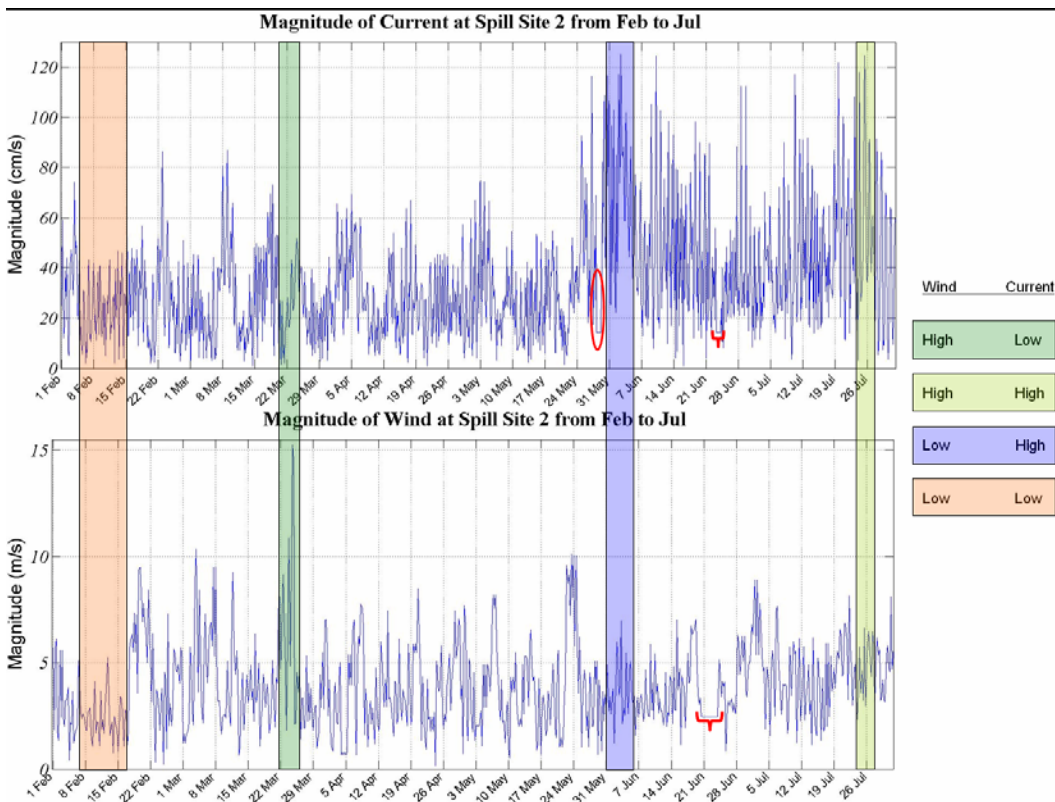
Figure 42.   Comparison of Magnitude Time Series plots for Site 2.

66
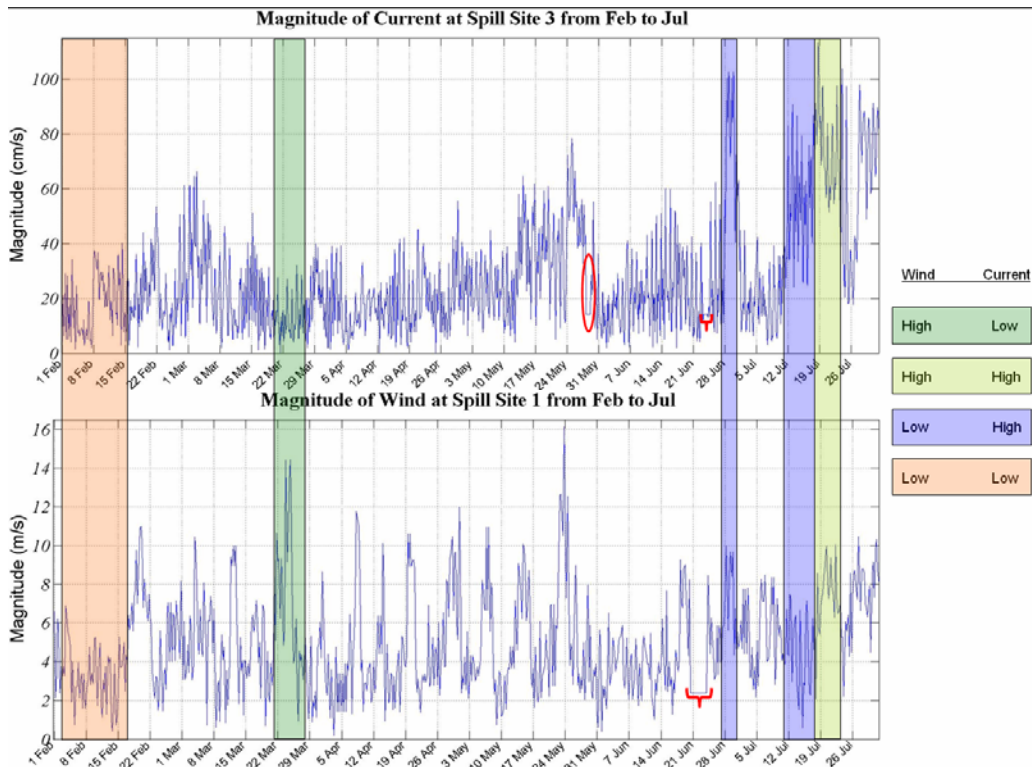
Figure 43.   Comparison of Magnitude Time Series plots for Site 3.
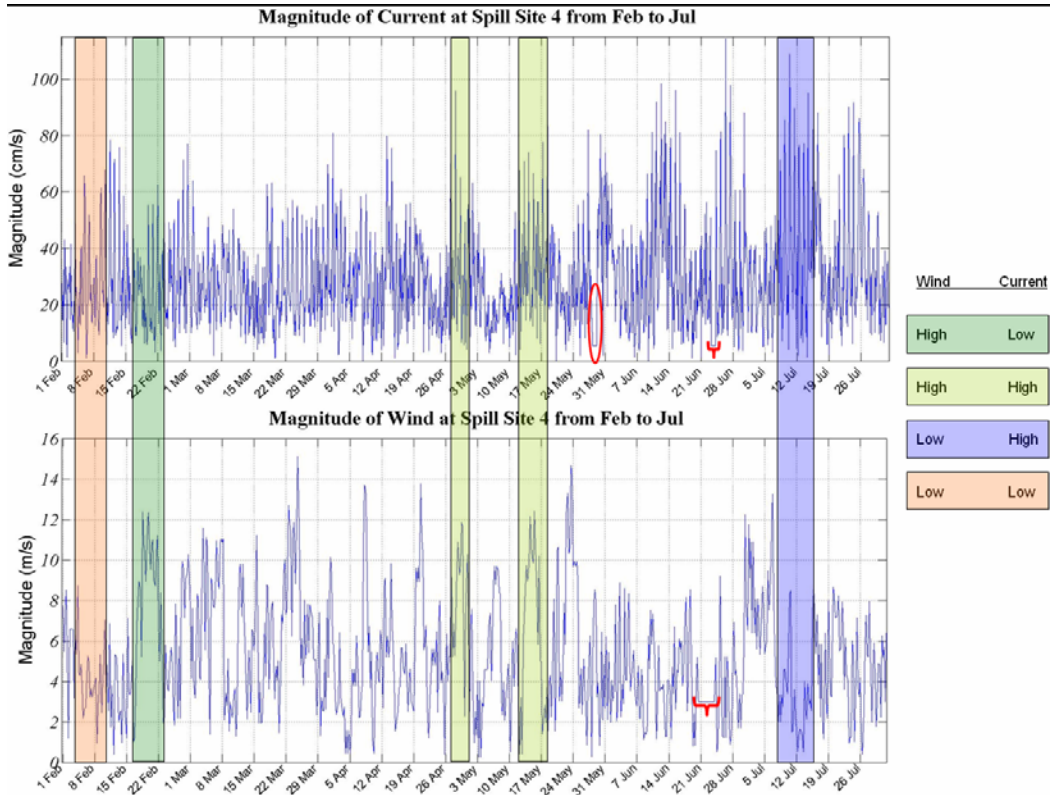
Figure 44.   Comparison of Magnitude Time Series plots for Site 4.

67

C.   CLIMATOLOGY

1.   Winds

Climatology was available for several coastal points but not anywhere near the identified spill sites.   Therefore, it was decided that the mean would be a sufficient replacement. Climatology winds are represented by the six month mean in this case. A time series was created by populating a matrix with the overall mean for the entire time period at each particular site in six hour time steps just as the real model fields were presented. The winds at spill sites are used to run the chemical model (OILMAP).

2.   Currents

Climatology currents are non-existent in the real world. Sea surface temperature, salinity, can all be obtained but the velocity of the water can not. So, in the spirit of trying to relate to the options operational planners would be faced with, the options to obtain a current input would be to look at archived data from previous years (research intensive), run at all angles (lengthy), or look at the last few months to see what the trends are. By using the mean the third choice was effectively picked.

VI. OIL SPILL PATTERNS

The oil scenarios, ran in OILMAP, were conducted using an arbitrary spill amount of 10,000 bbl (barrels). A barrel is equal to 40 gallons or approximately 0.13 tons. The spill was set to last for the duration of one hour and the oil was tracked for a period of up to five days. The temperature of the water was set according to the time of year the scenario took place in: For the winter period, 21 December to 21 March, the water was set to 22 °C. For spring, 21 March to 21 June, water was set to 27 °C. Summer, 21 June to 21 September, water temperature was set to 31 °C. The oil type used was Kuwait crude oil. The reasoning for using this particular oil is that it seemed to be representative of oil found in the area. In these scenarios the oil in the water column is far less than that on the surface and is not discussed; however, it is unknown as to how this would affect mine sweeping operations if at all. Anytime sound travels through a layer of different density it refracts and reflects according to incident angle and the density of the fluid at the interface. (This interaction is not part of this study but may be a potential for future research.)

A. OIL IN THE MARINE ENVIRONMENT

Factors affecting oil in sea water include wind speed, sea state, currents, and water temperature. These affect the different processes oil goes through once encountering the surface of the water. These processes include: evaporation, emulsification, spreading, solution, sea-air interchange, and sedimentation (Wilson et al., 1975). These processes make up the whole of the term "weathering."

The type of oil is also a factor since each type has its own particular mix of hydrocarbons and distillates. For instance, the oil used in these scenarios is Kuwait crude oil and probably has an entirely different molecular make up than oil from Venezuela or the Gulf of Mexico.

The most rapid event that happens to oil once it hits the surface is evaporation and it decreases exponentially over time. Over time weathering can turn a light crude oil into a viscous material or even a semi-solid. Wave action can cause water-in-oil emulsifications called "chocolate mousse" or simply "mousse" due to the color and

consistency of the material. As the percentage of water droplets to oil increases the color of the "mousse" lightens and can become more of a yellowish hue (Whitham et al., 1974). Weathering of oil can continue after it floats ashore. Unevaporated oil spreads on the water and thins as it does so. Berridge et al. (1968a, b) calculated that 100 cubic m of various crude oils will thin to an average value of 0.055 cm after only 17 minutes, 0.012 cm after three hours, and 0.003 cm after 28 hours. The thinner the surface of the oil the faster it weathers. As a result, the greater the rate and extent of oil spreading, the greater the rate of evaporation it undergoes.

B. ASSUMPTIONS

In the case of the simulations, the oil is left to spread and be acted upon by the environment without human intervention. In reality, this may or may not be the case. Satellite photos show oil slicks in the SOH and it is not known whether the countries bordering the SOH have any sort of response plan for a spill of any size. Assuming there is a plan in place by Iran, Oman, or the UAE, the presence of clean up efforts would cause a problem with traffic. At worst, it is estimated that traffic would slow down in the case of an accidental spill.

It is assumed that an explosion would be another story. A ship in distress would cause any available ship to respond to the distress of the crew. Another factor would be discovery as to the cause of the explosion. The presence of mines would preclude clean-up efforts in favor of mine sweeping. Naval operations in the area, along with civilian traffic would be effectively halted until the area could be pronounced clear.

C. SITE 1

1. Low Wind/Low Current

The spread of the oil over the five day period (10-15 Feb) was contained within the SOH at the tip of the peninsula (see Figure 45). Following initial release, the oil was pushed in the outflow direction and then is shown to stall at the tip of the peninsula after 24 hours (see Figure 45 a). Then, after 72 hours (b), the oil is once again caught in an outflow regime. In the last frame (c), the oil has been caught in an inflow type regime. In this case the oil did not go very far or make landfall.

The Mass Balance Graph (d) shows the rapid initial evaporation that occurs and the exponential decrease in evaporation rate with time. Note that the oil spreads across

the SOH for a significant distance covering the inbound and outbound transit lanes. The transit lanes are in the middle of the oil at the end of the first day and remain among the lanes to conclusion of the simulation time.

Figure 45.   Site 1 Low Wind/Low Current: a.) at 24 hours, b.) at 72 hours, c.) end state at the conclusion of five days, and d.) Mass Balance Graph.

2.   Low Wind /High Current

Much like the low wind and current scenario, the oil remained in the SOH around the peninsula (Figure 46). The spill tarried at the tip of the peninsula, caught in the peninsular eddy, before being pushed to the northwest and making landfall on the small island directly north of the peninsula (Larak Island). It was concluded that the oil was influenced primarily by the current from the track of the slick. However, this time the oil

did make landfall on the last day. The effect on the amount of oil on the surface is to decrease it in addition to the evaporation loss (Figure 46).

Also, the oil traveled across the transit lanes northward towards Iran. Clean-up efforts would interfere with transiting as the oil slick does not clear the transit lanes until after the third day.

Figure 46. Site 1 Low Wind/High Current: a.) at 24 hours, b.) at 72 hours, c.) end state at the conclusion of five days, and d.) Mass Balance Graph.

3. High Wind /Low Current

The high wind/low current scenario shows the oil to be driven to the southwest along the coast of the peninsula (Figure 47). The spill begins to make landfall on the third day (Figure 47 b) and continues to oil the coast until the fourth day when all oil is

washed ashore (Figure 47 c). The oil does not affect shipping in this case and becomes a problem for environmental cleanup rather rapidly. Transit lanes are clear from the moment the spill begins. Winds in this case were to the southwest.

a.)

b.)

c.)

d.)
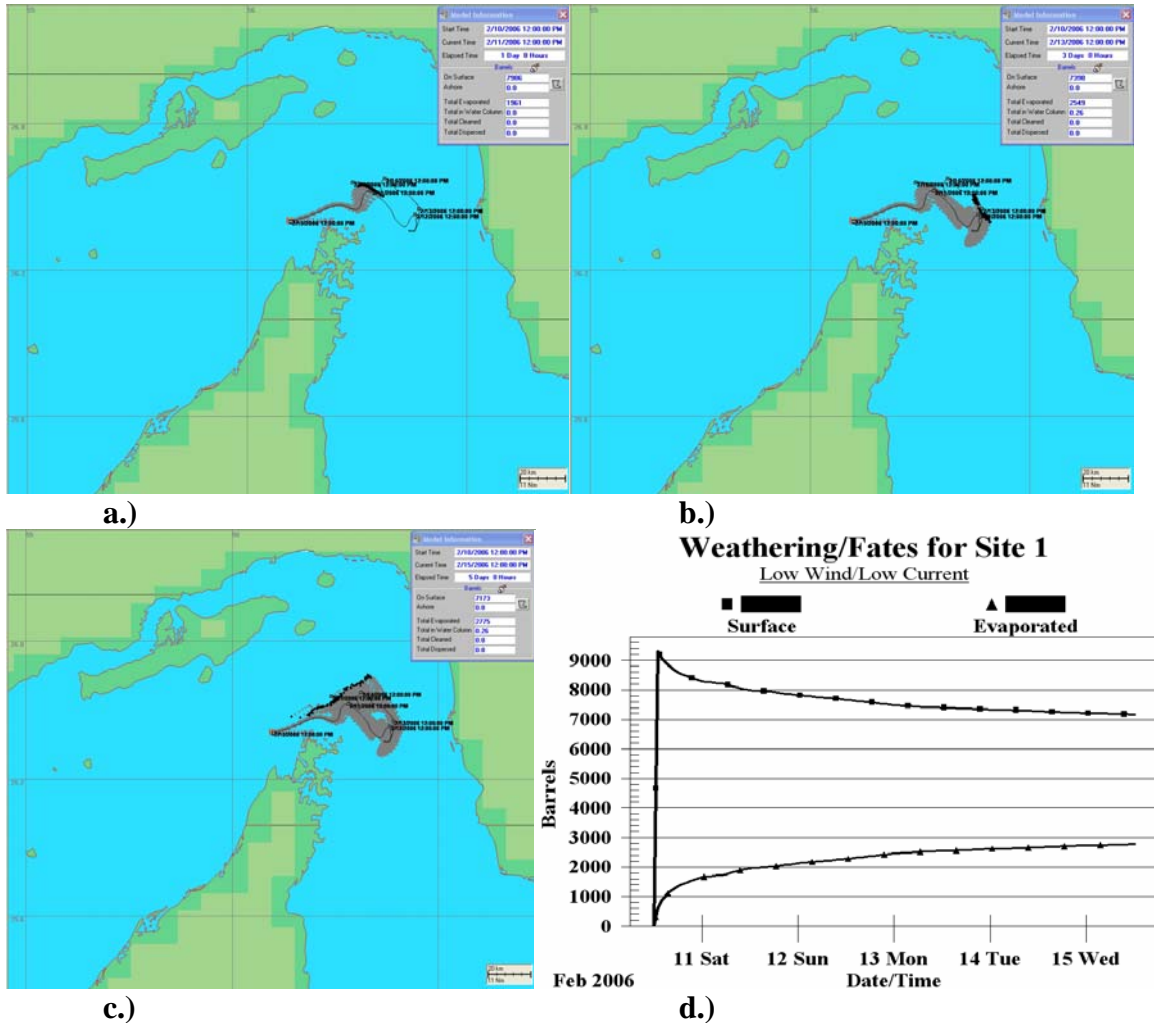
Figure 47.   Site 1 High Wind/Low Current: a.) at 24 hours, b.) at 72 hours, c.) end state at the conclusion of five days, and d.) Mass Balance Graph.

4.   High Wind /High Current

In the case of high wind and high current the winds were to the northeast as were the currents. Understand that this is for the release point only. At the two and a half day mark the oil first makes landfall (Figure 48). Upon inspection of the current and wind composite the winds were southwesterly on 22 May and the current was also. However, an anticyclonic eddy was positioned directly to the east of the peninsula. The turning of the oil took place in the first 24 hours (Figure 48) when a short period of weakened winds

and currents took place. The wind was slightly to the southeast and was enough to turn the oil towards the peninsula. In this case the oil was clear of the transit lanes after the first 24 hours.
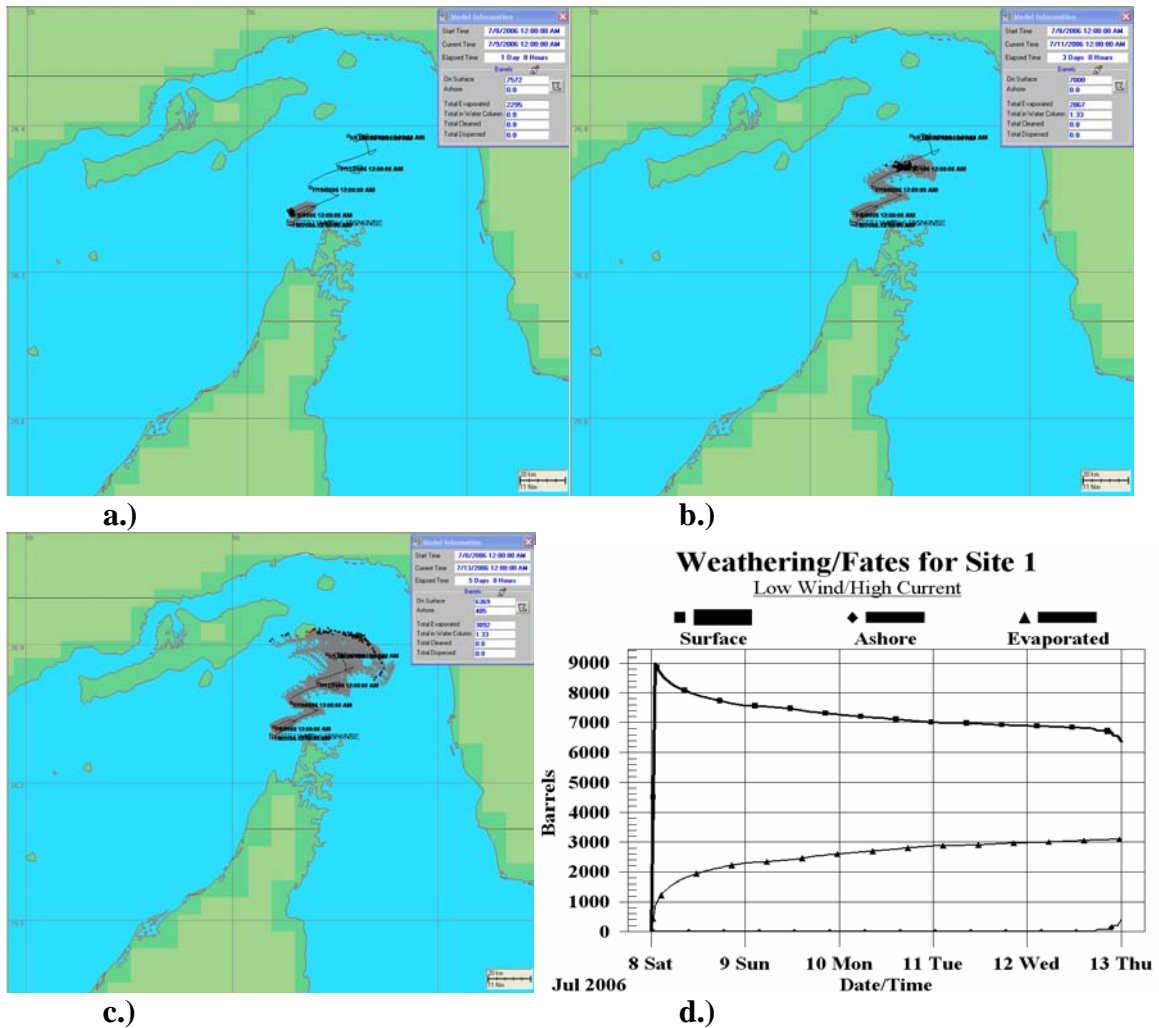

Figure 48.   Site 1 High Wind/High Current: a.) at 24 hours, b.) at 72 hours, c.) end state at the conclusion of five days, and d.) Mass Balance Graph.

D.   SITE 2

1.   Low Wind /Low Current

Site 2 is closer to the inbound transit lanes and possible joining point for traffic from Bandar Abbas. The spill in this scenario reacts much like the scenario from Site 1. The oil does not make landfall in five days; however, it is clear of the transit lanes almost immediately following the spill (Figure 49 a). The weathering of the oil is restricted to evaporation since it does not meet the land (Figure 49 c).

74
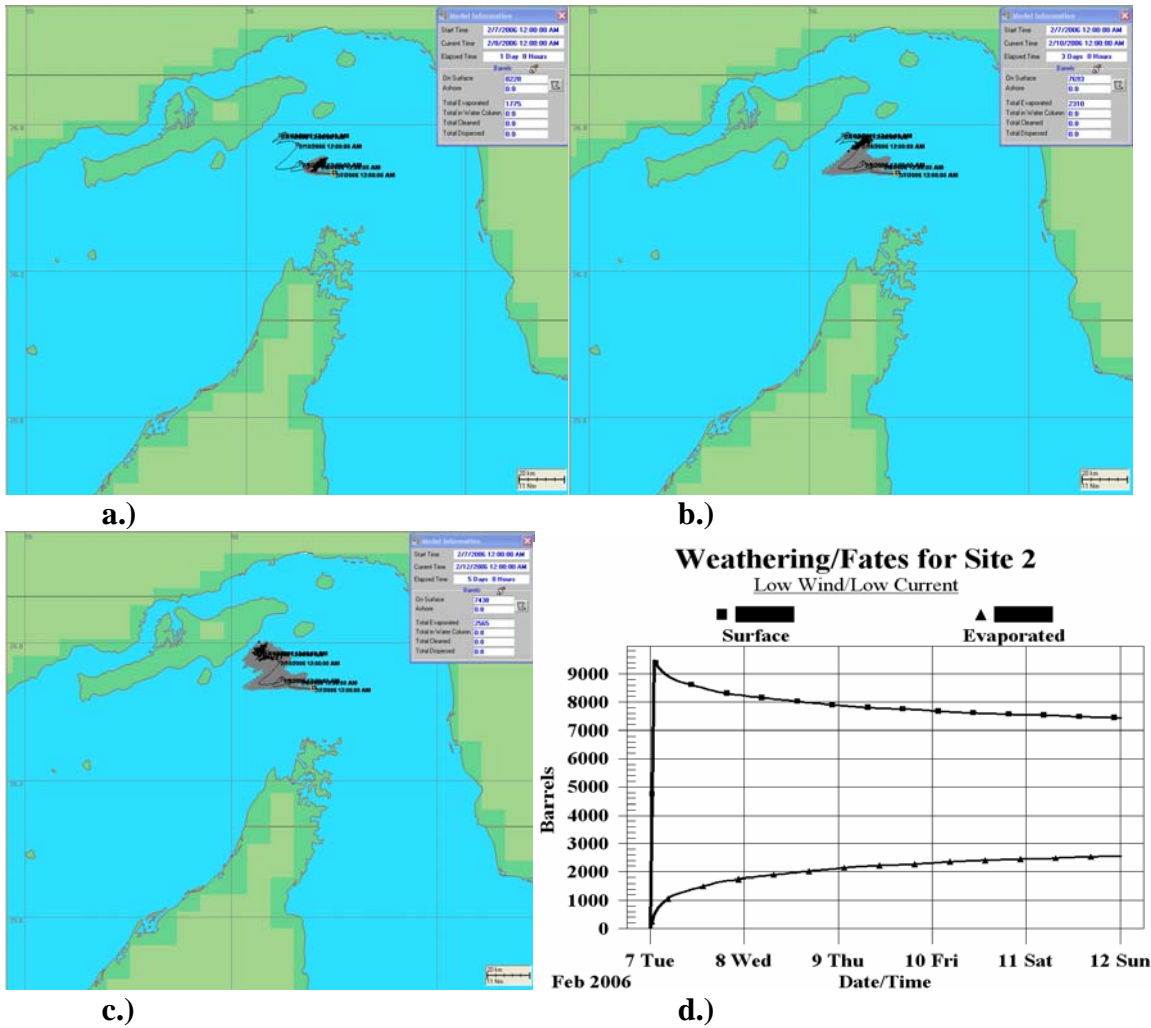
Figure 49. Site 2 Low Wind/Low Current release point and end state at the conclusion of five days and Mass Balance Graph.

2. Low Wind /High Current

Much like the previous scenario, the oil spread towards the island of Queshm except it actually made landfall this instance (Figure 50). Again, the oil slick cleared the transit lanes almost immediately (Figure 50 a). The landfall occurs halfway into the second day and continues to do so in waves across the third and fourth days (see Figure 50). The slick was pushed initially to the east since the strait was experiencing an outflow regime. The strong switch to the west was due to the strong inflow and southerly wind halfway through the first day. A short outflow regime coupled with the weak southerly wind pushed the slick to the small island to the north of the spill site (Larak) halfway through the second day. More southerly winds persisted for the next few days

pushing the slick into the islands of Queshm (large island to the west of the spill site) and Hengam (the smaller island to the south of Queshm).

a.)   b.)

c.)   d.)
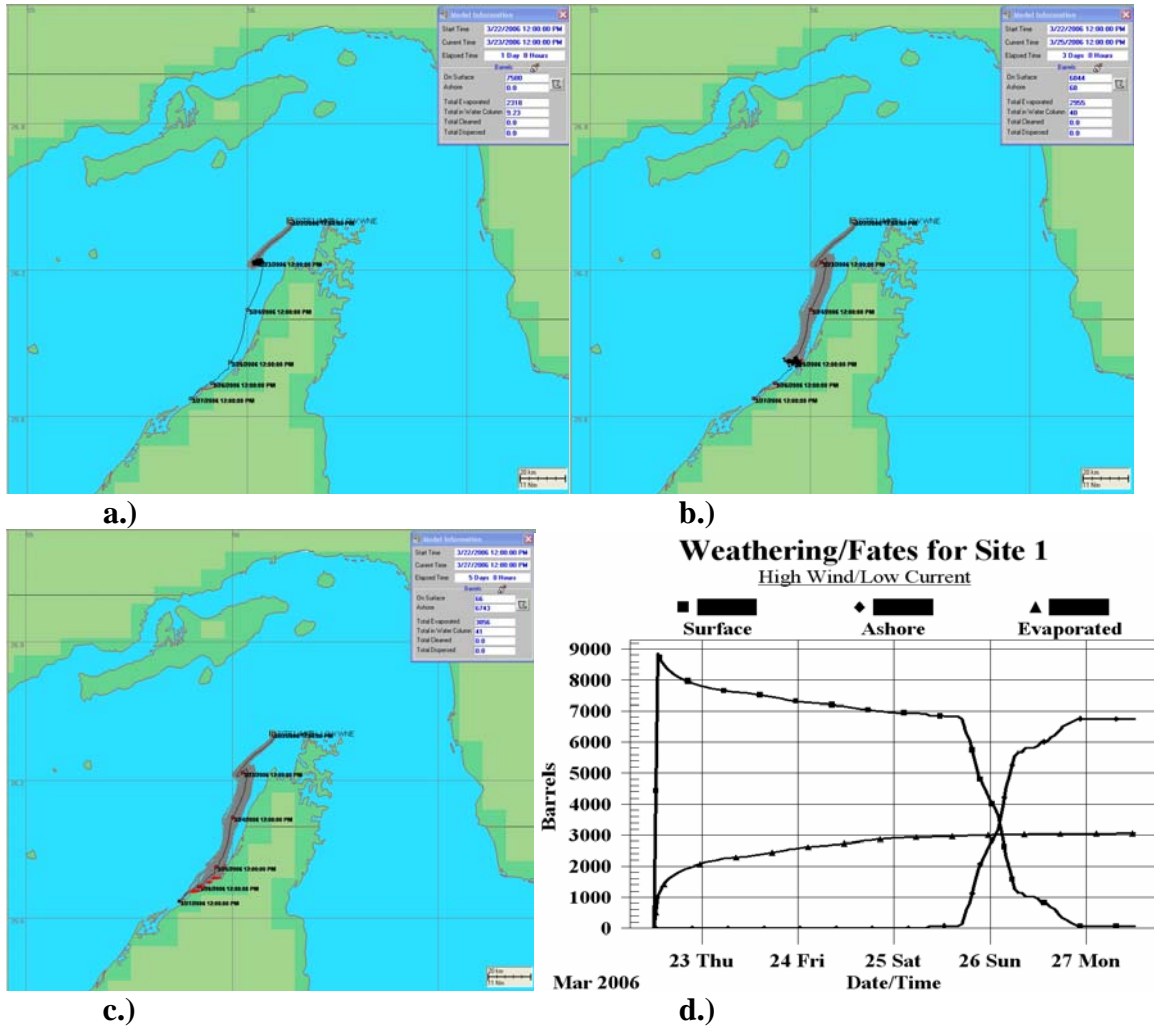
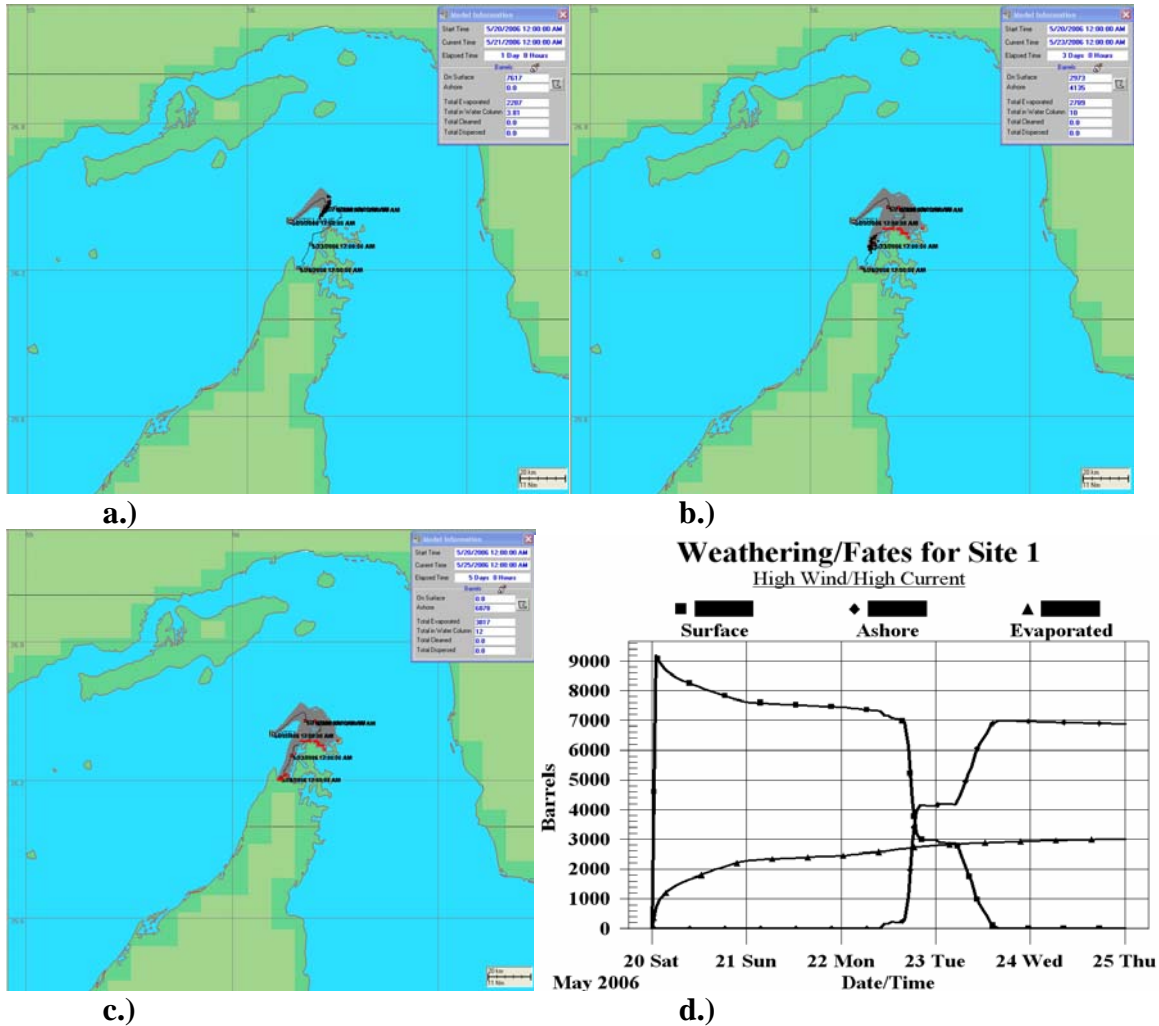Figure 50.   Site 2 Low Wind/High Current: a.) at 24 hours, b.) at 72 hours, c.) end state at the conclusion of five days, and d.) Mass Balance Graph.

3.   High Wind /Low Current

The high wind and low current scenario for Site 2 shows the oil pushed to the east leg of the SOH. It appears to hit an eddy in the area and spreads during lulls in the wind. Indeed, after inspecting the current and wind vectors for 24-26 March, the wind was almost straight westerly at about 10 m/s then underwent a transition to southwesterly and died to about 3-5 m/s. This scenario became a transition scenario from high wind/low

current to low wind low/low current. The spreading effectively seals off the transit lanes and the oil never makes landfall (Figure 51). Oil weathering is due to evaporation only (Figure 51).

Figure 51.   Site 2 High Wind/Low Current: a.) at 24 hours, b.) at 72 hours, c.) end state at the conclusion of five days, and d.) Mass Balance Graph.

E.   SITE 3

1.   Low Wind /Low Current

The low wind and low current scenario for Site 3 shows the oil partially making landfall into the fourth day and again on the fifth day. The spill is initially away from the transit lanes and then drifts northeast into the outbound lanes around the fifth day (Figure 52). Weathering is a combination of evaporation and landfall (Figure 52).

Figure 52.   Site 3 Low Wind/Low Current: a.) at 24 hours, b.) at 72 hours, c.) end state at
the conclusion of five days, and d.) Mass Balance Graph.

2.   Low Wind /High Current

The spill in this scenario crosses the outbound and inbound transit lanes within the first 24 hours and then is confined to the coast of Iran. After briefly making landfall the spill is pushed out to the GOO (Figure 53). The mass balance graph reveals that the oil makes landfall in four separate instances over a 24 hour period (Figure 53).
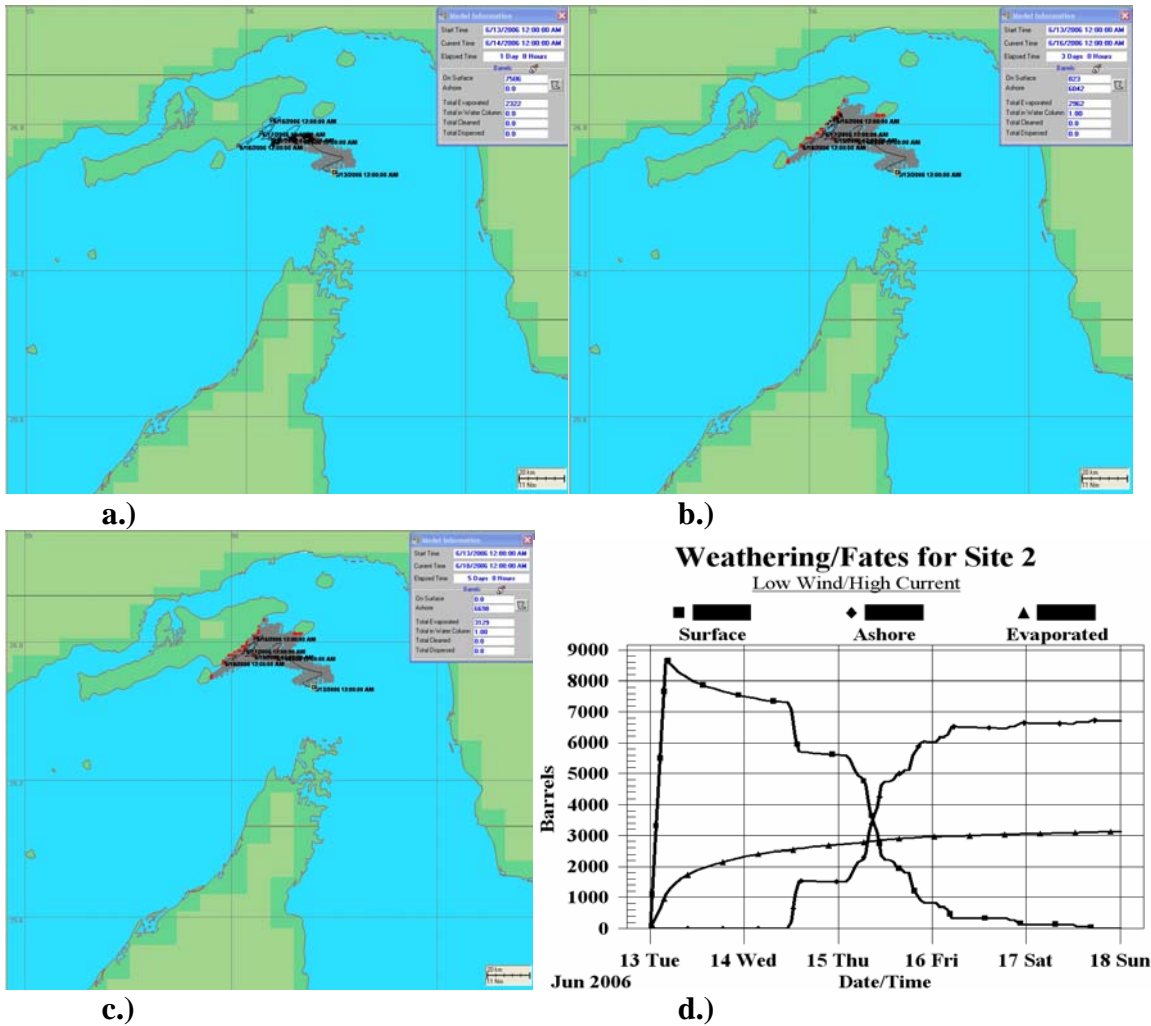
Figure 53.   Site 3 Low Wind/High Current: a.) at 24 hours, b.) at 72 hours, c.) end state at the conclusion of five days, and d.) Mass Balance Graph.

3.   High Wind /Low Current

The view from the track shows the spill immediately pushed to the south and not apparently making landfall (Figure 54). However, the mass balance graph shows that the spill indeed does make landfall out of the view if the picture on the fifth day (Figure 54). If the view was zoomed out the landfall would be shown. Since the SOH is the area of concern this is not a necessity.

a.)

b.)

c.)

Weathering/Fates for Site 3
High Wind/Low Current

d.)
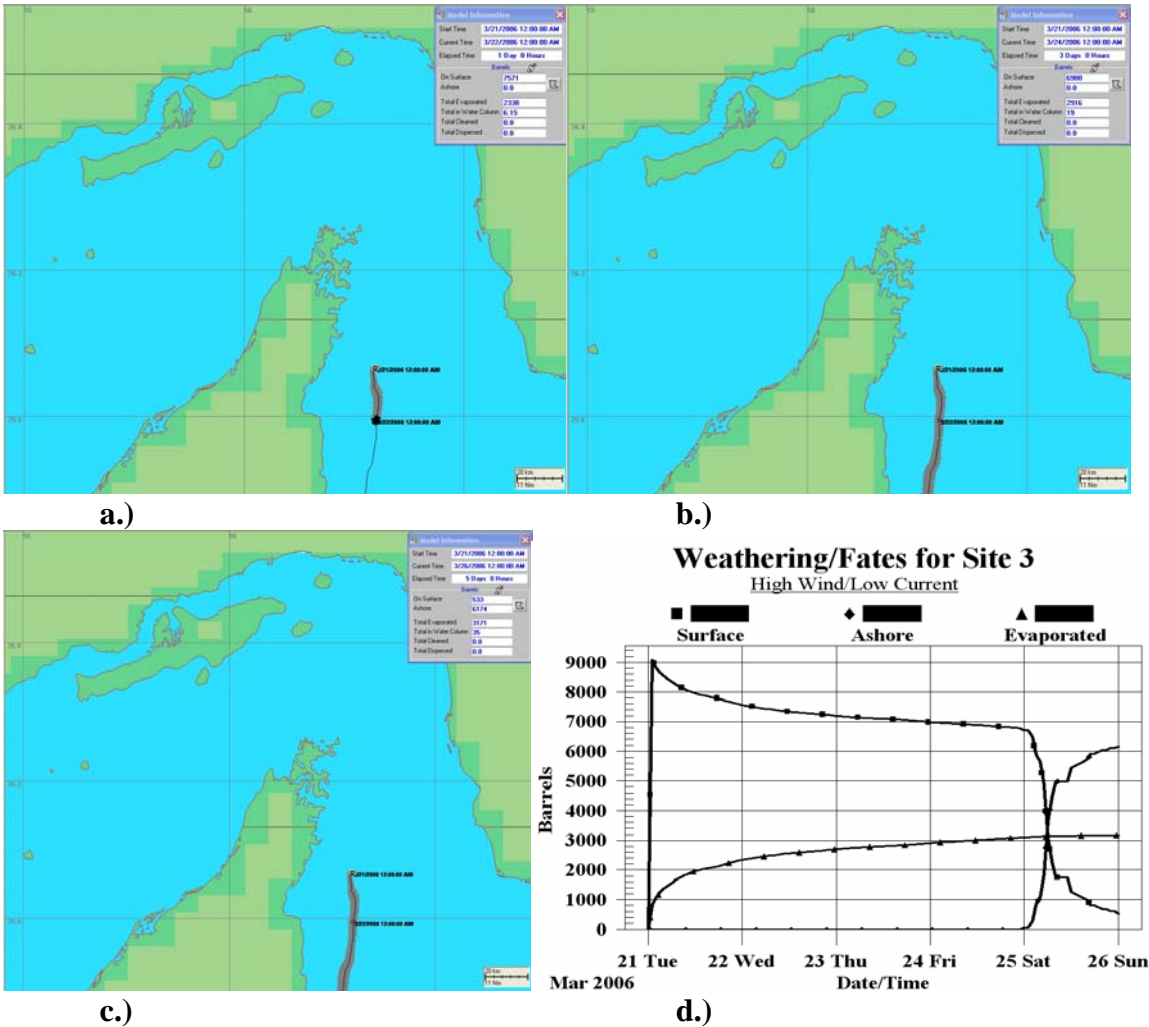
Figure 54.   Site 3 High Wind/Low Current release point and end state at the conclusion of five days and Mass Balance Graph.

4.   **High Wind /High Current**

In this scenario the spill makes contact with the peninsula on the second day and a small portion finally makes landfall on Queshm Island on the third day (Figure 55). The mass balance graph echoes the visual representation and adds that the rest of the oil takes until the end of the fifth day to totally make landfall (Figure 55).
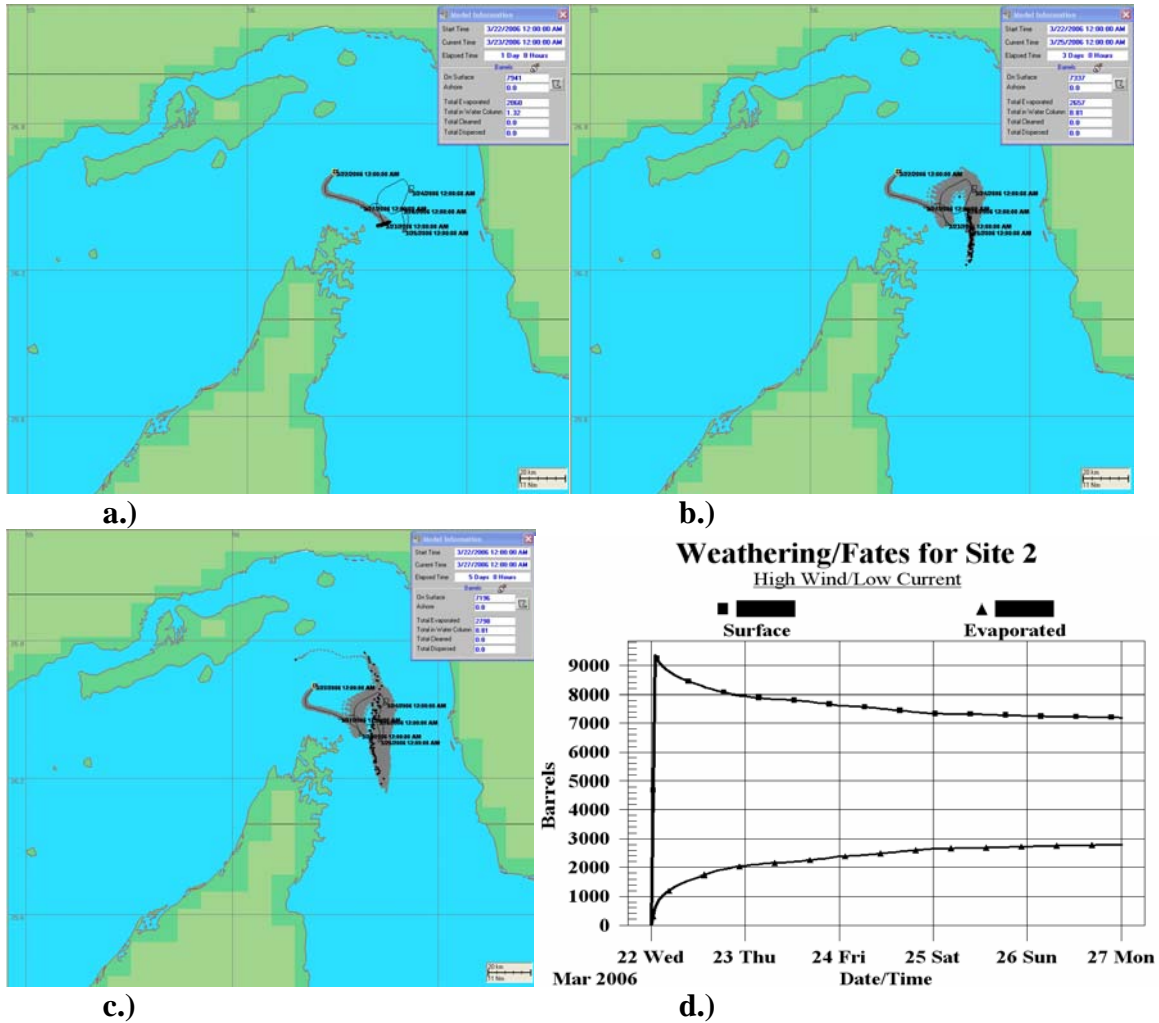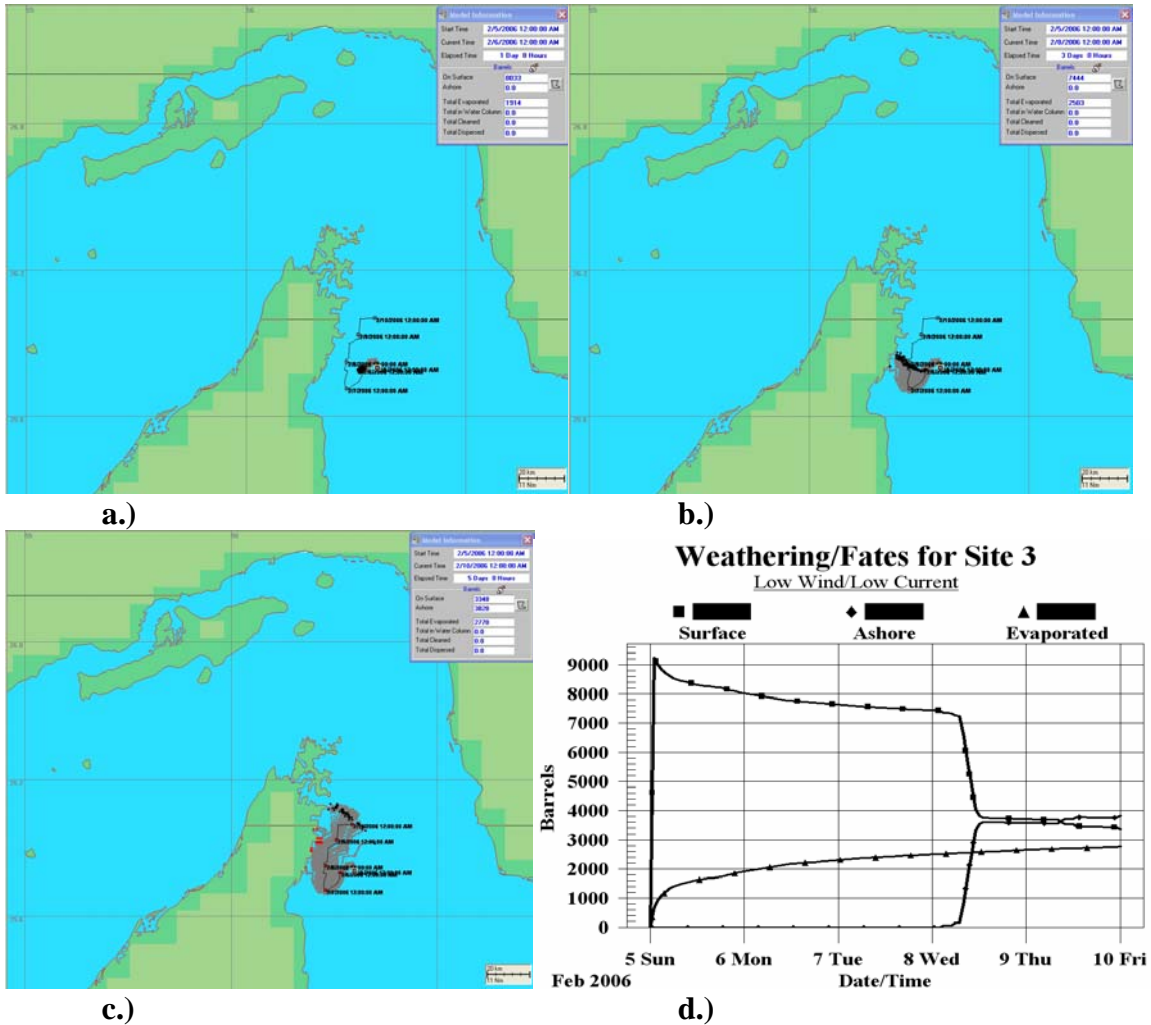
Figure 55.　　Site 3 High Wind/High Current: a.) at 24 hours, b.) at 72 hours, c.) end state at the conclusion of five days, and d.) Mass Balance Graph.

F.　　SITE 4

1.　　Low Wind /Low Current

In this scenario the oil made landfall by slightly oiling the eastern side of Abu Musa at the end of the second day (Figure 56). Meanwhile, the rest of the slick was moved around the island to make a greater landfall on the western side of the island before the rest of the spill is drawn away. The oil was briefly drawn to the southwest and back to the north east towards Lesser Tunb Island.

The Tunb islands straddle the inbound and outbound transit lanes. Hence, the reason for this site location. This also means that this spill traveled around and through

both transit lanes and was a surface feature to the fifth day. The mass balance graph shows the timing of the landfall events (Figure 56).

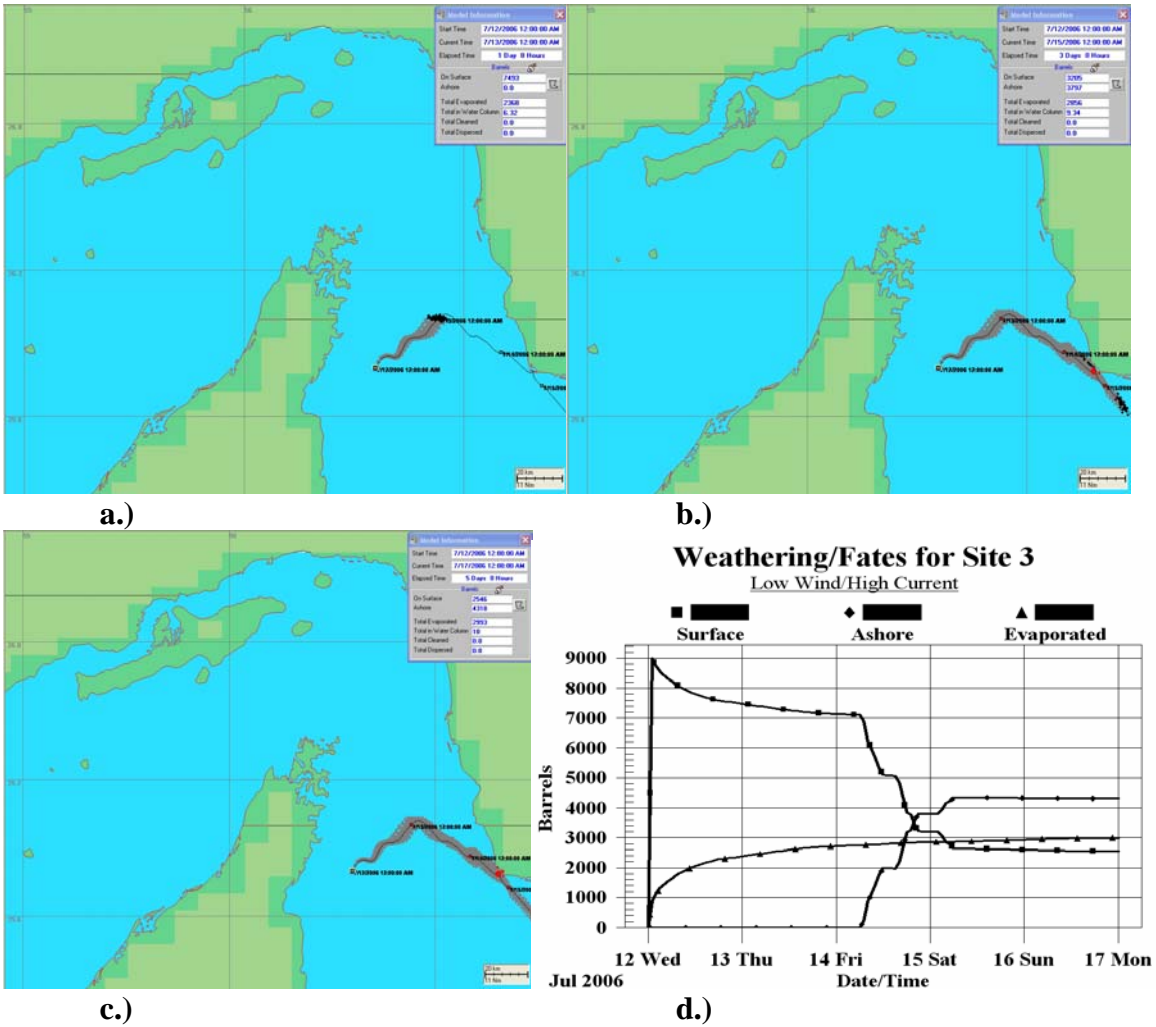
Figure 56. Site 4 Low Wind/Low Current: a.) at 24 hours, b.) at 72 hours, c.) end state at the conclusion of five days, and d.) Mass Balance Graph.

2. Low Wind /High Current

This scenario showed the greatest dispersion from this site and an outflow type regime took place during the time after release of the spill. The spill was pushed towards the tip of the peninsula by the third day where it spread north and south. Residence time was for almost two days while the slick spread from the peninsula to the islands of Hengam and Queshm (Figure 57). Since the slick did not make landfall it only underwent evaporation (Figure 57).

Figure 57. Site 4 Low Wind/High Current: a.) at 24 hours, b.) at 72 hours, c.) end state at the conclusion of five days, and d.) Mass Balance Graph.

3. High Wind /Low Current

This spill was rather straightforward. The slick was pushed to the south by a combination of winds and currents where it made landfall on the third day (see Figure 58). The mass balance graph shows the landfall occurred to totality over about a six hour period (see Figure 58).
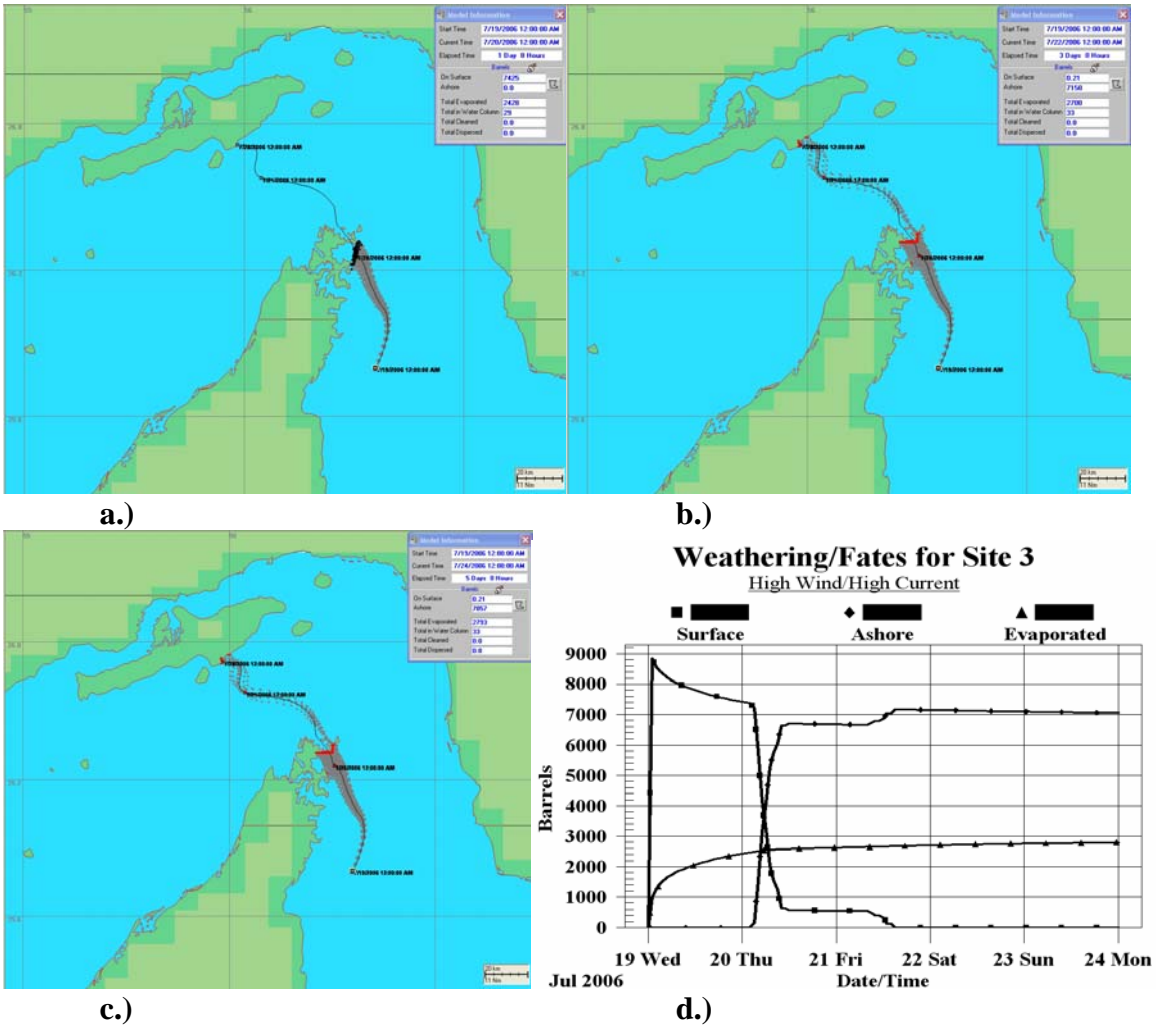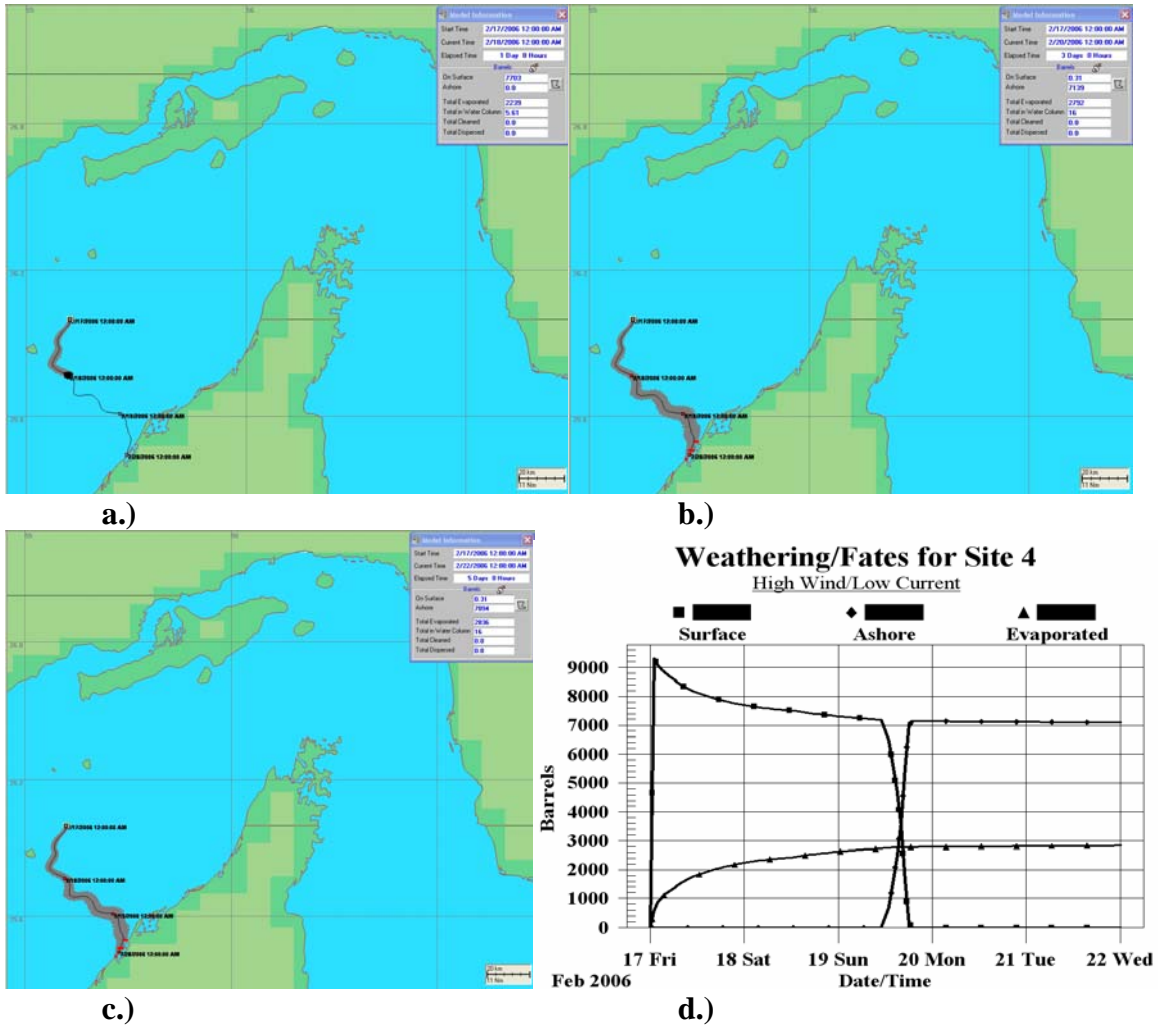
Figure 58. Site 4 High Wind/Low Current: a.) at 24 hours, b.) at 72 hours, c.) end state at the conclusion of five days, and d.) Mass Balance Graph.

4. High Wind /High Current

Like the previous scenario, this spill headed south and met the coastline of the UAE; however, the landfall was out of view (Figure 59). The spill was pushed further south and consequently it took longer for the oil to make landfall. The effect on transit lanes was minimal since the slick was south of the transit lanes by the end of the first day (Figure 59).
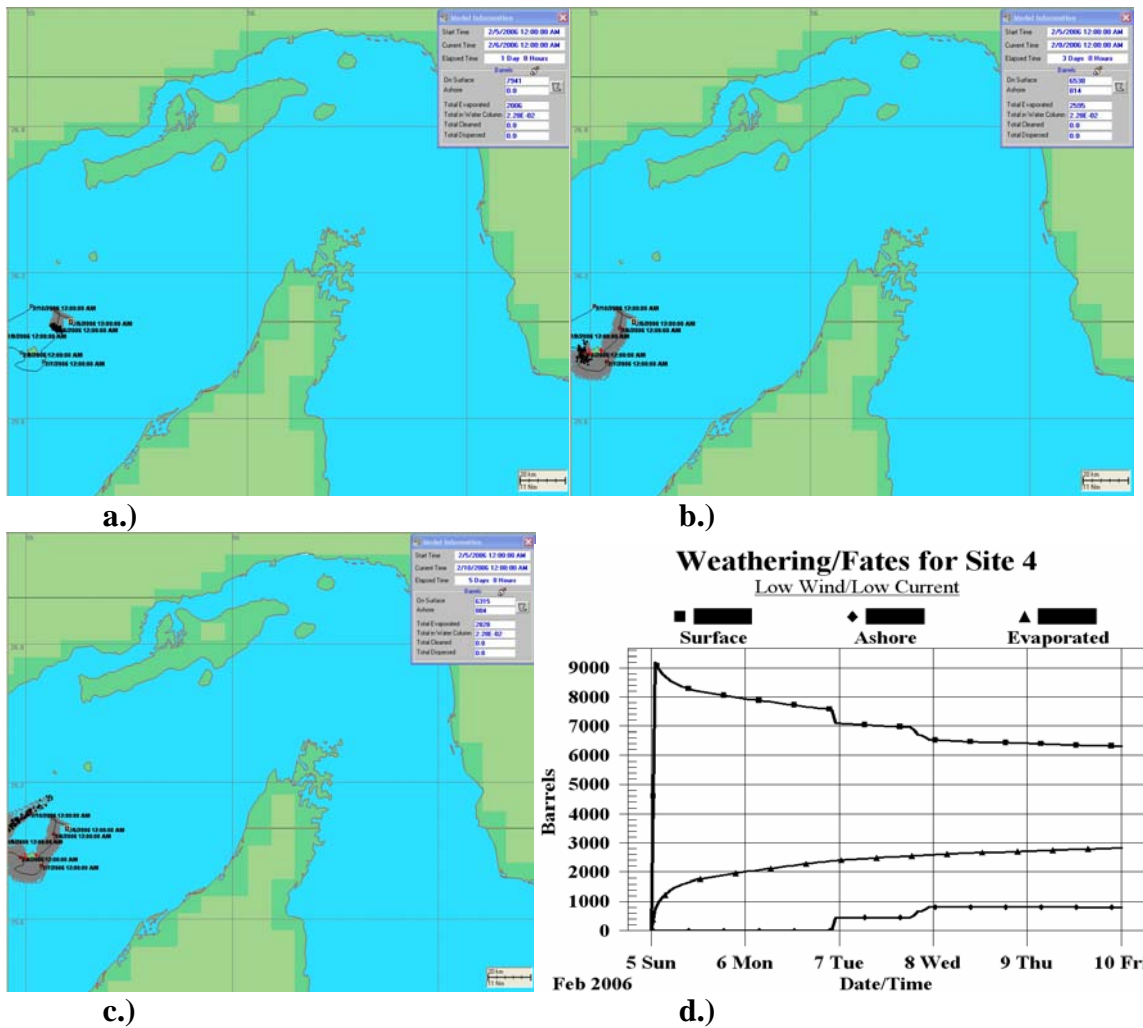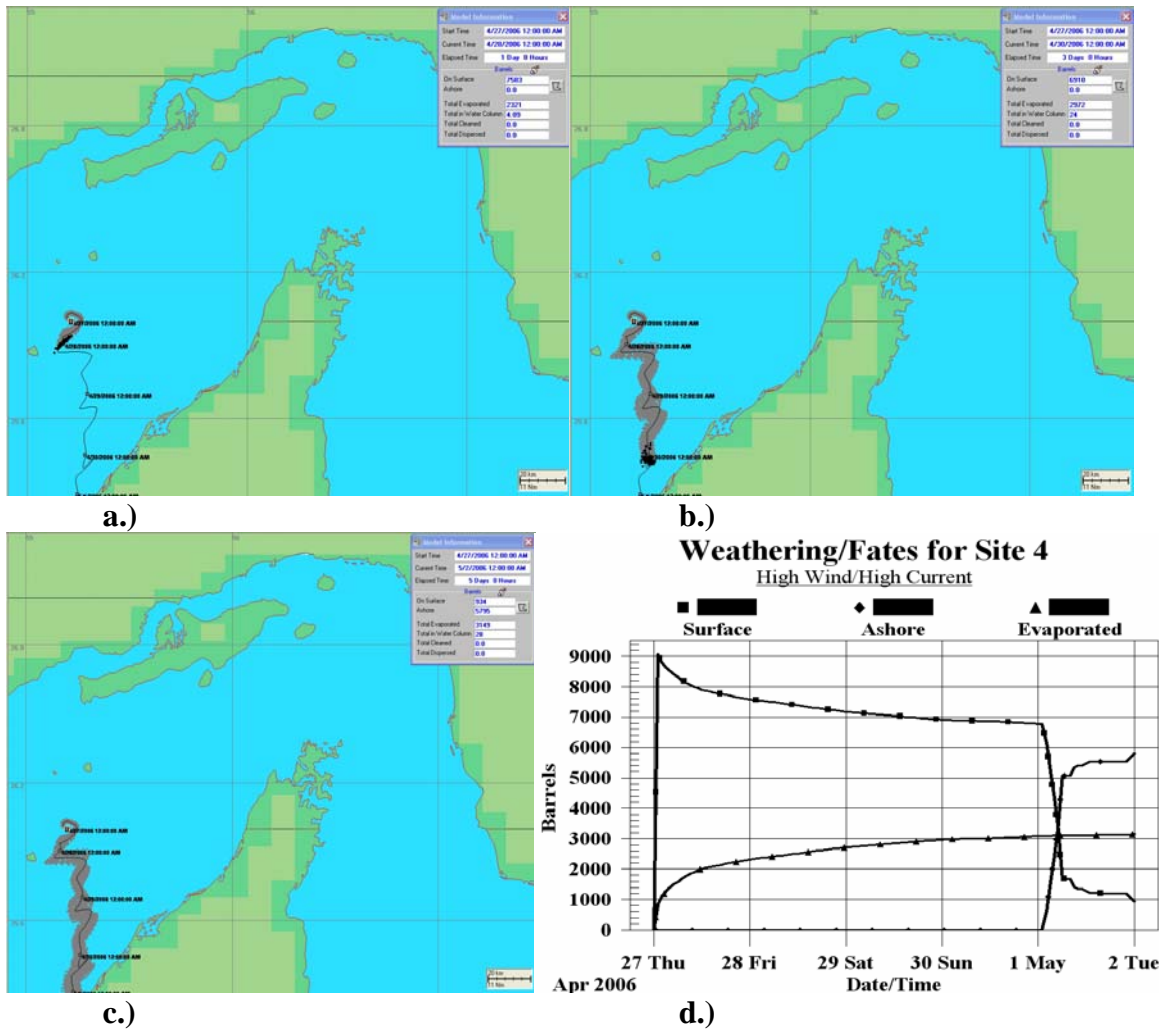
Figure 59. Site 4 High Wind/High Current: a.) at 24 hours, b.) at 72 hours, c.) end state at the conclusion of five days, and d.) Mass Balance Graph.

G. MODEL-DRIVEN SUMMARY

1. Site 1

Site 1 showed a variety of spill behaviors determined by the current and wind acting upon the oil slick. The distance covered by the slick and speed of landfall were all determined by these factors. Slick movement was restricted to the tip of the peninsula and the western leg of the SOH throughout the various combinations. Due to the tidal nature of flow through the SOH, the unidirectional movement does not last long. Transition from one flow regime to another causes the flow to lull or speed up depending on which regime is dominant at the time. Additionally, the wind does not maintain speed or direction for long. When the wind speed slowed below the 10 m/s mark the current seemed to become the dominant driver for oil slick movement.

2.   Site 2

Site 2 showed the oil slicks to be restricted to the tip of the peninsula and the eastern leg of the SOH. The interaction of the slicks with eddy flow seemed to cause greater dispersion. When the wind would slow the dispersion seemed to increase. The slowing, not necessarily the slow wind speed, seemed to aid dispersion.

3.   Site 3

Site 3 slicks seemed to be restricted to the eastern leg exclusively with the exception of the High Wind/High Current situation, and then the little oil that made it past the peninsula was less than 10% of the original spill. The dynamic forcing from outflow regimes and eddies contributed to the apparent trapping of oil slicks to the eastern leg.

4.   Site 4

Site 4 slicks were restricted exclusively to the western leg of the SOH. Site 4 best represents the highly variable nature of oil slick propagation with respect to directionality and distance. The various combinations of wind and current showed that the oil slick could go just about anywhere based on what the dominant driving force was. The amount of course changes and landfall behaviors showed the balance between wind and current.

H.   CLIMATOLOGY COMPARISON

The climatology runs for spill sites 1-4 were very unidirectional and tended to be slow. Since climatology was used, the runs did not exhibit any variations in flow associated with normal spill behavior. Without variation in wind speed and direction there were no periods where current could direct the steering more than any other time. Current direction and speed were dictated based solely on location of the spill. Time of the spill had no relevance. Tides would have made the time of the spill more important since their timing affects the direction of flow, and also force to a degree.

Site 1 was very slow in comparison to all of the runs made utilizing the model field inputs (see Figure 60 compared to Figures 45-48). Additionally, without the tidal influence, the slick maintained its direction with minimal spreading.
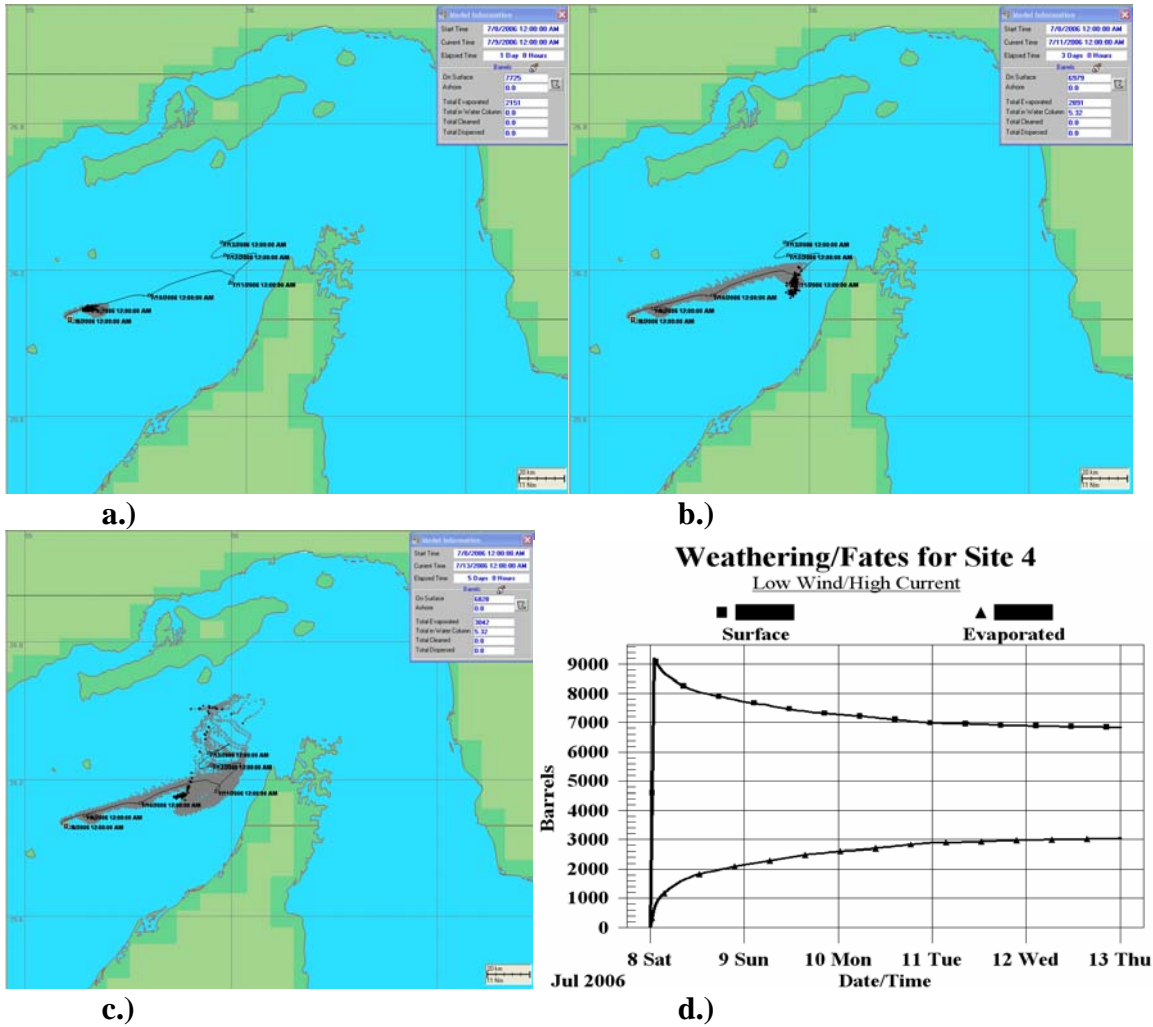
Figure 60.   Site 1 Climatology: a.) at 24 hours, b.) at 72 hours, c.) end state at the conclusion of five days, and d.) Mass Balance Graph.

Site 2 showed a more dramatic flow effect; yet, it was still unidirectional and with little spread (Figure 61). The slick made a long path into the western leg with no shift back to the east. The lack of tidal influence made the length of travel possible. If one inspects the entirety of Site 2 model field runs (Figures 49-51), the degree of tidal influence can be seen to prevent such long-term inflow. Also significant, the movement of the slick is in opposition to the mean wind flow. This is most likely due to the weak wind forcing from climatology winds (~ 4m/s). Without periods of high winds to act on the slick it moves primarily with the current.

Figure 61. Site 2 Climatology: a.) at 24 hours, b.) at 72 hours, c.) end state at the conclusion of five days, and d.) Mass Balance Graph.

Site 3 also showed the current, even weak current, to be more of a factor than the weak wind forcing at the eastern leg (~ 2m/s in Figure 62). The current at this location was less than 10 cm/s. The weakness of both current and wind amounted to the Low Wind/Low Current scenario from the model field run (Figure 52). The exception to the similarity ends with the magnitude of motion. No tidal forcing meant the continued push of the slick into the coastline of Oman. While contact with the peninsula was not uncommon to the scenario, the straight path taken was.

Figure 62.   Site 3 Climatology: a.) at 24 hours, b.) at 72 hours, c.) end state at the conclusion of five days, and d.) Mass Balance Graph.

Site 4 can also be related to the Low Wind/Low Current run (comparison between Figures 56 and 63). The climatology-driven run takes a couple of days longer to make landfall even though it is more direct path. This, of course, is due to the magnitude of forcing of the climatology (~ 5-8 cm/s current and ~ 3 m/s wind). Although the direction is fairly good, the timing is way off between the two. Periods of higher flow allow the model field-driven run to impact both the eastern and western shores of the island of Abu Musa; whereas, the climatology-driven run only shows the beginning of oiling of the eastern shore.
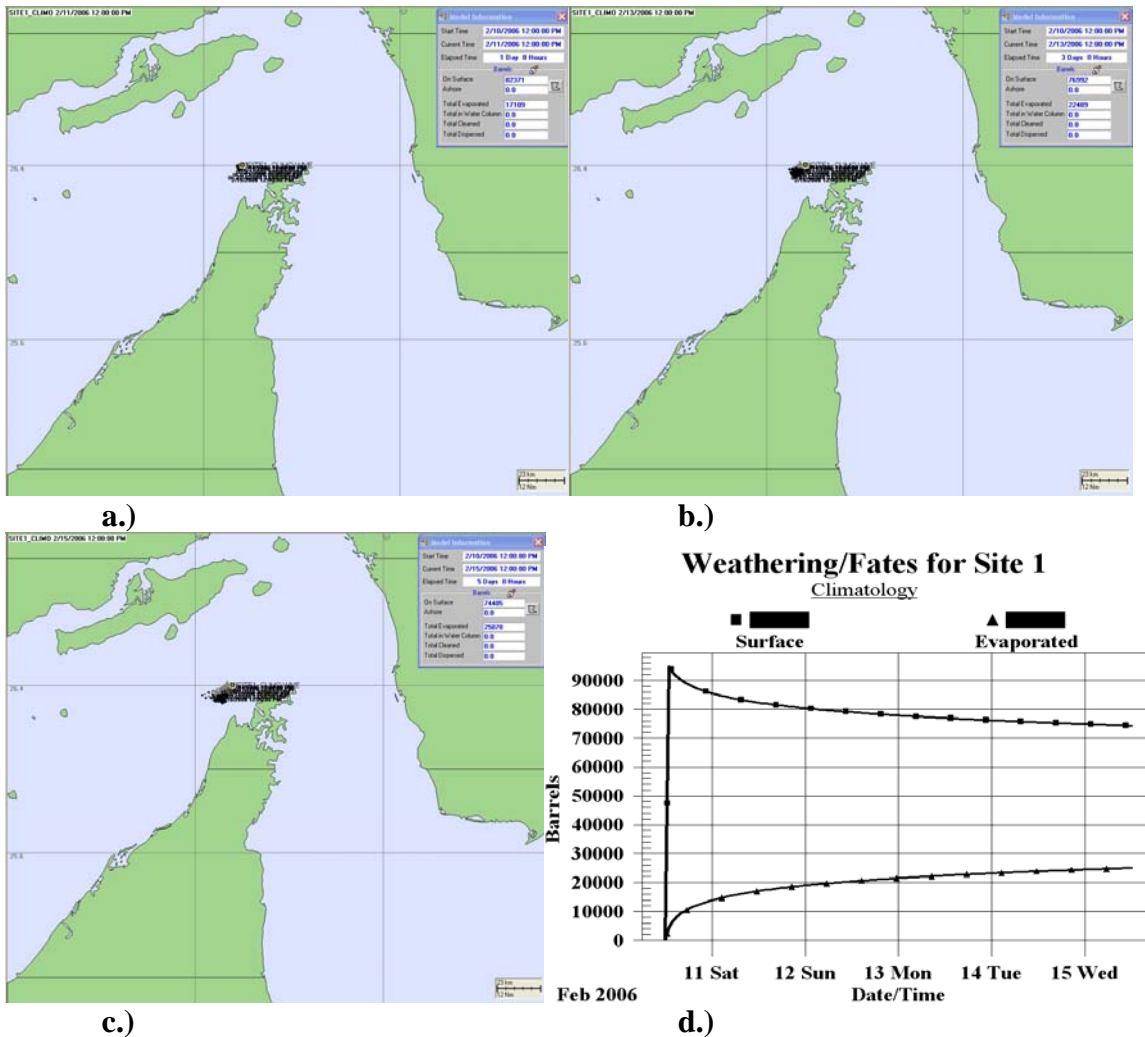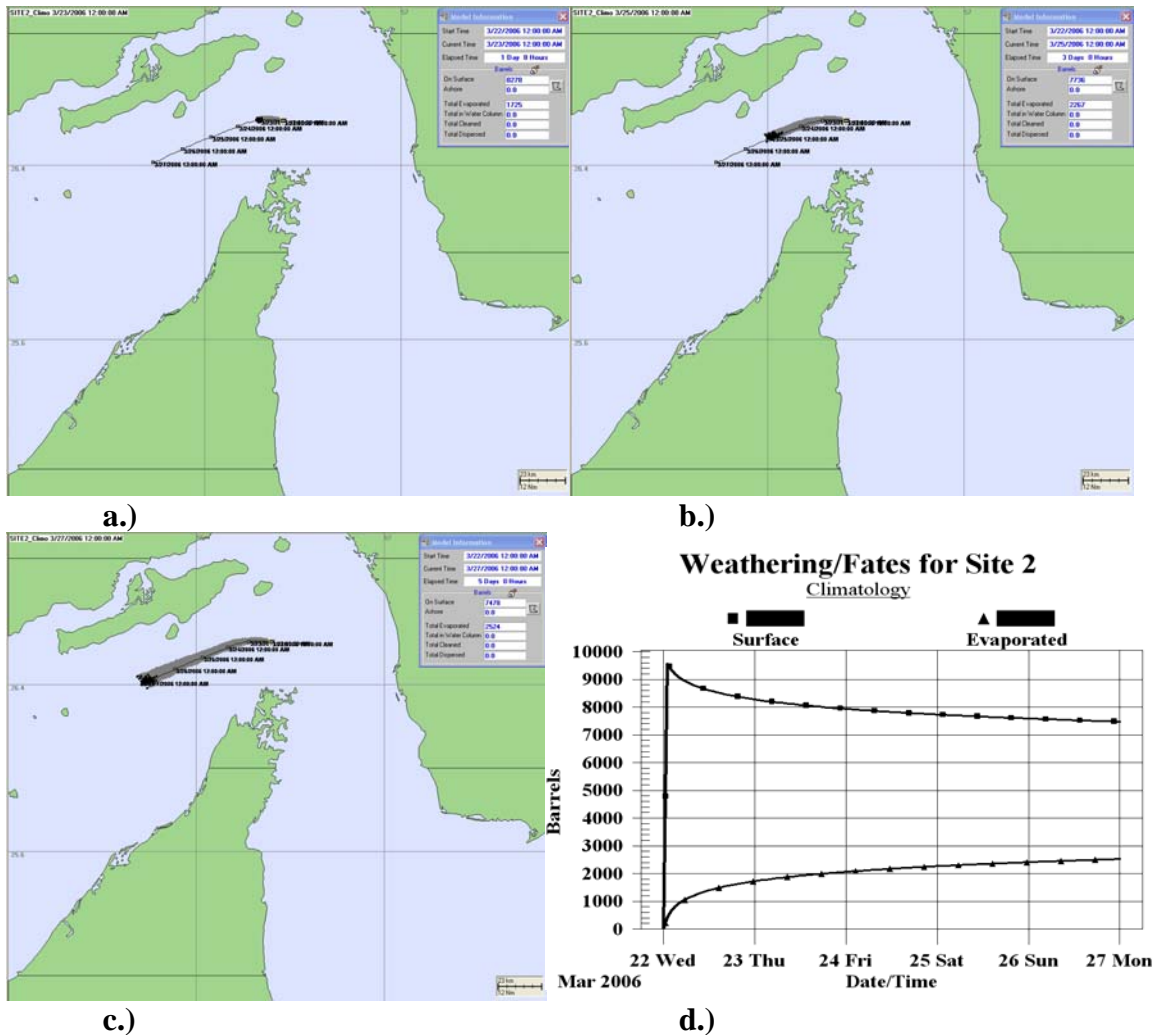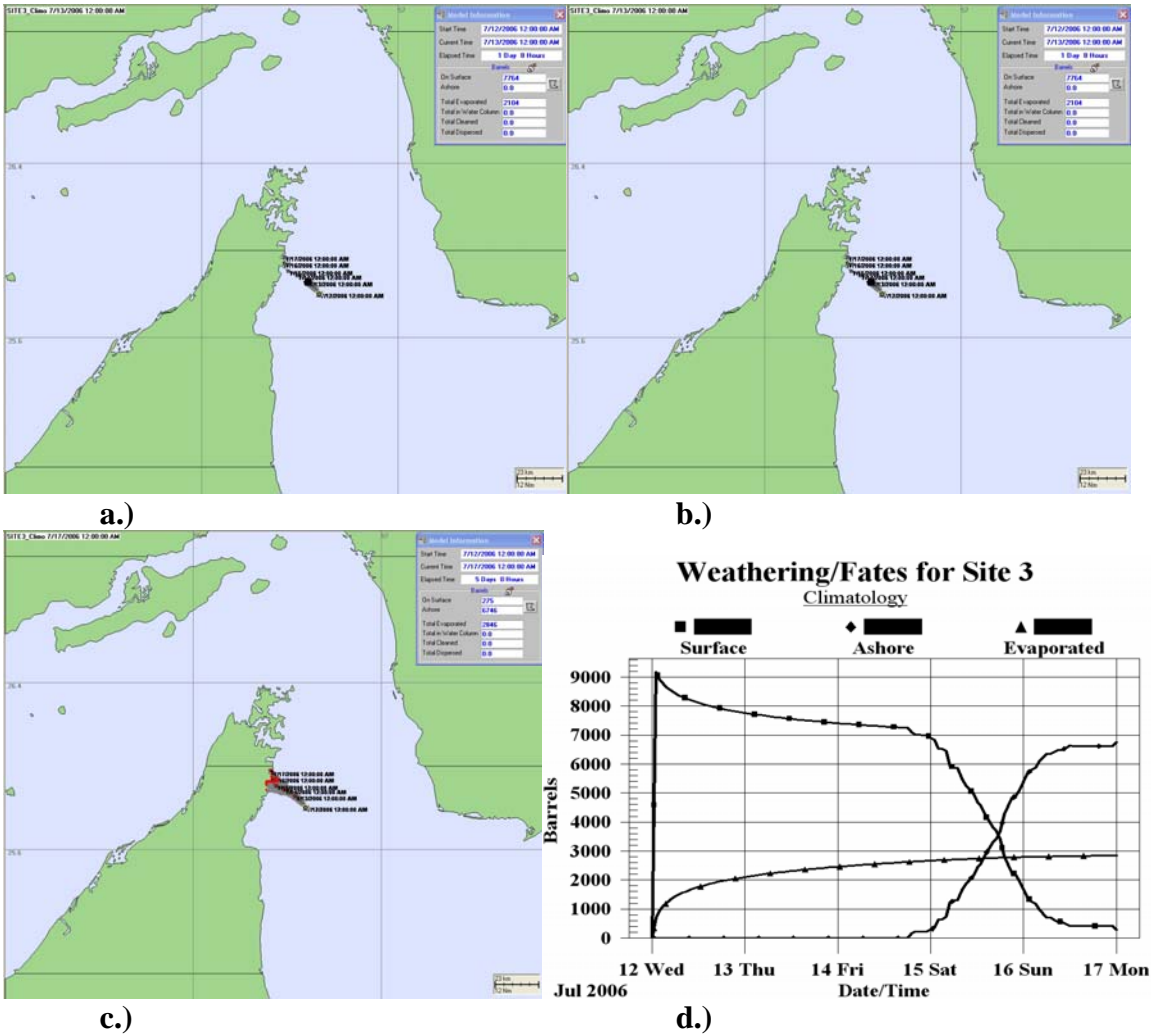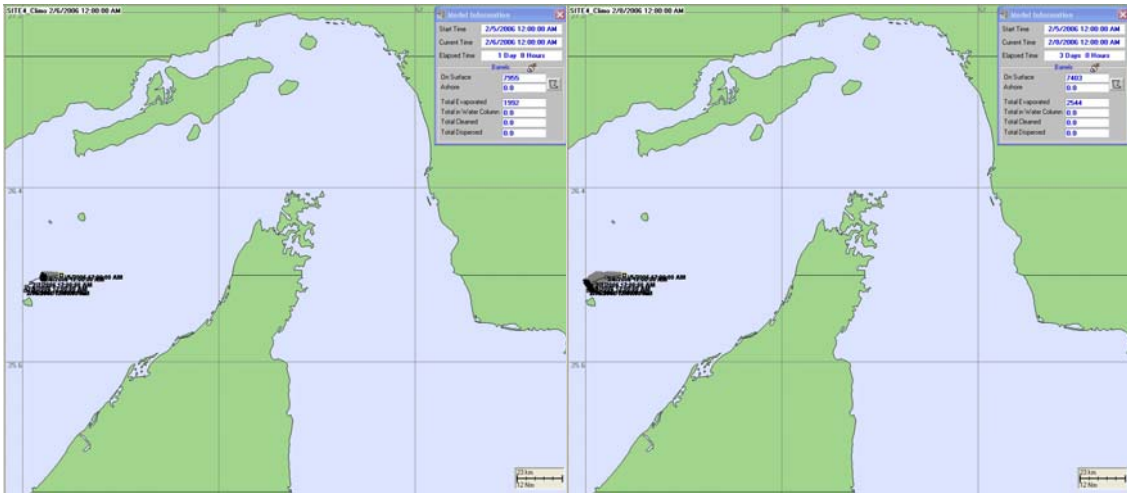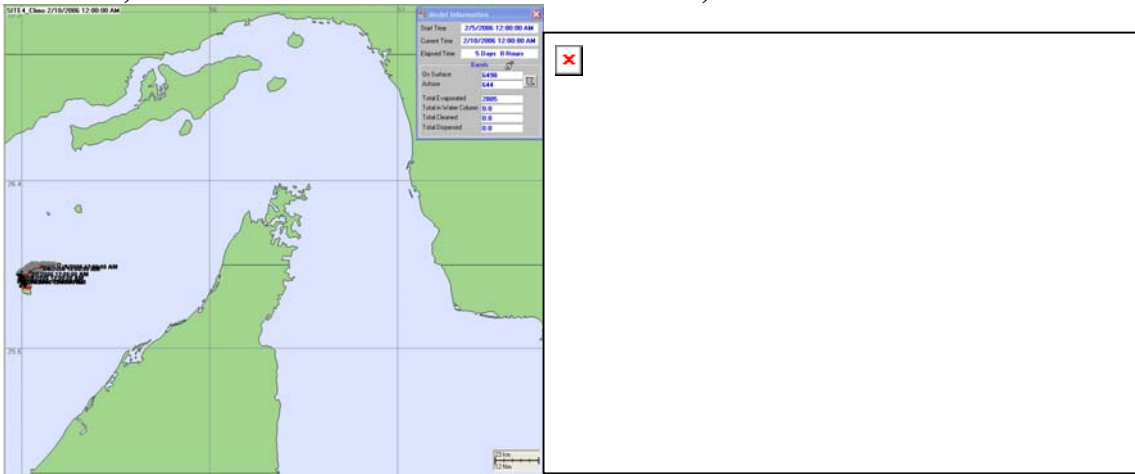
Figure 63.   Site 4 Climatology: a.) at 24 hours, b.) at 72 hours, c.) end state at the
conclusion of five days, and d.) Mass Balance Graph.

VII. MINE DRIFTING

A. HISTORY

Mines have been around since David Bushnell invented his "torpedo" in 1777 for use against the British fleet that then plagued the Americas (Zwolski, 1998). Mines used in World War I were so effective that they were used extensively in World War II and accounted for more ships damaged or lost than any other weapon in the war (Avery, 1998). Contact mines that detonate after making contact with a ship's hull are design relics from World War I. This was the type of mine that was used during the Iran/Iraq war and that so badly damaged the USS Samuel B. Roberts (FFG 58) in 1988 (Zwolski, 1998).

The Roberts puts a picture to the effectiveness of such a low tech weapon (see Figure 64). The mine used cost about $1500 and required no maintenance fuel or pay, and it did about $96 million dollars worth of damage to the USS Samuel B. Roberts (Zwolski, 1998); which already cost millions to build, maintain, and man.

Figure 64.   USS Samuel B. Roberts in drydock undergoing repairs. (After: PH1 Mussi, 1988)

In addition to the cost effectiveness of naval mines, the psychological aspect can not be ignored. During the Korean Conflict, the U.S. Navy was tied up for more than a week when Communist forces mined Wonsan, Korea. The U.S. did the same to Japan

during the Second World War, laying more than 12,000 mines in Japanese shipping lanes. And again U.S. forces stymied Vietnamese forces by shutting down harbors for over 300 days (Greer and Bartholomew, 1986).

B.   SCENARIO SET UP

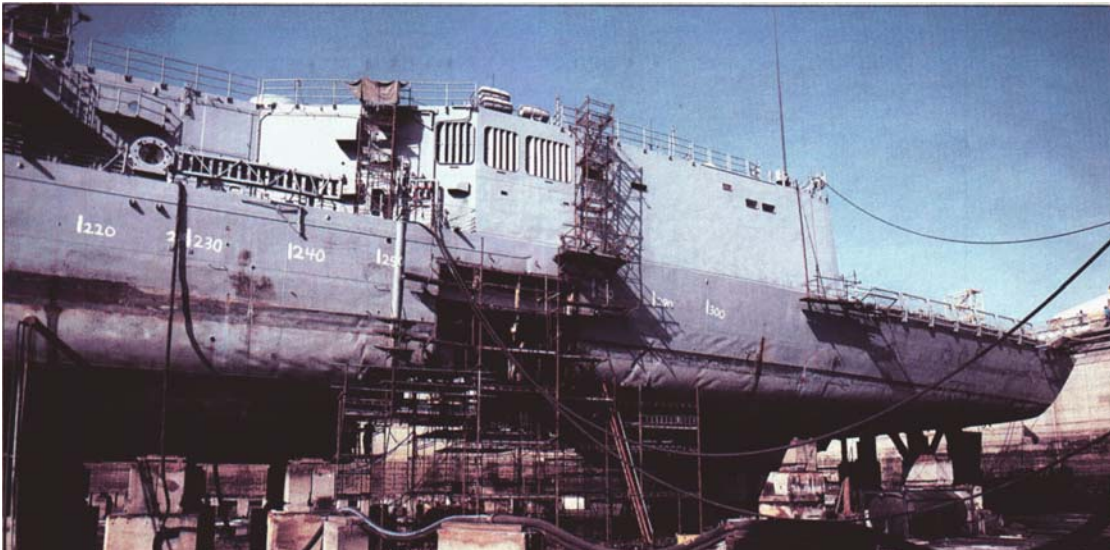Greer and Bartholomew (1986) declared that the most effective use of mines as a deterrent was overt mine laying and that if ship destruction was desired that covert mine laying was best.

The scenario dealt with here is the second form. By causing destruction, terrorists feel they can get their needs addressed and the world attention they desire. This also gives plausible deniability to state actors; who may not want direct conflict with a world class military superpower such as the U.S., yet may want to damage an opponent's resolve.

The mines utilized are of the low-technology, contact-type, deployed from a civilian vessel or unobtrusive vessel that blends with normal SOH traffic. This could be a fishing vessel or high speed craft. Avery (1998) noted that "Practically any surface platform, including fishing boats, patrol craft and merchant vessels" could be easily modified to carry naval mines; hence, the choice of deployment.

The usage of drift mines is with the assumption of range and lack of discrimination for target. Any hit is a good hit in this case as the idea is for chaos to ensue. Couple this with the possible economic and political fallout and the message would be sure to be heard.

The scenarios are run for 48 hours since that is the longest forecast ability for currents immediately available and we are intending to compare to climatology. The "climatology" used was just the six month mean propagated over the six month term. In reality the climatology would not be available for currents. The same premise was used in this scenario set up as in the oil spill.

Four release times were picked from the times utilized for the oil spill scenarios for variety of current profiles for the "real" data runs. Only one run was required for the "climatology" portion since the output would be the same no matter the time started. Comparisons of the "real" to "climatology" were then compared.

The locations of the release points started from the eastern leg of the SOH by the coast of Iran and then reached north of the Musandam peninsula. Then the craft was to swing towards the western portion of the island of Queshm.

Release Point Number	**Latitude (deg N)**	**Longitude (deg E)**
1	26.0	57.1
2	26.2	56.9
3	26.3	56.7
4	26.5	56.6
5	26.6	56.4
6	26.5	56.3
7	26.4	56.0
8	26.3	56.0
9	26.4	55.8
10	26.4	55.5

Table 6.   Mine drop locations.

C.   SCENARIO RESULTS

The currents varied from high to low in the four "real" scenarios and were supposed to be indicative of extreme possibilities. It would be best to describe the climatology first since it is the easiest to understand (Figure 65).

The climatology run could be considered the easiest case and actually was as likely to cause significant damage to ships in the transit lanes as the other scenarios. Since the mines did not move significantly over the 48 hours. If that was the metric there would be a problem. However, the ability for prediction of mine movement is the telling factor. Using this run for the base the other runs could be analyzed while bearing in mind how far from "real" the climatology would become.

The subsequent runs showed much more movement and possible contact points (Figure 66). The range of movement over 48 hours is significant and brought the "real" mines in and out of the transit lanes several times per mine. It is readily apparent that the varying currents of the SOH make the prediction of mine movement all but impossible with a climatology input.
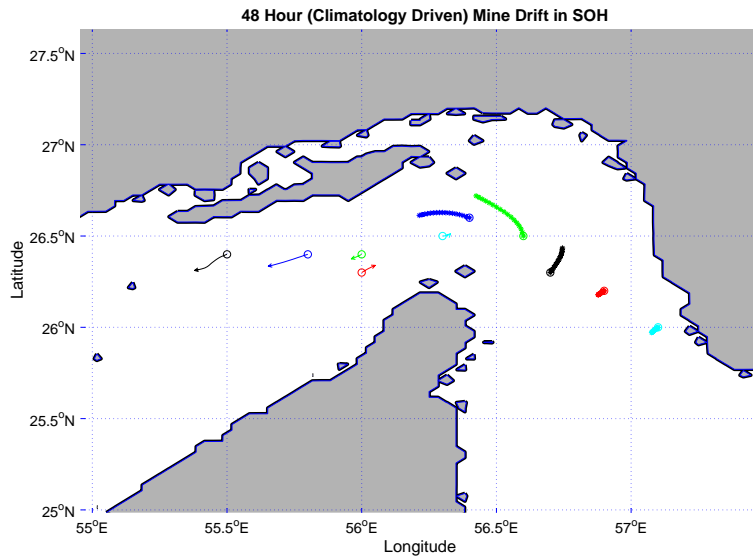
93

Figure 65.   Climatology driven 48 hour mine drift track. Circles show the start points.
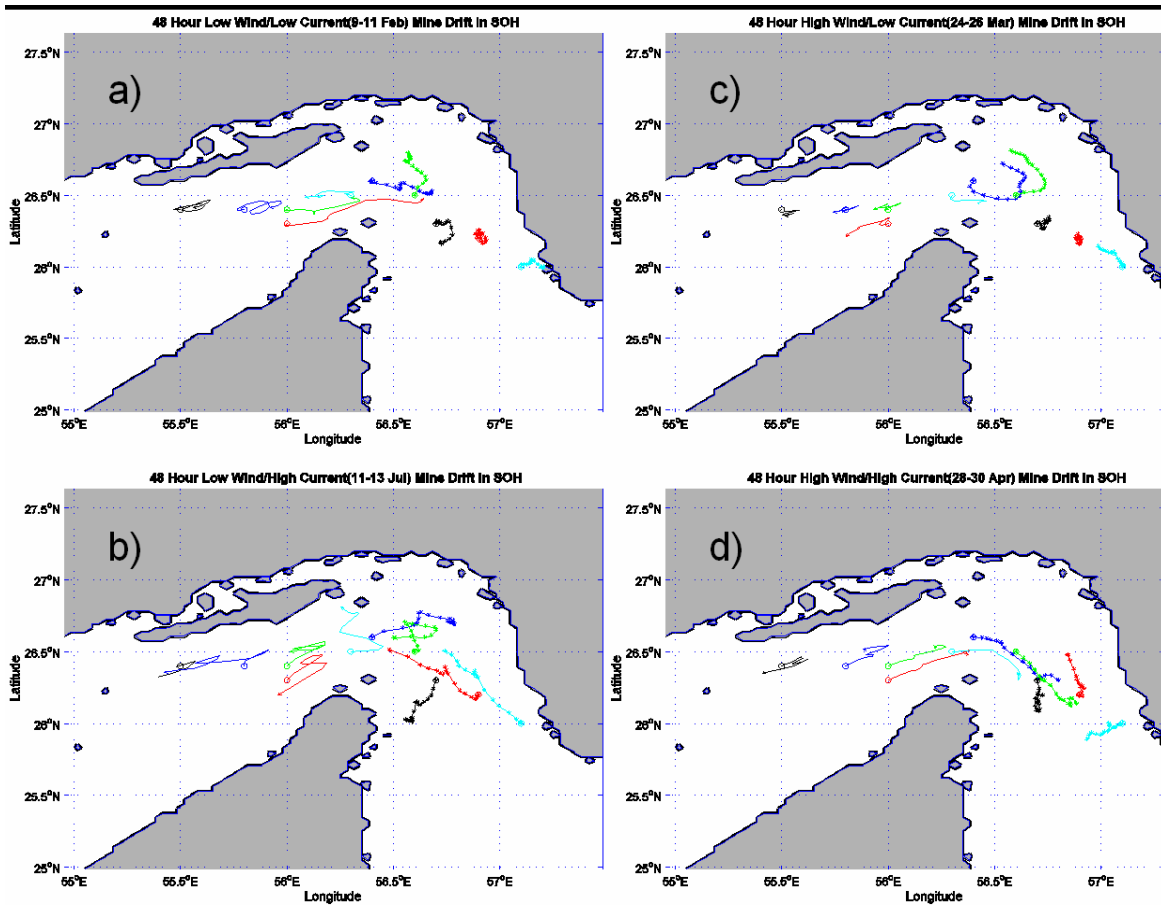

Figure 66.   "Real" data input driven Lagrangian mine drifts for: a) High Wind/Low Current 9-11 Feb, b) Low Wind/High Current 11-13 Jul, c) High Wind/Low Current 24-26 Mar, and d) High Wind/High Current 28-30 Apr.

VIII. CONCLUSIONS

The Strait of Hormuz is a vital flow point for oil and natural gas which supplies the majority of the world with energy. Since it is a natural choke point it is also a natural target for closure. In the volatile environment of the Persian Gulf, where violence is an oft used method of political and ideological furtherance, this avenue of commerce is under constant threat of closure. Any halt to the flow of the resources exiting the Gulf via the SOH is tantamount to a world economic crisis. Once flow is stopped, criticality of the amount of time to transit recommencement can not be easily estimated. In order to safeguard the waters of the Gulf, the U.S. Navy has had a constant presence since 1986. Therefore, to meet future threats to commerce or naval forces in transit through the Strait of Hormuz it is imperative to have the best tools available. For evaluating and planning for possible events in the strait it is best to use model field data vice climatology data.

Through the use of sophisticated numerical modeling and data analysis methods, oceanographic and atmospheric models are among the best in the world. While efforts to make the model forecasts match reality are an ongoing process, the shorter range forecasts are very good tools for operational use. The use of model fields for input to decision aids yields a better answer than climatology alone. While the models may not catch every event that is temporally short, the trends are kept very well. Even if climatology of currents were available, the use of model fields would be preferable due to the constant updates the model makes with every run.

The mine drift scenarios proved that the variability associated with the flow of current in the SOH would be sorely represented by climatology inputs. Even without the analysis of major forcing for the current it would be easy to see, from the results of these comparisons, that the tides are the single most significant feature to accurate portrayal of current in the SOH. This highlights the necessity of utilizing the best models for operational use. By utilizing the best inputs to operational tools such as OILMAP, and others, it enhances the quality of information yielded to the user.

The oil spill runs showed conclusively that the tidal forcing, along with variable winds are necessary for a better prediction of oil slick flow. Without the tidal shift the oil

is unidirectional and lacks the speed change associated with the inflow and outflow regime peaks. Essentially, the utilization of climatology currents is worse than a guess for oil slick prediction. In a reverse estuarine flow such as is found in the Strait of Hormuz, the tidal influence cannot be ignored. Realistic wind forcing is also a necessary feature. Otherwise, the direction of oil slick propagation is primarily due to current, even weak current. In oil spread dynamics, the wind speed is of paramount importance for the prediction of movement and weathering. From analyzing the movement oil under the influence of wind and currents it can be seen that winds greater than 5 m/s can significantly alter the course of oil slicks. However, if the mean wind is an indication of the overall tendency of the strength of winds through the SOH ($\sim$ < 5m/s), then it is the current that is the primary driving force for the course of oil spills in the SOH. Therefore, accurate modeling of currents is important to the overall accuracy of oil spill track prediction.

Areas for future research should include a study of the subsurface variability of current through the SOH and also the effects of stratified layers of suspended oils on surface sonar such as those utilized in mine hunting. Also, the possibility of mine dispersal through an oil slick for possible masking should be properly investigated. Further usage of OILMAP could be made by utilizing the Stochastic Model feature. This would investigate the planning utility of the model in operational use.

LIST OF REFERENCES

Anderson, H., R. Sandza, and R. B. Cullen, 3 August 1987: A Sting in the Gulf: A Mine Blast Interrupts the First U.S. Tanker Convoy to Kuwait. Newsweek, **110**, pp. 24-26.

ASA, 2006: OILMAP User Manual Version 4.8. Applied Science Associates, Inc, 70 Dean Knauss Drive, Narragansett, RI. Web site: www.appsci.com (Downloaded: 1/04/07)

Arakawa, A. and V. R. Lamb, 1977: Computational Design of the Basic Dynamical Processes of the UCLA General Circulation Model. *Methods in Computational Physics*, **17**, Academic Press, pp. 173-265.

Asselin, R. A., 1972: Frequency Filter for Time Integrations. Mon. Wea. Rev., **100**, pp. 487-490.

Associated Press article, 03 Nov 2006: Iran Tes-Fires 3 New Missiles: Tehran Says Missiles Can Cover the Gulf, Strategic Strait of Hormuz. MSNBC, Web site: www.msnbc.msn.com/id/15524966/. (Downloaded on 1/22/07)

Avery, J., 1998: The Naval Mine Threat to U.S. Surface Forces. Surface Warfare, May/June, vol. 23, no. 3, pp. 4-9.Bower, A. S., Hunt, H. D., and Price, J., 2000. Character and Dynamics of the Red Sea and Persian Gulf Outflows. *J. of Geophys. Res. - Oceans*, **105** (C3), pp. 6387-6414.

Baker, N. L., 1992: Quality Control for the Navy Operational Atmospheric Database. *Wea. Forecasting*, **7**, pp 250-261.

Baker, N. L., 1994: Quality Control of Meteorological Observations at Fleet Numerical Meteorology and Oceanography Center. NRL/FR/7531-94-9451. Naval Research Laboratory, Monterey, CA, 93943-5502.

Barker, E., 1992: Design of the Navy's Multivariate Optimum Interpolation Analysis System. *Wea. Forecasting*, **7**, pp 220-231.Chao, S., T. W. Kao, and K. R. Al-Hajri, 1992: A Numerical Investigation of Circulation in the Arabian Gulf. *J. of Geophys. Res.*, **97**, C7, pp. 11,219-11,236.

Berridge, S. A., R. A. Dean, R. G. Fallows, and A. Fish, 1968a: The Properties of Persistent Oils at Sea. *J. Inst. Pet.*, **54**, pp. 300-309.

Berridge, S. A., M. T. Thew, and A. G. Loriston-Clarke, 1968b: The Formation and Stability of Emulsions of Water in Crude Petroleum and Similar Stocks. *J. Inst. Pet.*, **54**, pp. 337-357.

Chu, P.C., H. C. Tseng, C. P. Chang, and J. M. Chen, 1997a: South China Sea Warm Pool Detected in Spring from the Navy's Master Oceanographic Observational Data Set (MOODS). *J. Geophys. Res.*, **102**, 15, pp. 761-15,771.

Chu, P.C., S. H. Lu, and Y. Chen, 1997b: Temporal and Spatial Variabilities of the South China Sea Surface Temperature Anomaly. *J. Geophys. Res.*, **102**, pp. 20937-20955.

CIA, 2007: World Fact Book. U.S. Central Intelligence Agency. Web site: www.cia.gov/cia/publications/factbook/index.html. (Downloaded: 1/28/07).

Clifford, M., C. Horton, and J. Schmitz, 1994: SWAFS: Shallow Water Analysis and Forecast System. *IEEE Oceans '94*, Brest, France, IEEE, pp. 82-87.

Diba, B. A., 10 November 2006: Closing the Strait of Hormuz. *Persian Journal*, Web site: www.iranian.ws/iran_news/publish/printer_18800.shtml. (Downloaded: 1/22/07).

Eager, R. E., S. Raman, P. Childs, R. P. Boyles, J. S. Reid, and D. Westphal, 2005: Observations and Modeling of the Coastal Meteorology of the United Arab Emirates During the Unified Aerosol Experiment (2004). *Sixth Conf. on Coastal Atm. and Oc. Pred. and Proc.*, session 3, Tuesday 11 January 2005.

Ebrahim, A., 2006: Landscape of Iran. Web site: www.manatravels.com/land.htm. (Downloaded: 1/20/07).

Fairall, C.W., E.F. Bradley, D.P. Rogers, J.B. Edson, and G.S. Young, 1996: Bulk Parameterization of Air-Sea Fluxes for Tropical Ocean-Global Atmospheric Coupled-Ocean Atmospheric Response Experiment. *J. Geophys. Res.*, **101**, pp. 3747-3764.

Fox, D. N., W. J. Teague, C. N. Barron, M. R. Carnes, and C. M. Lee, 2002: The Modular Ocean Data Assimilation System (MODAS). *J. of Atm. and Ocean. Tech.*, **19**, pp. 240-252.

Gandin, L.S., 1988: Complex Quality Control of Meteorological Observations. *Mon. Wea. Rev.*, **116**, pp. 1137-1156.

Goerss, J. and P. Phoebus, 1992: The Navy's Operational Atmospheric Analysis. *Wea. Forecasting*, **7**, pp 232-249.

Greer, W. L. and J. Bartholomew, February 1986: The Psychology of Mine Warfare. *US Naval Institute Proceedings*, vol. **112**, no. 2, pp. 58-62.

IPS MeteoStar, 1995-2004: Climatology for Winds in Oman, Iran, and UAE. Web site: http://wxweb.meteostar.com/climate/ (Downloaded: 1/28/07)

Haeger, S.D., 2006: Data Assimilation for Operational Models, PowerPoint Presentation utilized during teleconference at Naval Postgraduate School Monterey, CA, 2 February, 2007.

Haltiner, G. J. and R. T. Williams, 1980: Numerical Weather Prediction and Dynamic Meteorology. John Wiley and Sons.

Hotelling, H., 1933: Analysis of a Complex of Statistical Variables into Principal Components. *J. Edu. Psych.*, **24**, pp. 417-441, 498-520.

HUMS, 2001: Hormozgan Province. Hormozgan University of Medical Sciences. Web site: www.hums.ac.ir/english/province/hormozgan%20english/index.html .

Kaihatu, J. M., R. A. Handler, G. O. Marmorino, and L. K. Shay, 1998: Empirical Orthogonal Function Analysis of Ocean Surface Currents Using Complex and Real-Vector Methods. *J. of Atm. and Ocean. Tech.*, vol. **15**, pp. 927-941.

Kämpf, J. and M. Sadrinasab, 2006: The Circulation of the Persian Gulf: a Numerical Study. *Ocean Science*, **2**, pp. 27-41.

Kantha, L. H. and C. A. Clayson, 2000: Numerical Models of Oceans and Oceanic Processes. Academic Press-International Geophysics Series, vol. **66**.

Kjeilen, T., 1996: Encyclopaedia of the Orient. Web site: www.i-cias.com/e.o/hormuz.htm (Downloaded on 1/20/07).

Klemp, J. and R. Wilhelmson, 1978: The Simulation of Three-Dimensional Convective Storm Dynamics. *J. Atmos. Sci.*, **35**, pp. 1070-1096.

Kreil, E., 2004: Persian Gulf Oil and Gas Exports Fact Sheet. Energy Information Agency, Department of Energy, Country Analysis Briefs, September. Web site: www.eia.doe.gov/emeu/cabs/pgulf.html, (Downloaded on 1/5/07).

Looney, R. E., 2002: Globalization and Maritime Power Chapter 6: Market Effects of Naval Presence in a Globalized World: A Research Summary. Web site: www.ndu.edu/inss/books/Books_2002/Globalization_and_Maritime_Power_Dec_02/07_ch06.htm. (Downloaded on 1/21/07)

Louis, J.-F., 1979: A Parametric Model of Vertical Eddy Fluxes in the Atmosphere. *Bound. Layer. Meteor.*, **17**, pp. 187-202.

McCarthy, J. D., 1991: U.S.S. VINCENNES (CG 49) Shootdown of Iran Air Flight 655: A Comprehensive Analysis of Legal Issues Presented by the Case Concerning the Aerial Incident of 3 July 1988 (Islamic Republic of Iran v. United States of America). Master's Thesis, Naval Postgraduate School, Monterey, CA.

Mellor, G. L., 2004: Users Guide for a Three Dimensional, Primitive Equation, Numerical Ocean Model. Princeton University, Princeton, NJ. Web site: http://www.aos.princeton.edu/WWWPUBLIC/htdocs.pom/

Mellor, G. L. and T. Yamada, 1974: Development of a Turbulence Closure for Geophysical Fluid Problems. *Rev. Geophys. And Space Phys.*, **20**, pp. 851-875.

Metz, H. C., 1993: Persian Gulf States: A Country Study. Washington: GPO for the Library of Congress.

Mussi, C., 1988: To See the Dawn: The Night-Long Battle to Save USS Roberts. All Hands, August, no. 857, pp. 4-10.

Nincic, D. J., 2002: Globalization and Maritime Power Chapter 8: Sea Lane Security and U.S. Maritime Trade: Chokepoints as Scarce Resources. Web site: www.ndu.edu/inss/books/Books_2002/Globalization_and_Maritime_Power_Dec_02/09_ch08.htm. (Downloaded on 1/21/07)

Pauley, P., 2003: Superobbing Satellite Winds for NAVDAS. NRL Publication NRF/MR/7530--03-8670.

Reynolds, R.M., 1993: Physical Oceanography of the Gulf, Strait of Hormuz, and the Gulf of Oman-Results from the Mt Mitchell Expedition. *Marine Pollution Bulletin*, **27**, pp. 35-59.

Richman, M.B., 1986: Rotation of Principal Components. *J. Climatology*, **6**, pp. 293-235.

Robert, A. J., 1966: The Investigation of a Low-Order Spectral Form of the Primitive Equation Models. *J. Meteor. Soc. Japan.*, **44**, pp. 237-245.

Sheppard, C. R. C. and D. J. Dixon, 1998: Chapter 32. Seas of the Arabian Region: Coastal Segment (29, S). *The Sea*, vol. **11**, pp. 915-931.

Sirovich, L., 1987: Turbulence and the Dynamics of Coherent Structures, Part I: Coherent Structures. *Quart. Appl. Math.*, vol. **45**, pp. 561-571.

Skamarock, W. C. and J. B. Klemp, 1992: The Stability of Time-Split Numerical Methods for the Hydrostatic and the Nonhydrostatic Elastic Equations. *Mon. Wea. Rev.*, **120**, pp. 2109-2127.

Swift, S. A. and A. S. Bower, 2002: Formation and Circulation of Dense Water in the Persian/Arabian Gulf. *Journal of Geophysical Research - Oceans*, **108**(C1), 10.1029/2002JC001360.

Titley, D., 2007: Achieving Battlespace On Demand. PowerPoint Presentation utilized during lecture on Battlespace on Demand at Naval Postgraduate School Monterey, CA, 26 January 2007.

Traut, L., 2002: Musandam Peninsula. Desert Discovery, Web site: www.desert-discovery.com/text/regions/map.html. (Downloaded on 1/15/07).

Weare, B.C., A.R. Navato, and R.E. Newell, 1976: Empirical Orthogonal Analysis of Pacific Sea Surface Temperature. *J. Phys. Oceanogr.*, **6**, pp. 671-678.

Whitham, B. T., D. F. Duckworth, A. A. B. Harvey, P. G. Jeffrey, and S. G. Perry, 1974: Marine Pollution by Oil: Characterization of Pollutants, Sampling, Analysis, and Interpretation. Institute of Petroleum Oil Pollution Analysis Committee, London, Great Britain. Applied Science Publishers LTD.

Wilson, E. B., J. M. Hunt, J. N. Butler, C. D. McAuliffe, R. Patrick, E. A. Pearson, W. D. Garrett, J. M. Teal, F. T. Weiss, R. C. Vetter, and M. H. M. Katsouros, 1975: Petroleum in the Marine Environment: Workshop on Inputs, Fates, and the Effects of Petroleum in the Marine Environment May 21-25, 1973. National Academy of Sciences, Washington D.C.

Winkler, D. F., 2003: Operation Praying Mantis Blows a Hole in Iranian Navy. Navy League of the United States. Web site: www.navyleague.org/sea_power/sep_03_45.php. (Downloaded: 2/28/07)

Zaman, 03 Nov 2006: Iran Tests 3 Missiles in Persian Gulf. Zaman Online: First Turkish Paper on the Internet, Web site: www.zaman.com/?bl=hotnews&alt=&hn=37928. (Downloaded on 1/11/07)

Zhu, M. and B.W. Atkinson, 2004: Observed and Modeled Climatology of the Land Sea Breeze Circulation Over the Persian Gulf. *Int. J. Climatology*, vol. **24**, no. 7, pp. 883-905

Zwolski, M., 1998: The History of Mining. *Surface Warfare*, May/June, vol. 23, no. 3, pp. 20-21.

THIS PAGE INTENTIONALLY LEFT BLANK

INITIAL DISTRIBUTION LIST

1. Defense Technical Information
   Center Ft. Belvoir, Virginia

2. Dudley Knox Library
   Naval Postgraduate School
   Monterey, California

3. Mr. Edward Gough
   CNMOC Technical Director
   Stennis Space Center, Mississippi

4. CAPT David W Titley
   CNMOC, COO
   Stennis Space Center, Mississippi

5. CAPT Jim Berdeguez
   CNMOC DOO for ASW/MIW

6. CAPT Robert E. Kiser
   CNMOC DOO Stennis
   Space Center, Mississippi

7. Professor Mary L. Batteen
   Naval Postgraduate School
   Monterey, California

8. Professor Peter C Chu
   Naval Postgraduate School
   Monterey, California

9. LT Travis Clem
   Naval Postgraduate School
   Monterey, California

10. Mr. Ronald Betsch
    MIW Program Manager
    Naval Oceanographic Office
    Stennis Space Center, Mississippi

11. Mr. Steve Haeger
    Naval Oceanographic Office
    Stennis Space Center, Mississippi

12.   Mr. Matthew Ward
       Applied Science Associates, Inc.
       Narragansett, Rhode Island

13.   Professor Curtis Collins
       Naval Postgraduate School
       Monterey, California